TEMPORAL-MODE INTERFEROMETRY: A TECHNIQUE FOR HIGHLY SELECTIVE QUANTUM PULSE GATING VIA CASCADED FREQUENCY CONVERSION IN NONLINEAR OPTICAL WAVEGUIDES

by

DILEEP VENKATARAMA REDDY

A DISSERTATION

Presented to the Department of Physics
and the Graduate School of the University of Oregon
in partial fulfillment of the requirements
for the degree of
Doctor of Philosophy

September 2017

DISSERTATION APPROVAL PAGE

Student: Dileep Venkatarama Reddy

Title: Temporal-Mode Interferometry: A Technique for Highly Selective Quantum Pulse Gating via Cascaded Frequency Conversion in Nonlinear Optical Waveguides

This dissertation has been accepted and approved in partial fulfillment of the requirements for the Doctor of Philosophy degree in the Department of Physics by:

Daniel A. Steck	Chair
Michael G. Raymer	Advisor
John Toner	Core Member
Andrew H. Marcus	Institutional Representative

and

Sara D. Hodges	Interim Vice Provost and Dean of the Graduate School

Original approval signatures are on file with the University of Oregon Graduate School.

Degree awarded September 2017

DISSERTATION ABSTRACT

Dileep Venkatarama Reddy

Doctor of Philosophy

Department of Physics

September 2017

Title: Temporal-Mode Interferometry: A Technique for Highly Selective Quantum Pulse Gating via Cascaded Frequency Conversion in Nonlinear Optical Waveguides

A new, and thus far only, method to overcome a selectivity barrier in parametrically pumped quantum pulse gates is proposed and experimentally demonstrated for the first time, using frequency conversion of optical temporal modes in second-order nonlinear waveguides. Temporal modes and quantum pulse gates are defined and their utilities are explored. Pulsed operation of three-field and four-field, parametric, optical processes are modeled and numerically investigated. A maximum limit to achievable selectivity for quantum pulse gating in uniform media is discovered and theoretically explained. An interferometric means of overcoming said limit and asymptotically approaching unit selectivity is proposed. The principle is experimentally verified by double-passing specifically shaped optical pulses derived from an ultrafast Ti:sapphire laser through a periodically-poled lithium niobate waveguide phasematched for sum-frequency generation. Further improvements and future implications for quantum technologies are discussed.

This dissertation includes previously published co-authored material.

CURRICULUM VITAE

NAME OF AUTHOR: Dileep Venkatarama Reddy

GRADUATE AND UNDERGRADUATE SCHOOLS ATTENDED:

University of Oregon
Indian Institute of Technology - Madras

DEGREES AWARDED:

Doctor of Philosophy, Physics, 2017, University of Oregon
Master of Technology, Communications and Signal Processing, 2009, Indian Institute of Technology - Madras
Bachelor of Technology, Electrical Engineering, 2009, Indian Institute of Technology - Madras

AREAS OF SPECIAL INTEREST:

Nonlinear Quantum Optics
Quantum Field Theory
Numerical Simulations
Electronics

PROFESSIONAL EXPERIENCE:

Graduate Research Assistant, Department of Physics, University of Oregon

Graduate Teaching Assistant, Department of Physics, University of Oregon

GRANTS, AWARDS AND HONORS:

Science Literacy Program (SLP) fellowship, University of Oregon, 2014

Science Literacy Program (SLP) fellowship, University of Oregon, 2013

Weiser Senior Teaching Assistant Award, Department of Physics, University of Oregon, 2012-13

Weiser General Physics Graduate Teaching Assistant Award, Department of Physics, University of Oregon, 2010-11

Summer Research Fellowship Program (SRFP), Jawaharlal Nehru Institute of Advanced Scientific Research (JNCASR), 2006

PUBLICATIONS:

Dileep V. Reddy and M. G. Raymer, "Photonic temporal-mode multiplexing by quantum frequency conversion in a dichroic-finesse cavity," preprint arXiv:1708.01705 (2017).

J. Nunn, J. H. D. Munns, S. Thomas, K. T. Kaczmarek, C. Qiu, A. Feizpour, E. Poem, B. Brecht, D. J. Saunders, P. M. Ledingham, Dileep V. Reddy, M. G. Raymer, and I. A. Walmsley, "Theory of noise suppression in Λ-type quantum memories by means of a cavity," *Phys. Rev. A* **96**, 012338 (2017).

Dileep V. Reddy and M. G. Raymer, "Engineering temporal-mode-selective frequency conversion in nonlinear optical waveguides: From theory to experiment," *Opt. Express* **25**, 12952–12966 (2017).

D. L. P. Vitullo, C. C. Leary, P. Gregg, R. A. Smith, Dileep V. Reddy, S. Ramachandran, and M. G. Raymer, "Observation of interaction of spin and intrinsic orbital angular momentum of light," *Phys. Rev. Lett.* **118**, 083601 (2017).

R. A. Smith, Dileep V. Reddy, D. L. P. Vitullo, and M. G. Raymer, "Double-heralded generation of two-photon-states by spontaneous four-wave-mixing in the presence of noise," *Opt. Express* **24**, 5809–5821 (2016).

D. L. P. Vitullo, C. C. Leary, P. Gregg, R. A. Smith, Dileep V. Reddy, S. Ramachandran, and M. G. Raymer, "Observation of intrinsic spin-orbit interaction of light in few-mode optical fiber," *Frontiers of Optics (FiO'16)*, OSA Technical Digest, paper FW2B.4 (2016).

M. G. Raymer and Dileep V. Reddy, "Theory of loss in a distributed feedback cavity-enhanced single-photon SPDC source," *Frontiers in Optics (FiO'16)*, OSA Technical Digest, paper LF2E.4 (2016).

B. Brecht, Dileep V. Reddy, C. Silberhorn, and M. G. Raymer, "Photon temporal modes: A complete framework for quantum information science," *Phys. Rev. X* **5**, 041017 (2015).

J. B. Christensen, Dileep V. Reddy, C. J. McKinstrie, K. Rottwitt, and M. G. Raymer, "Temporal mode sorting using dual-stage quantum frequency conversion by asymmetric Bragg scattering," *Opt. Express* **23**, 23287–23301 (2015).

D. V. Reddy, M. G. Raymer, and C. J. McKinstrie, "Sorting photon wave packets using temporal-mode interferometry based on multiple-stage quantum frequency conversion," *Phys. Rev. A* **91**, 012323 (2015).

R. A. Smith, Dileep V. Reddy, D. L. P. Vitullo, and M. G. Raymer, "Verification of a heralded, two-photon Fock state with a gang of detectors," *Frontiers in Optics (FiO'15)*, OSA Technical Digest, paper FTu3G.2 (2015).

Michael G. Raymer, Benjamin Brecht, Dileep V. Reddy, and Christine Silberhorn, "Photon temporal modes as a complete framework for quantum information," *Frontiers in Optics (FiO'15)*, OSA Technical Digest, paper FW3D.2 (2015).

B. Brecht, Dileep V. Reddy, C. Silberhorn, and M. G. Raymer, "Quantum information science with temporal modes," *Publication on Lasers and Electro-Optics (CLEO'15)*, OSA Technical Digest, paper EB_2a_2 (2015).

D. V. Reddy, M. G. Raymer, and C. J. McKinstrie, "Efficient sorting of quantum-optical wave packets by temporal-mode interferometry," *Opt. Lett.* **39**, 2924–2927 (2014).

D. V. Reddy, M. G. Raymer, and C. J. McKinstrie, "Efficient sorting of single-photon wave packets by temporal-mode interferometry," *Frontiers in Optics (FiO'14)*, OSA Technical Digest, paper FTu4A.5 (2014).

D. V. Reddy, M. G. Raymer, C. J. McKinstrie, L. Mejling, and K. Rottwitt, "Temporal mode selectivity by frequency conversion in second-order nonlinear optical waveguides," *Opt. Express* **21**, 13840–13863 (2013).

L. Mejling, Dileep V. Reddy, C. J. McKinstrie, M. G. Raymer, and K. Rottwitt, "Mode selectivity with quantum-state-preserving frequency conversion using four-wave mixing," *Photonic Society Summer Topical Meeting Series*, IEEE (2013).

L. M. Andersen, Dileep V. Reddy, C. J. McKinstrie, M. G. Raymer, and K. Rottwitt, "Quantum-state-preserving Frequency Conversion Using Four-wave Mixing," *Nonlinear Optics (NLO'13)*, OSA Technical Digest, paper NTu1A.2 (2013).

ACKNOWLEDGEMENTS

I would start by thanking professor Michael G. Raymer, whose guidance and trust enabled me to bloom in this field. He introduced me to the central problem of this dissertation on my first day in his lab. For that and everything else, I am eternally grateful.

Many collaborators from across the world have been instrumental in my getting this far. I owe Dr. Colin J. McKinstrie and Dr. Lasse Mejling for easing my entry into the theory. Prof. Christine Silberhorn and Dr. Bejamin Brecht have been very helpful and accomodating in our pursuit of common goals, as have Dr. Jesper Christensen and Prof. Karsten Rottwitt. Prof. Kartik Srinivasan, Prof. Joshua Nunn, and Prof. Brian J. Smith were all ready and willing to lend the full benefit of their experience to my project.

Next come the machine shop staff. John Boosinger, Jeffrey Garman, and Kris Johnson gave me free reign to use the machine shop for my personal projects. Cliff Dax is a total wizard with electronics, and Larry Scatena can solve all your laser problems with a wave of his hands. You guys actually keep this place running, and I thank you all.

I thank the entire physics faculty for maintaining such a fun, diverse, and jovial atmosphere at the department. Prof. Eric Corwin took me under his wing when I was still green behind the ears. Prof. John Toner, Prof. Steven van Enk and Prof. Daniel Steck were experts always readily available for consultation. Prof. Gregory Bothun has been a witty life coach, and Prof. Stephen Gregory and Prof. Dean Livelybrooks have been excellent graduate councillors. I thank Prof. Jim Brau, Prof. David Soper, and Prof. Eric Torrence for patiently hearing

out my esoteric ideas. And I thank Prof. Scott Fisher and Stanley Micklavzina for being gung-ho about physics outreach.

The OMQ administrative director Dr. Brandy Todd and her rotating minions were invaluable in keeping the center afloat and all the grads functional. I will always remember current and former physics administrative staff members Bonnie Grimm, Doreen Kester, Jodi Myers, Jani Scallion, Tiffany Stewart, Christine Waite, Laurie Schneider, Patty Smith and Patricia Valenzuela. You all are the bolts that keep the machine intact.

My office mate Dr. Kyle Klarup is the nicest guy I know, and he made the space homely and livable. Dr. Roger Smith taught me my first lessons about running an optics experiment, and Dr. Dashiell Vitullo supplemented it generously. Dr. Erin Mondloch induced in me a pavlovian conditioning where I still say goodbye in person to everyone in the labs and offices before leaving for the day. Dr. Jonathan Lavoie came in late, but brought in his French-Canadian quirks as compensation.

Wesley Erickson and Erik Keever were ever willing or pursue ellaborate hobbies. Weekly quantum discussion lunches with Dr. Chris Jackson, and Andrea Goering's nudging towards Spice-camp and Country Fair have been formative. Thank you Eryn Cook for introducing me to road biking, and being my belaying partner at the climbing gym. And thank you Dr. Laura McWilliams for the ounces of caffeinated humanity, and for playing Dante to my Virgil.

I thank all of my mentors at IITM, BASE, and KVIISc for giving me the best education in the world. And to close, I thank my parents Prof. B. V. V. Reddy and Annapurna V. Reddy. You have sacrificed much, and I have been the wayward son. I will place this work and more at your feet.

To Jayanth. You'd better catch up fast. I have plans for us.

TABLE OF CONTENTS

LIST OF FIGURES

LIST OF TABLES

CHAPTER I

PROBLEM STATEMENT AND MOTIVATION

"The Night, once the font of the Unknown, becomes only the lack of Sun."

– The Trickster's lament, quote from "Thief: The Dark Project"

Light in History and Modernity

The identification of light as a tangible entity sprang from an observed contrast in conditions between its presence versus its absence. Ancient mythologies associated light with positive virtue and divinity due to its ability to illuminate darkness and shadows, thereby literally reducing ignorance, and revealing hidden truths. Many attempts at a materialistic explanation for the phenomenon were made over the centuries. The advent of metallurgy, glass blowing, and the patronage of craftsmanship by early and medieval civilizations enabled the creation of the field of ray optics, which could phenomenologically predict the behavior of light when refracted through transparent materials, or reflected off of mirrored surfaces of known geometries. But monumentally reductionist successes in our understanding of light occurred after the codification of the modern scientific method, and parallel developments in, at the time, unrelated fields.

An atomistic, particle or corpuscle theory of light has its roots in antiquity, but was coherently articulated in the classical physics tradition by Newton [1] in the 17th century. Newton formulated his hypotheses based on refraction of light into its constituent colors in dense media, and in an attempt to relate this to gravity. His contemporaries and successors, such as Hooke [2], Huygens [3], Euler [4], and Young [5], promoted the wave theory of light through their experiments on

interference and diffraction. By mid-19th century, the mathematical framework for explaining both interference and polarization of light as manifestations of transverse waves had been fully developed. Experiments by Michelson and Morley [6] measured the speed of light in the Earth's atmosphere. By establishing the invariance of its value to the velocity of the frame of reference, they burried the then prominent, mechanical vibrations in "luminiferous ether" model.

In mid-19th century, Faraday [7] had discovered the rotation of polarization of light in the presence of a longitudinal magnetic field, and speculated that light waves might indeed be travelling disturbances in the ubiquitous vacuum electromagnetic field. This inspired Maxwell [8] to render the classical equations governing electromagnetic fields, and derive the self-propagating wave equations for electromagnetic radiation at the exact, measured speed. Hertz [9] and others confirmed the correspondence predicted between radio waves and visible light. By the end of the 19th century, the classical conception of light was complete and self consistent, but could not explain resonant lines in atomic emission/absorption spectra. Thermodynamic applications of the classical theory also made unrealistic predictions for blackbody radiation, i.e. the spectra of thermal radiation from objects at nonzero (absolute) temperature.

In 1901, Planck [10] showed that quantizing the exchange of energy between matter and the electromagnetic field to discrete amounts whose value depended only on the frequency, would entropically predict the blackbody spectrum. Einstein [11] utilized the idea of light quanta to explain photoelectric effect, and this, along with Compton scattering [12] of X-rays, lent credence to the existence of photons as "particle-like" excitations in the electromagnetic field. These behaviors were easily subsumed into quantum physics by Dirac and others. His early attempt

[13] at relativistic field theory laid the foundation for the development of quantum electrodynamics by Tomonaga [14], Schwinger [15], and Feynman [16], which treated all electromagnetic interactions between charged particles and photons as couplings between fermionic and bosonic quantum fields respectively. These theories later evolved to encompass other types of physical interactions, and lead to the photonic field taking its place as one of four prime force carriers between fundamental particles in the Standard Model pantheon.

The latter half of the 20th century saw the invention of the Laser, and new developments in the study of spectroscopy, Raman transitions, and light-matter interactions in nonlinear materials prompted a need for a formal theory of coherent optical macroscopic and microscopic processes. Glauber [17] and Sudarshan [18], along with their collaborators, invented a means of representing arbitrary quantum states of light as a phase-space distribution of coherent states, paving the way for the entire field of Quantum Optics. Aspect [19] used entangled photon pairs to violate CHSH inequalities [20], which were mathematical expressions unbreakable under classical assumptions about the nature of the physical universe. Today, cutting-edge theoretical and experimental works on the philosophically loaded questions about interpretations of quantum mechanics are performed in this field at these energy scales.

Figure 1 showcases a schematic of the entire electromagnetic spectrum ordered with respect to wavelength (proportional to inverse of frequency of oscillation of the waves). I have tagged the major regions for their relevance to certain natural phenomena. I have also illustrated various human technologies that operate in and/or rely on specific bands.Both the modern world, and our

understanding of the universe, has benefited enormously from our investigations into light.

Orthogonality and Selective Devices

Electromagnetic radiation is the dominant medium for long-distance and network communication today. In the ad-hoc, unstructured wireless paradigm of HAM radio, multiple independent transmissions occur into the same spatio-temporal airspace. The reservation of specific frequency bands for specific purposes, the spurious and sparse distribution of transmissions, and the legal limitations on transmitting powers (thus limiting effective range) all serve to avoid contentions for resource [21]. Wireless comsumer technology protocols like wifi and bluetooth open and maintain persistent sessions with connecting users, and assign temporary frequency bands/channels to each one, allowing for concurrent multi-user, multi-network functionality. Officially registered AM and FM radio stations purchase licenses from local governmental agencies to operate in non-overlapping frequency bands to avoid collision. Multiple stations can operate in the same bands as long as their transmissions originate from distances greater than the sum of their effective ranges. This general way of maintaining multiple simultaneous communication channels in the same spatio-temporal physical volume by relying on disjoint frequency bands is called "wavelength-division multiplexing" (WDM).

GSM cellphone towers, in addition to WDM, employ another approach to increase their capacity. They transmit a general clock reference signal to synchronize all the cellphones connected to them, and then split their transmissions into distinct time bins, where each bin is assigned to a specific user [22]. This method is known as "time-division multiplexing" (TDM). Long-haul

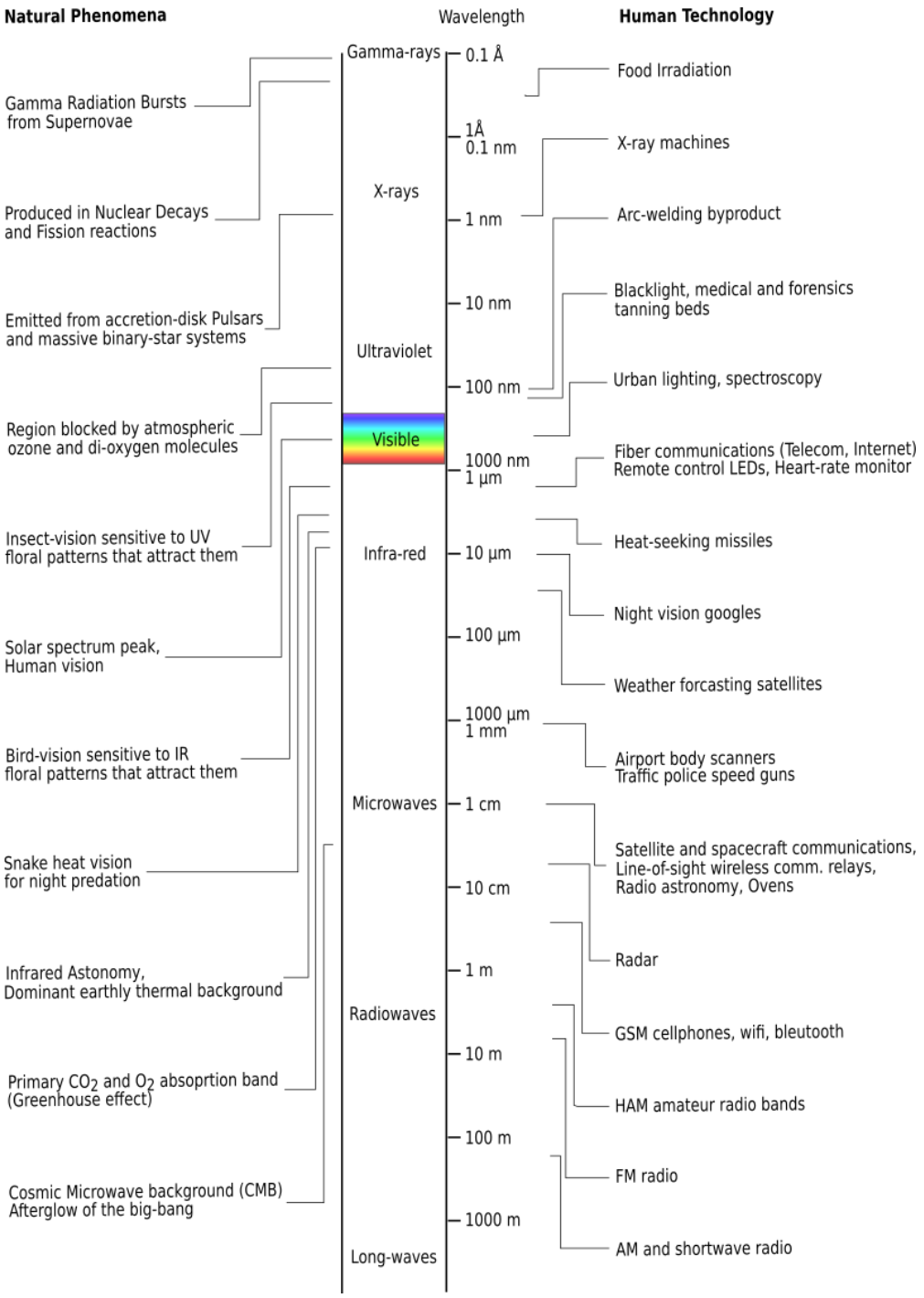

FIGURE 1. The electromagnetic spectrum, with some ranges tagged with technology or natural phenomena relevant to those length/energy scales.

optical fibers, which form the backbone of the world-wide internet, are typically constrained to transmit in a fairly narrow range of frequencies/wavelengths without experiencing significant loss or dispersion. Most telecommunication fiber transmissions modulate the quadrature (amplitude and phase) of a coherent beam at a set wavelength to transmit information. But even within the narrow fiber-transmission bands, both WDM and TDM have been employed to boost the fiber carrying capacity [23].

The recent decade has seen much effort put into guiding multiple transverse-spatial modes of light in the same, large-core fibers [24]. These transverse modes, or "orbital angular-momentum" (OAM) modes should transmit independently, barring fiber imperfections. OAM beams have recently been successfully deployed for multichannel line-of-sight freespace communication as well [25]. And well-designed geometric configurations of arrays of antenna can not only select for signal direction, but also its transverse mode profile.

In addition to time-frequency bands/bins, and transverse mode distributions, electromagnetic (EM) field has one more property: polarization. Being a vector field, its modes have a field-direction profile along with an amplitude profile. Physical constraints restrict the polarization to be transverse to the direction of propagation (in isotropic media). This two-dimensional basis can also be used as two channels, like in stereoscopic vision applications like 3D movies. They are also used in liquid-crystal display (LCD) screens, in communications (polarization-maintaining, birefringent fibers), and to selectively tap into specific electronic transitions in atomic systems.

All of the properties of the EM field listed thus far are its manipulable degrees of freedom (DOF). And the chief reason we are able to use them in such

manners for simultaneous, multi-channel information transfer without crosstalk or interference is due to our ability to generate and measure orthogonal or nearly-orthogonal states of light within these DOF. A fast enough flip mirror (or an equivalent, temporally modulated electro-optic device) could, in principle, sort pulses of light that are separated in time. A prism, diffraction grating, or specially coated dichroic mirror can deterministically demultiplex different frequency components of a beam. Charge and current-based electronic components can be tuned to resonate at set frequencies, enabling antennas to select for certain wireless bands. Interferometric setups can multiplex OAM modes of distinct spatial parities [26], and simple crystalline devices like polarizers and waveplates can fully resolve the polarization DOF. Orthogonal (defined in Chapter II) field configurations remain orthogonal under lossless, unitary transformations, such as time evolution (propagation) in uniform media. And this very orthogonality allows for the existence of physical devices for highly selective, deterministic manipulation and detection of these modes.

Temporal Modes and the Quantum Pulse Gate

Two pulsed modes of light can be orthogonal, and hence deterministically separable, in various ways. They could be in spatially distinct beams, or have the value of the overlap integral between their transverse mode functions be zero. They could have perpendicular polarizations, or have non-overlapping frequency spectra (be of distinguishable colors). Or the pulses could literally be separated in time by a large delay. However, the pulsed modes by definition have well-defined, complex functions characterizing their longitudinal pulse shapes. Therefore, two modes that are fully overlapping in time in the same beam with the same transverse

profiles, polarization states, and spectral frequency bands, can still be orthogonal by dint of possessing orthogonal longitudinal shapes [27]. We call such modes temporal modes (TM) [28].

Temporal modes are sometimes also called wave-packet modes. They are a generalization of time-frequency bins, and can be decomposed as coherent superpositions of temporally and/or spectrally disjoint modes [17, 27]. Since they are defined by continuous functions, they span a vector space with potentially very high dimensionality, which makes them particularly advantageous for quantum information encoding. Physical laws, and specifically quantum mechanics, allows for the existence of unitary transformations that can deterministically sort and manipulate user-defined temporal-mode components of light. We call a device that can be programmed to selectively multiplex a TM of choice, a "quantum pulse gate" (QPG) [29, 30]. Figure 2 portrays a schematic operation of a QPG.

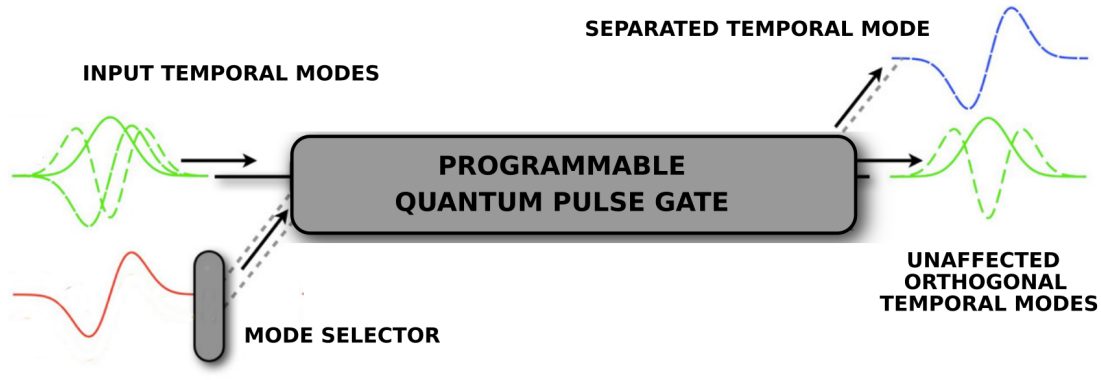

FIGURE 2. Schematic of operation of the ideal quantum pulse gate. The device can be programmed to selectively "drop" arbitrarily shaped temporal-mode components with high efficiency without contamination from the orthogonal subspace.

Optical system designs unavoidably have to account for longitudinal mode structure. Light emitted from optical quantum memories such as ion-doped solid state crystalline wafers or fibers, trapped ultracold atoms, gaseous ensembles,

or even storage cavities [31, 32], has a characteristic shape and temporal width dictated by the linewidths or decay rates of the listed media. By time-reversal symmetry, there is an optimum temporal mode shape and width that maximizes light storage efficiency in the same media. Photon pair sources, which are valuable for quantum optical setups, are often engineered to either eliminate entanglement in the temporal mode basis to ensure the heralding of pure single-photon states [33], or maximize it to exploit time-frequency entanglement as a resource [34, 35]. While the use of temporal modes cannot violate the Shannon limit for classical bandwidth capacity [36], the increased dimensionality offers advantages in the quantum realm, including an improved security for quantum-key distribution [37]. All of these applications would benefit from a practical QPG device.

To date, all attempts at realizing a QPG have relied on parametric nonlinear processes that are pumped with time-varying control fields. For example, all optical quantum memory protocols consist of a medium with multi-level internal electronic states, and an input optical signal is meant to be stored in a collective excitation of such states. This transfer is typically mediated by the presence of a control field, which is usually a combination of strong lasers, or externally applied EM radio-frequency (RF) fields [38]. Another example is frequency conversion of an optical signal by three-wave or four-wave mixing in nonlinear transparent media, also mediated by laser control fields (called pumps) [39]. The storage/retrieval or frequency conversion efficiencies of these parametric processes become sensitive to the temporal mode structure of the input optical signal when the control fields are pulsed (varying with time). This has prompted significant attention and research into the potential utilization of parametrically pumped processes as QPGs.

The ideal QPG must satisfy two conditions: 1) It must fully separate the desired TM component, and 2) it must avoid contamination from orthogonal TM components. When both of these are met, the QPG is said to have unit selectivity (defined in Chapter IV). All previous efforts at achieving a QPG have failed at simultaneously meeting both conditions. There exists a fundamental limit to selectivity of QPGs based on traveling-wave interactions in media with simple dispersion profiles, and the purpose of this dissertation is to quantify this limit, explain it, and overcome it in theory and in practice, thus paving the way towards a perfectly selective quantum pulse gate.

The material presented in this dissertation includes published co-authored material. Specifically, Chapter VI contains text, equations, and figures from [40–42], and equations from [43]. Chapter V contains text, equations, figures, and data presented in [44]. And Chapter VI contains text from the 'applications' section of [28], as well as a concept from [45]. I fully acknowledge my fellow co-authors Dr. Lasse Mejling, Prof. Karsten Rottwitt, Dr. Colin J. McKinstrie, Dr. Benjamin Brecht, Prof. Christine Silberhorn, Dr. Jesper B. Christensen, and Prof. Michael G. Raymer for their roles in these publications.

Outline

In Chapter II, I go over the classical and quantum theory of electromagnetic fields. I also fully define temporal modes and their quantum operators, thus putting them on firm mathematical footing.

Chapter III covers a discussion of dispersion and second-order optical nonlinearity in non-centrosymmetric crystalline media. I consider three-wave

mixing in the context of sum-frequency and difference-frequency generation in the strong pump limit. I derive the equations of motion for pulsed operation.

The equations of motion previously derived are interpreted more abstractly to represent general parametrically pumped processes in Chapter IV. They are solved numerically for diverse sets of parameters, and analytically for special parameter regimes. Their performance as a selective QPG is quantified and the selectivity limit explained. This chapter also contains our method to overcome the selectivity limit via temporal-mode interferometry. It ends with a generalization to four-wave mixing.

In Chapter V, I introduce our experimental setups, and justify our choices for systems and parameters. I showcase certain innovative physical constructions, and verify the theory predictions with measurements for both single-stage and dual-stage frequency conversion.

And finally in Chapter VI, I suggest improvements to the technique, and layout a research plan to carry the work forward. I close with a list of myriad QPG applications that are now rendered within reach.

CHAPTER II

CLASSICAL AND QUANTUM THEORY OF LIGHT

Maxwell's Equations and Classical-Mode Concepts

Here I lay out the classical equations of motion governing the behavior of electromagnetic fields, and introduce basic concepts required for the descriptions that follow. These equations were first expressed together by Maxwell in 1873 [8]. They couple two vector fields, namely, the electric field $[\mathbf{E}(\mathbf{r},t)]$ and the magnetic field $[\mathbf{B}(\mathbf{r},t)]$, to source terms, and to each other. They relate their temporal evolution to their local spatial variations. They may be presented concisely in free space as

$$\nabla \cdot (\epsilon_0 \mathbf{E}) = \rho, \tag{2.1}$$

$$\nabla \times \frac{\mathbf{B}}{\mu_0} = \mathbf{J} + \frac{\partial(\epsilon_0 \mathbf{E})}{\partial t}, \tag{2.2}$$

$$\nabla \cdot \mathbf{B} = 0, \tag{2.3}$$

$$\nabla \times \mathbf{E} = -\frac{\partial \mathbf{B}}{\partial t}. \tag{2.4}$$

Here, and in the rest of this document, I use a bold font to denote three-dimensional vectors. The source terms $\rho(\mathbf{r})$ and $\mathbf{J}(\mathbf{r})$ are the charge and current densities, respectively. The fundamental constants ϵ_0 and μ_0 are respectively called the permittivity and the permeability of free space. A cursory counting of the number of constraints versus the number of field parameters would reveal that this particular parameterization is redundant. A reduction is possible if we were

to employ the scalar and vector potential notation [46]. But I will refrain for the sake of simplicity.

While Eqs. 2.1-2.4 govern the effect of sources on fields, for the converse, we would need to refer to the Lorentz force equation,

$$\mathbf{F} = q[\mathbf{E} + \mathbf{v} \times \mathbf{B}], \tag{2.5}$$

which yields the force $\mathbf{F}$ on a point charge q moving with velocity $\mathbf{v}$ due to the local electric and magnetic fields.

I will now consider the fields in free space without any source terms, by setting $\rho = 0$ and $\mathbf{J} = 0$ everywhere. Then, Eqs. 2.1-2.4 can be combined into the form

$$(\nabla^2 - \mu_0\epsilon_0\partial_t^2) \begin{bmatrix} \mathbf{E} \\ \\ \mathbf{B} \end{bmatrix} = 0. \tag{2.6}$$

Here, I am using the short-hand notation for partial derivatives ($\partial_t \equiv \partial/\partial_t$). Equation 2.6 is clearly a three-dimensional wave equation. There are several spatio-temporal field functions that satisfy Eq. 2.6. A primordial one being plane waves,

$$\mathbf{E}(\mathbf{r}, t) = \Re[\hat{\mathbf{e}} E_0 \exp(i\mathbf{k} \cdot \mathbf{r} - i\omega t)], \quad \mathbf{B}(\mathbf{r}, t) = \Re[\hat{\mathbf{e}}' B_0 \exp(i\mathbf{k} \cdot \mathbf{r} - i\omega t)]. \tag{2.7}$$

Physical electric and magnetic fields are taken to be real by convention. The wavenumber is related to the harmonic temporal frequency by $|\mathbf{k}| = \sqrt{\mu_0\epsilon_0}\omega$. The wavefronts traverse through space in the direction of the momentum vector $\mathbf{k}$ at the speed of light $c = 1/\sqrt{\mu_0\epsilon_0}$. The unit vectors $\hat{\mathbf{e}}$ and $\hat{\mathbf{e}}'$ denote the field

polarizations, and the divergence relations in Eqs. 2.1 and 2.3 demand that the polarizations be transverse to the direction of propagation:

$$\mathbf{k} \cdot \hat{\mathbf{e}} = 0, \quad \mathbf{k} \cdot \hat{\mathbf{e}}' = 0. \tag{2.8}$$

Furthermore, the curl Eqs. 2.2 and 2.4 restrict $\mathbf{E}$ and $\mathbf{B}$ to be perpendicular,

$$\hat{\mathbf{e}}' B_0 = \sqrt{\mu_0 \epsilon_0} \frac{\mathbf{k}}{|\mathbf{k}|} \times \hat{\mathbf{e}} E_0. \tag{2.9}$$

The canonical plane wave is characterized by a momentum vector $\mathbf{k}$, an amplitude E_0, and a polarization direction, which is contained in a two-dimensional space perpendicular to the specified momentum. All solutions to Eq. 2.6 with free-space boundary conditions may be expressed as linear superpositions of plane waves.

The derivation (and listed consequences) only applies to free space and to media with spatially uniform permittivities ϵ and permeabilities μ. To solve Maxwell's equations in nonuniform and/or in non-isotropic media, one would have to solve them in the Fourier domain, and apply the divergence and curl operators to the medium properties as well. Several claims about the relative orientations of vectors made thus far are not true in such general cases. That theory is beyond the scope of this thesis.

Plane waves have infinite transverse extents. They are neither the only, nor the most convenient mode decomposition for the electromagnetic field in many practical contexts. Typical optical laboratory setups, for example, involve lasers and beams of light being steered along effectively straight paths using mirrors, lenses, and other such elements. For such configurations, one applies the paraxial approximation to make the transverse field profile separable from its longitudinal

(say z) periodic functional dependence. Popular choices for mode functions include Hermite-Gaussian beams, Laguerre-Gaussian beams, and Bessel beams. This project predominantly deals with linearly polarized, compact free space beams, where most of the beam intensity ($\propto |\mathbf{E}|^2$) is confined close to the principle axis, with a single maximum in the transverse plane. The field amplitude for such beams can be approximated well by the fundamental, transverse-electromagnetic (TEM_{00}) Gaussian mode,

$$\mathbf{E}(r,z,t) = \Re\left[E_0\hat{\mathbf{e}}\frac{w_0}{w(z)}\exp\left(\frac{-r^2}{w(z)^2}\right)\exp\left(i\left(kz + k\frac{r^2}{2R(z)} - \psi(z) - \omega t\right)\right)\right], \tag{2.10}$$

where r is the radial distance from the principle axis, z is the axial distance from the beam's focal point, $k = 2\pi/\lambda$ is the wavenumber, $w(z)$ is the spot size, or radius at which the field amplitudes fall to $1/e$ of their axial values, $w_0 = w(0)$ is the waist radius, $R(z)$ is the radius of curvature of the beam's wavefronts, and $\psi(z)$ is the extra Gouy phase attributable to the phase velocity of light. The spot size, curvature, and the Gouy phase are all related to the Rayleigh range ($z_R = \pi w_0^2/\lambda$) by

$$w(z) = w_0\sqrt{1 + \left(\frac{z}{z_R}\right)^2}, \quad R(z) = z\left[1 + \left(\frac{z_R}{z}\right)^2\right], \quad \psi(z) = \arctan\left(\frac{z}{z_R}\right). \tag{2.11}$$

For a given wavelength, a Gaussian beam is fully characterized by its waist radius (w_0), or equivalently by its Rayleigh range (z_R). When this beam is refocused by a lens, these properties are altered, resulting in a different Gaussian beam. Cylindrical lenses can be employed to selectively operate on specific-transverse

axes independently. As illustrated in Fig. 3, the Rayleigh range is the length along which the beam behaves as effectively collimated, with minimal wavefront curvature. This range is larger for beams with a larger waist. I exploit all of these features in our experimental setup to treat a wide optical beam as a plane wave incident on a grating-based system (Chapter V).

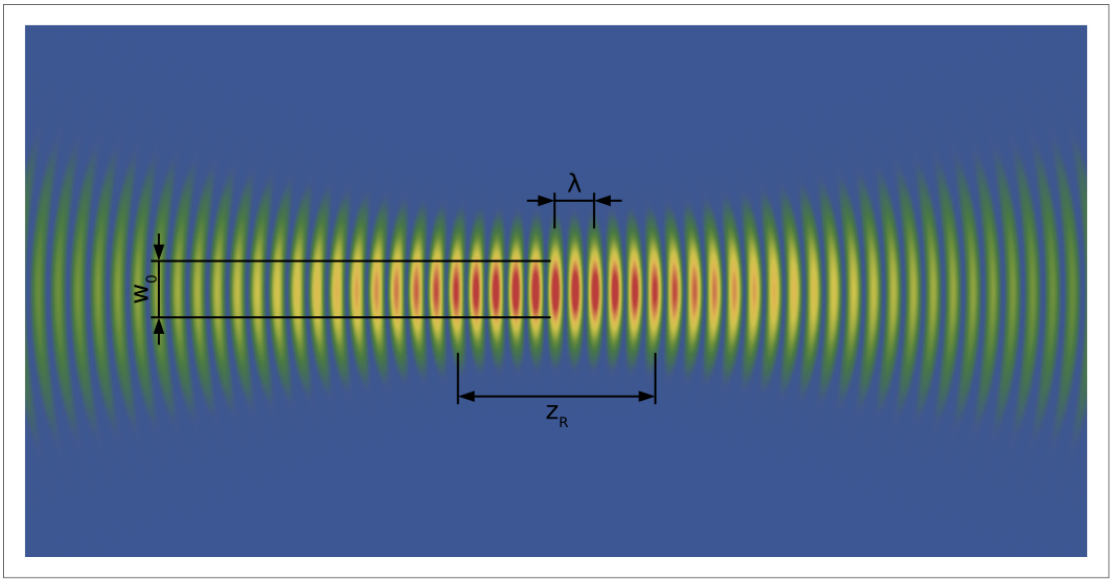

FIGURE 3. Instantaneous (in time) spatial intensity profile of a Gaussian beam with its principle axis along the z-direction. The wavelength (λ), waist radius (w_0), and the Rayleigh range (z_R) are also indicated.

This project will also involve discussion and use of waves that traverse apparatuses specially designed to guide them along predetermined paths. They are called waveguides, and they could take the form of silica fibers, or few-micron-size channels etched into crystalline wafer substrates. Waveguides rely on refractive index contrasts (encoded in the permittivity) between the guiding core and the adjacent "cladding" material, and use either total internal reflection, or photonic-crystal mediated interference effects to achieve guidance. The guided modes for a given waveguide geometry can be found by solving Maxwell's equations with the

transverse index-boundary field-continuity conditions. Figure 4 shows the typical transverse intensity profiles for fundamental guided modes in a simple geometric ridge waveguide.

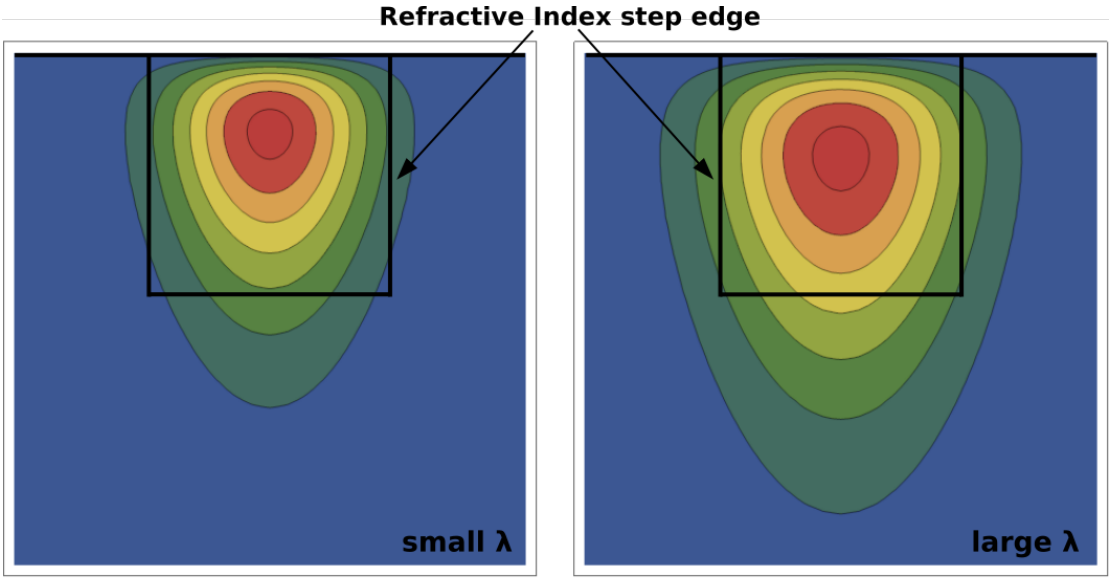

FIGURE 4. Fundamental guided-mode transverse intensity profiles for square channel waveguides at two different wavelengths.

Every mode function introduced thus far in this section has been monochromatic. They have all been continuous waves of a single wavelength and infinite longitudinal extent. Introduction of explicit temporal modulation to the wave amplitude will widen the frequency spectrum. Electromagnetic pulses can indeed be represented as a weighted superposition of a continuum of monochromatic modes with the same transverse geometry. If the pulse duration is much longer than the oscillation frequency (or equivalently, the longitudinal-spatial extent much larger than the wavelength), then we can use the slowly-varying-envelope approximation, and represent the longitudinal mode structure as a product of a primary carrier wave with the central frequency, and an amplitude envelope function,

$$\mathbf{E}(z,t) = \Re[\hat{\mathbf{e}} E_0(t) \exp[i(k_0 z - \omega_0 t)]], \quad \omega_0 = ck_0, \tag{2.12}$$

where the transverse mode structure is not shown. The frequency spectrum of such a pulse would be the Fourier transform of the envelope function $[E_0(t)]$ shifted to the central frequency ω_0. Figure 5 illustrates an example of a pulsed mode with a slowly varying envelope, as well as it's frequency spectrum.

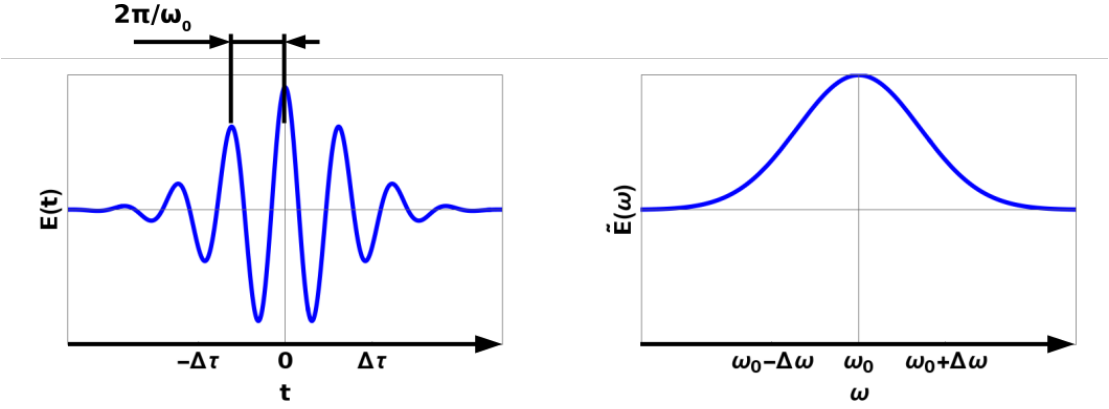

FIGURE 5. Figure showing the time-domain function of an electric field pulse $E(t)$, and the corresponding frequency spectrum $\tilde{E}(\omega)$. Here, $\Delta\tau\Delta\omega = 2\pi$.

Electromagnetic Field Quantization

I start by following the prescription for monochromatic-mode field quantization, first layed out in [47], and summarized in [48]. The classical electromagnetic field Hamiltonian in free space is

$$H = \frac{\epsilon_0}{2} \int d^3r [E^2 + c^2 B^2], \tag{2.13}$$

where $E = |\mathbf{E}|$ and $B = |\mathbf{B}|$. Since the Hamiltonian is quadratic in the canonical fields, this is a linear field theory [48], meaning that the Hamiltonian equations of

motion are linear differential equations. we can therefore express the fields as a superposition of a set of noninteracting normal modes (such as plane waves). We can then apply the same general quantization procedure for all the modes. Using an arbitrary mode decomposition, the monochromatic (eigensolution) field for a single mode can be expressed as

$$\mathbf{E}(\mathbf{r},t) = \alpha(t)\mathbf{f}(\mathbf{r}) + \text{c.c.} = \alpha(0)\exp(-i\omega t)\mathbf{f}(\mathbf{r}) + \text{c.c.} \tag{2.14}$$

The symbol 'c.c.' stands for complex conjugate. This separation of space and time variables is valid since $\mathbf{E}(\mathbf{r},t)$ satisfies the wave equation. The spatial mode function $\mathbf{f}(\mathbf{r})$ is asssumed to be normalized, and obeys the following constraints

$$\int d^3r|\mathbf{f}(\mathbf{r})|^2 = 1, \quad (\nabla^2 + k^2)\mathbf{f}(\mathbf{r}) = 0, \tag{2.15}$$

where $k = \omega/c$. By applying Maxwell's equations (Eqs. 2.1-2.4) to the Hamiltonian, one can trivially show that

$$H = 2\epsilon_0|\alpha(t)|^2. \tag{2.16}$$

This harmonic expression prompts the elevation of the temporal part of the field to an annihilation operator,

$$\alpha(0) \to i\sqrt{\frac{\hbar\omega}{2\epsilon_0}}\hat{a}, \tag{2.17}$$

resulting in the following harmonic-oscillator Hamiltonian,

$$\hat{H} = \frac{\hbar\omega}{2}(\hat{a}^\dagger\hat{a} + \hat{a}\hat{a}^\dagger) = \hbar\omega\left(\hat{a}^\dagger\hat{a} + \frac{1}{2}\right), \tag{2.18}$$

by utilizing the commutation relation $[\hat{a}, \hat{a}^\dagger] = 1$. We can write the quantum fields for this single mode in some volume V as

$$\hat{\mathbf{E}}(\mathbf{r}, t) = i\sqrt{\frac{\hbar\omega}{2\epsilon_0}}\mathbf{f}(\mathbf{r})\hat{a}\exp(-i\omega t) + \text{H.c.}, \tag{2.19}$$

$$\hat{\mathbf{B}}(\mathbf{r}, t) = \sqrt{\frac{\hbar}{2\omega\epsilon_0}}[\nabla \times \mathbf{f}(\mathbf{r})]\hat{a}\exp(-i\omega t) + \text{H.c.} \tag{2.20}$$

The text 'H.c.' stands for Hermitian conjugate. The Hermitian field operators, which measure real quantities, are often separated into positive-frequency and negative-frequency parts thusly:

$$\hat{\mathbf{E}}(\mathbf{r}, t) = \hat{\mathbf{E}}^{(+)}(\mathbf{r}, t) + \hat{\mathbf{E}}^{(-)}(\mathbf{r}, t), \qquad \hat{\mathbf{E}}^{(-)}(\mathbf{r}, t) = [\hat{\mathbf{E}}^{(+)}(\mathbf{r}, t)]^\dagger, \tag{2.21}$$

$$\hat{\mathbf{B}}(\mathbf{r}, t) = \hat{\mathbf{B}}^{(+)}(\mathbf{r}, t) + \hat{\mathbf{B}}^{(-)}(\mathbf{r}, t), \qquad \hat{\mathbf{B}}^{(-)}(\mathbf{r}, t) = [\hat{\mathbf{B}}^{(+)}(\mathbf{r}, t)]^\dagger. \tag{2.22}$$

We can write all equations using just the negative-frequency operators for notational convenience.

To generalize this treatment to many modes, I use the fact that there are orthonormal modes fully characterized by the wave vector $\mathbf{k}$ and a bi-valued index for polarization $\sigma = \pm 1$. We can then define a complete set of orthonormal mode functions $\mathbf{f}_{\mathbf{k},\sigma}(\mathbf{r})$, satisfying

$$\int_V \mathbf{f}_{\mathbf{k},\sigma}(\mathbf{r}) \cdot \mathbf{f}^*_{\mathbf{k}',\sigma'}(\mathbf{r}) = \delta_{\sigma,\sigma'}\delta^3(\mathbf{k} - \mathbf{k}'), \tag{2.23}$$

where V is the quantization volume, and $\delta_{\sigma,\sigma'}$ is the Kronecker delta function. The orthogonality of these mode functions implies that they evolve as independent

harmonic oscillators, as indicated by the resulting form of the Hamiltonian operator,

$$\hat{H} = \sum_{\mathbf{k},\sigma} \hbar\omega_{\mathbf{k}} \left(\hat{a}^{\dagger}_{\mathbf{k},\sigma} \hat{a}_{\mathbf{k},\sigma} + \frac{1}{2} \right), \quad [\hat{a}_{\mathbf{k},\sigma}, \hat{a}^{\dagger}_{\mathbf{k}',\sigma'}] = \delta_{\sigma,\sigma'} \delta^3(\mathbf{k} - \mathbf{k}'), \tag{2.24}$$

where $\omega_{\mathbf{k}} = c|\mathbf{k}|$. The total field operators are then the sum over the individual field-mode operators,

$$\hat{\mathbf{E}}^{(+)}(\mathbf{r}, t) = i \sum_{\mathbf{k},\sigma} \sqrt{\frac{\hbar\omega_{\mathbf{k}}}{2\epsilon_0}} \mathbf{f}_{\mathbf{k},\sigma}(\mathbf{r}) \hat{a}_{\mathbf{k},\sigma} \exp(-i\omega_{\mathbf{k}} t), \tag{2.25}$$

$$\hat{\mathbf{B}}^{(+)}(\mathbf{r}, t) = \sum_{\mathbf{k},\sigma} \sqrt{\frac{\hbar}{2\omega_{\mathbf{k}}\epsilon_0}} [\nabla \times \mathbf{f}_{\mathbf{k},\sigma}(\mathbf{r})] \hat{a}_{\mathbf{k},\sigma} \exp(-i\omega_{\mathbf{k}} t). \tag{2.26}$$

Now we can expand the quantization volume V to cover all of space, and replace the sums over the wave vectors with integrals over momentum- or k-space. This continuum limit will introduce factors of 2π to the commutators and the integrands. For concreteness, a popular choice for orthonormal sets of monochromatic modes are the plane waves,

$$\mathbf{u}_{\mathbf{k},\sigma}(\mathbf{r}) = \mathbf{e}_{\mathbf{k},\sigma} \exp(i\mathbf{k} \cdot \mathbf{r}). \tag{2.27}$$

The field operators then become

$$\hat{\mathbf{E}}^{(+)}(\mathbf{r},t) = i\sum_{\sigma}\int \frac{d^3k}{(2\pi)^3}\sqrt{\frac{\hbar ck}{2\epsilon_0}}\hat{a}_{\mathbf{k},\sigma}\mathbf{u}_{\mathbf{k},\sigma}(\mathbf{r})\exp\left(-i\omega_{\mathbf{k}}t\right), \tag{2.28}$$

$$\hat{\mathbf{B}}^{(+)}(\mathbf{r},t) = i\sum_{\sigma}\int \frac{d^3k}{(2\pi)^3}\sqrt{\frac{\hbar ck}{2\epsilon_0}}\hat{a}_{\mathbf{k},\sigma}\left(\frac{\mathbf{k}}{ck}\times\mathbf{u}_{\mathbf{k},\sigma}(\mathbf{r})\right)\exp\left(-i\omega_{\mathbf{k}}t\right), \tag{2.29}$$

and the corresponding normalization conditions, and the commutators are

$$\int d^3r\mathbf{u}_{\mathbf{k},\sigma}(\mathbf{r})^*\cdot\mathbf{u}_{\mathbf{k}',\sigma'}(\mathbf{r}) = (2\pi)^3\delta^{(3)}(\mathbf{k}-\mathbf{k}')\delta_{\sigma,\sigma'}, \quad \left[\hat{a}_{\mathbf{k},\sigma},\hat{a}^{\dagger}_{\mathbf{k}',\sigma'}\right] = (2\pi)^3\delta^{(3)}(\mathbf{k}-\mathbf{k}')\delta_{\sigma,\sigma'}. \tag{2.30}$$

Wave-packet modes

The monochromatic plane-wave creation and annihilation operators ($\hat{a}^{\dagger}_{\mathbf{k},\sigma}$ and $\hat{a}_{\mathbf{k},\sigma}$, respectively) can operate on the quantum vacuum state of the electromagnetic field to create or destroy single-quanta of field excitation, just as in the case of a simple harmonic oscillator,

$$\hat{a}^{\dagger}_{\mathbf{k},\sigma}|0\rangle = |1\rangle_{\mathbf{k},\sigma}, \quad \hat{a}_{\mathbf{k},\sigma}|1\rangle_{\mathbf{k},\sigma} = |0\rangle_{\mathbf{k},\sigma}. \tag{2.31}$$

The state $|n\rangle_{\mathbf{k},\sigma}$ (where $n > 0$), which can be created by n successive creation operators acting on the vacuum, for example, is identified as the n-photon Fock state in the defined plane-wave mode.

But the choice of plane waves, or even monochromatic modes was not necessitated by physical constraints. One may also expand the same fields in terms of non-orthogonal, non-monochromatic, spatial-temporal modes $\mathbf{v}_{j,\sigma}(\mathbf{r},t)$

[17, 27]. These wave-packet modes are related to the orthogonal, monochromatic, plane-wave modes through the non-unitary transformation

$$\mathbf{v}_{j,\sigma}(\mathbf{r},t) = i\sqrt{\frac{\hbar c}{2\epsilon_0}}\int \frac{d^3k}{(2\pi)^3}\sqrt{k}U_j^{(\sigma)}(\mathbf{k})\mathbf{u}_{\mathbf{k},\sigma}(\mathbf{r})\exp\left(-i\omega_{\mathbf{k}}t\right), \tag{2.32}$$

in which $U_j^{(\sigma)}(\mathbf{k})$ is a unitary transformation 'matrix.' This relation is a spatial Fourier transform. We can call $\mathbf{v}_{j,\sigma}(\mathbf{r},t)$ the wave-packet (WP) modes. For fixed value of σ,

$$\sum_j [U_j^{(\sigma)}(\mathbf{k}')]^* U_j^{(\sigma)}(\mathbf{k}) = (2\pi)^3\delta^{(3)}(\mathbf{k}'-\mathbf{k}), \quad \int \frac{d^3k}{(2\pi)^3}U_j^{(\sigma)}(\mathbf{k})[U_{j'}^{(\sigma)}(\mathbf{k})]^* = \delta_{j,j'}. \tag{2.33}$$

The annihilation and creation operators are changed by the unitary transformation leading to new annihilation and creation operators $\hat{b}_{j,\sigma}$ and $\hat{b}_{j,\sigma}^\dagger$ such that

$$\hat{b}_{j,\sigma} = \int \frac{d^3k}{(2\pi)^3}[U_j^{(\sigma)}(\mathbf{k})]^*\hat{a}_{\mathbf{k},\sigma}, \quad \hat{a}_{\mathbf{k},\sigma} = \sum_j U_j^{(\sigma)}(\mathbf{k})\hat{b}_{j,\sigma}, \quad \left[\hat{b}_{j,\sigma},\hat{b}_{m,\rho}^\dagger\right] = \delta_{j,m}\delta_{\sigma,\rho}. \tag{2.34}$$

In terms of the wave-packet modes, the positive-frequency parts of the electric and magnetic field operators are

$$\hat{\mathbf{E}}^{(+)}(\mathbf{r},t) = \sum_{j,\sigma}\hat{b}_{j,\sigma}\mathbf{v}_{j,\sigma}(\mathbf{r},t), \tag{2.35}$$

$$\hat{\mathbf{B}}^{(+)}(\mathbf{r},t) = \sum_{j,\sigma}\hat{b}_{j,\sigma}\left(\frac{\mathbf{k}_j}{c|\mathbf{k}_j|}\times\mathbf{v}_{j,\sigma}(\mathbf{r},t)\right). \tag{2.36}$$

An important state of light is that in which a single excitation occurs in a given spatio-temporally localized packet. An example is the deterministic generation of a single photon from an atom in a cavity-QED system. If the packet is dispersed spectrally by a prism and detected by an array of photon counters, only one counter will click, although the precise identity of the one that does will be random. Such a state is expressed as

$$|1\rangle_{j,\sigma} = \hat{b}^{\dagger}_{j,\sigma}|\text{vacuum}\rangle = \int \frac{d^3k}{(2\pi)^3} U_j^{(\sigma)}(\mathbf{k})|1\rangle_{\mathbf{k},\sigma}, \tag{2.37}$$

where $|1\rangle_{\mathbf{k},\sigma}$ is a state with a single excitation having particular monochromatic wave vector-polarization state labeled by the pair $(\mathbf{k},\sigma)$. The function $U_j^{(\sigma)}(\mathbf{k})$ fully specifies the state. The relation between the wave-packet modes and the monochromatic modes is not unitary because of the $\sqrt{k}$ factor. Consequently, $\mathbf{v}_{j,\sigma}(\mathbf{r},t)$ do not generally form an orthogonal set under a scalar product defined by the overlap integral. That is,

$$\int d^3r \mathbf{v}_{j,\sigma}(\mathbf{r},t)^* \cdot \mathbf{v}_{m,\sigma}(\mathbf{r},t) = \frac{\hbar c}{2\epsilon_0} \int \frac{d^3k}{(2\pi)^3} k U_j^{(\sigma)}(\mathbf{k})^* U_m^{(\sigma)}(\mathbf{k}) \neq \delta_{j,m}. \tag{2.38}$$

However, for every wave-packet mode, one can define a dual mode

$$\mathbf{v}^D_{j,\sigma}(\mathbf{r},t) = i\sqrt{\frac{2\epsilon_0}{\hbar c}} \int \frac{d^3k}{(2\pi)^3} \frac{1}{\sqrt{k}} U_j^{(\sigma)}(\mathbf{k}) \mathbf{u}_{\mathbf{k},\sigma}(\mathbf{r}) \exp\left(-i\omega_{\mathbf{k}} t\right), \tag{2.39}$$

with the $\sqrt{k}$ in the denominator of the integrand and an inverted constant factor. The dual modes have the following properties,

$$\int d^3r \mathbf{v}^D_{j,\sigma}(\mathbf{r},t)^* \cdot \mathbf{v}_{m,\rho}(\mathbf{r},t) = \delta_{j,m}\delta_{\sigma,\rho}, \tag{2.40}$$

$$\int d^3r \mathbf{v}^D_{j,\sigma}(\mathbf{r},t)^* \cdot \hat{\mathbf{E}}^{(+)}(\mathbf{r},t) = \hat{b}_{j,\sigma}. \tag{2.41}$$

The dual modes and the wave-packet modes form a biorthogonal basis system under a scalar product defined by the regular overlap integral.

If we restrict ourselves to wave-packet modes that are essentially monochromatic carrier waves with slowly varying envelopes, as defined in Eq. 2.12, then the spectra of said modes would be narrowband, and the $U_j^{(\sigma)}(\mathbf{k})$ would only be nonzero around a narrow neighborhood of some central wave vector $\mathbf{k}_0$. Consequently, the spatial mode functions can be considered to be approximately orthogonal under the regular overlap-integral inner-product definition. We would modify Eq. 2.38 thusly:

$$\int d^3r \mathbf{v}_{j,\sigma}(\mathbf{r},t)^* \cdot \mathbf{v}_{m,\sigma}(\mathbf{r},t) \approx \frac{\hbar c|\mathbf{k}_0|}{2\epsilon_0} \int \frac{d^3k}{(2\pi)^3} U_j^{(\sigma)}(\mathbf{k})^* U_m^{(\sigma)}(\mathbf{k}) = \frac{\hbar c|\mathbf{k}_0|}{2\epsilon_0}\delta_{j,m}. \tag{2.42}$$

This lays the basis for temporal modes. It must be noted that the electric field is not the optimum field for quantization in nonlinear optical media, and we would need to use the displacement field instead [49, 50]. The results for free space are not accurate for dispersive media either. Using certain narrowband approximations will allow us to dodge this problem, and result in appropriate modifications to the field-operator prefactors. This will be expounded on in Chapter III.

Some Experimental Quantum Effects

The quantum theory of the electromagnetic field was required to explain physical phenomena that the classical theory could not. A chief historical phenomenon that prompted all of quantum physics is that of blackbody radiation [10]. A modern class of experimental observations that fit the same niche are the Bell's inequality [19] or the CHSH inequality violations [20]. The latter is used as a philosophical linchpin for the nonclassical nature of reality. The both of these aforementioned topics are beyond the scope of this document. I will, however, present some simpler quantum effects to foreshadow a recurring concept.

Photon antibunching

A half-silvered or a partially reflecting mirror transmits some intensity of a beam of light incident on its surface and reflects some of it. If the process were lossless, then due to energy conservation, the total intensities of the two outgoing (transmitted and reflected) beams will equal that of the incoming incident beam. A quantum description of such a mirror would take the form of a unitary operation that linearly couples input modes to output modes [51, 52]. I label these classes of devices beam splitters.

The most basic beam splitters have two input ports and two output ports, and are schematically depicted as in Fig. 6. If we suppress extraneous parameters such as polarization, transverse spatial profiles, *et cetera*, we can use annihilation operators ($\hat{a}_1$, $\hat{a}_2$) and ($\hat{b}_1$, $\hat{b}_2$) to denote the input and output modes respectively. And these modes are related to each other through a 2×2 unitary matrix U,

$$\begin{bmatrix} \hat{a}_1^\dagger \\ \hat{a}_2^\dagger \end{bmatrix} = U \begin{bmatrix} \hat{b}_1^\dagger \\ \hat{b}_2^\dagger \end{bmatrix}, \quad U^\dagger U = \mathbb{I}, \tag{2.43}$$

where $\mathbb{I}$ is the identity matrix. The four complex elements of U are severely constrained by the unitarity condition. If we absorb phase factors into the definitions of the input/output modes, then without much loss of generality, a beam splitter operation can be characterized by two real parameters (τ, ρ). A popular choice for a general beam splitter matrix is

$$U = \begin{bmatrix} \tau & \rho \\ -\rho & \tau \end{bmatrix}, \quad \tau, \rho \in \mathbb{R}, \quad \tau^2 + \rho^2 = 1. \tag{2.44}$$

If the input state were a single quanta of light excited in input-mode: $\hat{a}_1^\dagger|0\rangle$, then the output state after the beam splitter would be a coherent superposition of the two output modes: $(\tau\hat{b}_1^\dagger + \rho\hat{b}_2^\dagger)|0\rangle$. The probability of detecting this photon in the output-port 1 is τ^2, and the same in output-port 2 is ρ^2. In the special case of a 50/50 beam splitter, $\tau = \rho = 1/\sqrt{2}$, making both the probabilities equal.

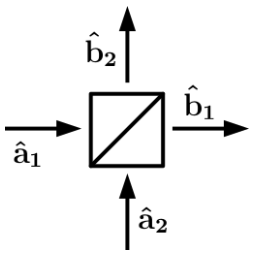

FIGURE 6. Schematic of a beam splitter, with input ($\hat{a}_1$, $\hat{a}_2$) and output ($\hat{b}_1$, $\hat{b}_2$) modes designated.

The key feature to note is that the photon can only be detected once. Therefore, if we were to measure the integrated energy in the two output modes using highly-sensitive detectors, such as photomultiplier tubes, or avalanche

photodiodes in Geiger mode, then for certain input states (such as single photons), we would observe a lack of simultaneous detection events in the two output arms. This "antibunching" effect hints at the partile-like nature of quantum fields, and is used to characterize "sub-Poissonian" sources of light [53], such as quantum dots, diamond NV-centers, and parametrically pumped photon-pair generators.

Mach-Zehnder interferometer with single photons

The negative sign on one of the matrix elements in Eq. 2.44 is a phase factor that is necessary for unitarity. Its effect cannot be measured by using a single beam splitter (and two detectors). We can trivially construct a setup that is sensitive to the relative phase between the two modes of a superposition state by cascading two separate beam splitters where the output ports of one beam splitter is rerouted to the input ports of a second one, as shown in Fig. 7. Such a setup is called a Mach-Zehnder interferometer, and itself has two input ports ($\hat{a}_1$, $\hat{a}_2$) and two output ports ($\hat{c}_1$, $\hat{c}_2$).

Let the unitary matrices representing the two beam splitters in the standard form be characterized by ($\tau^{(1)}$, $\rho^{(1)}$) and ($\tau^{(2)}$, $\rho^{(2)}$), as depicted in Fig. 7. The effect free-space Hamiltonian evolution of the beams inbetween the beam splitters is an overall phase term linearly dependent on distance traversed. I shall denote these phases by (θ_1, θ_2) for paths 1 and 2, respectively. Then, the output modes and the input modes of the interferometer are related to each other by

$$\begin{bmatrix} \hat{a}_1^\dagger \\ \hat{a}_2^\dagger \end{bmatrix} = \begin{bmatrix} \tau^{(1)} & \rho^{(1)} \\ -\rho^{(1)} & \tau^{(1)} \end{bmatrix} \begin{bmatrix} \exp(-i\theta_1) & 0 \\ 0 & \exp(-i\theta_2) \end{bmatrix} \begin{bmatrix} \tau^{(2)} & \rho^{(2)} \\ -\rho^{(2)} & \tau^{(2)} \end{bmatrix} \begin{bmatrix} \hat{c}_1^\dagger \\ \hat{c}_2^\dagger \end{bmatrix} \tag{2.45}$$

$$= \begin{bmatrix} (\tau^{(1)}\tau^{(2)}e^{-i\theta_1} - \rho^{(1)}\rho^{(2)}e^{-i\theta_2}) & (\tau^{(1)}\rho^{(2)}e^{-i\theta_1} + \tau^{(2)}\rho^{(1)}e^{-i\theta_2}) \\ -(\tau^{(1)}\rho^{(2)}e^{-i\theta_2} + \tau^{(2)}\rho^{(1)}e^{-i\theta_1}) & (\tau^{(1)}\tau^{(2)}e^{-i\theta_2} - \rho^{(1)}\rho^{(2)}e^{-i\theta_1}) \end{bmatrix} \begin{bmatrix} \hat{c}_1^\dagger \\ \hat{c}_2^\dagger \end{bmatrix}. \tag{2.46}$$

This implies that an input state of a single photon in mode 1: $\hat{a}_1^\dagger|0\rangle$, would be transformed into a superposition of the two output states: $[(\tau^{(1)}\tau^{(2)}e^{i\Delta\theta} - \rho^{(1)}\rho^{(2)})\hat{c}_1^\dagger + (\tau^{(1)}\rho^{(2)}e^{i\Delta\theta} + \tau^{(2)}\rho^{(1)})\hat{c}_2^\dagger]|0\rangle$, up to an overall phase factor. This means that the probability of detecting this photon in output mode-1 is $P_1 = (\tau^{(1)}\tau^{(2)})^2 + (\rho^{(1)}\rho^{(2)})^2 - 2\tau^{(1)}\tau^{(2)}\rho^{(1)}\rho^{(2)}\cos\Delta\theta$, and the same for output mode-2 is $P_2 = (\tau^{(1)}\rho^{(2)})^2 + (\tau^{(2)}\rho^{(1)})^2 + 2\tau^{(1)}\tau^{(2)}\rho^{(1)}\rho^{(2)}\cos\Delta\theta$. These are sinusoidal functions of the relative phase $\Delta\theta = (\theta_2 - \theta_1)$.

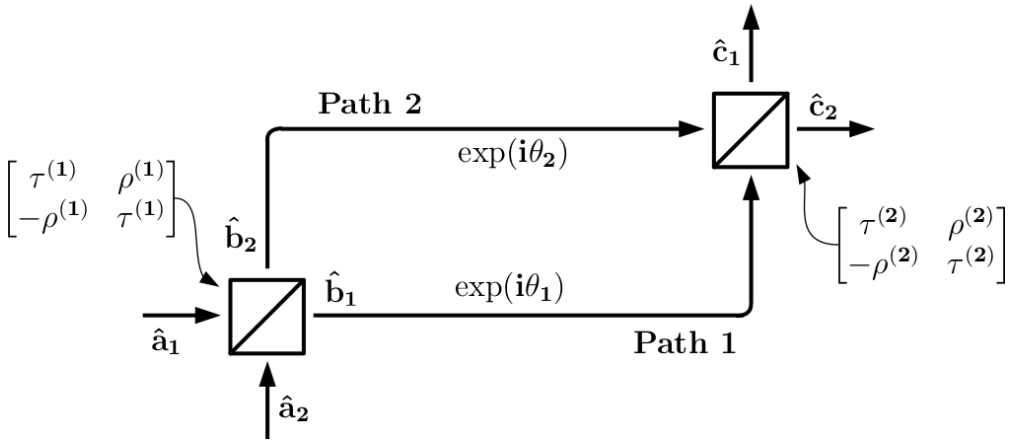

FIGURE 7. A Mach-Zehnder interferometer setup by cascading two beam splitters. Phase accumulated in the intermediate paths is also shown.

Provided that the absolute path difference between paths 1 and 2 does not exceed the coherence length of the input state, we can always pick phase differences

that maximize P_1 and simultaneously minimize P_2, or vice versa. Scanning the phase difference across a continuum of values can confirm the sinusoidal dependence of P_j on $\Delta\theta$. The visibility of these so called "fringe" patterns for outputs 1 and 2 depend on the beam splitter coefficients thusly for a coherent-state input in port 1 and vacuum in port 2:

$$V_1 = \frac{2\tau^{(1)}\tau^{(2)}\rho^{(1)}\rho^{(2)}}{(\tau^{(1)}\tau^{(2)})^2 + (\rho^{(1)}\rho^{(2)})^2}, \quad V_2 = \frac{2\tau^{(1)}\tau^{(2)}\rho^{(1)}\rho^{(2)}}{(\tau^{(1)}\rho^{(2)})^2 + (\rho^{(1)}\tau^{(2)})^2}. \tag{2.47}$$

Here, visibility is defined as the ratio of the difference of the maximum and minimum values of a function to the sum of the same. Both V_1 and V_2 maximize to unity if both beam splitters are 50/50 (i.e. $\tau^{(1)} = \rho^{(1)} = \tau^{(2)} = \rho^{(2)} = 1/\sqrt{2}$). In such a case, a photon incident on, say, the input port 1 can be made to deterministically exit either of the two exit ports, despite the inherent probabilistic nature of detection across individual beam splitters. This effect is contingent on a complete lack of measurement of which path the photon traversed in. The existence of an obstacle in, say, path 1, would completely destroy the interference, even if the photon never interacts with said obstacle. This effect is exploited to make "noninteractive" photonic measurements [54].

Temporal Modes as a Vector Space

Temporal modes (TMs) are a weighted linear superposition of a continuum of monochromatic modes within a neighborhood of some central frequency [28]. While the time-frequency space may be equivalently split into disjoint bins [55],

TMs are exactly orthogonal, and better suited for narrowband integrated systems. TM operators for modes labeled with some index j can be expressed as

$$\hat{A}_j^\dagger = \frac{1}{2\pi}\int d\omega f_j(\omega)\hat{a}^\dagger(\omega) = \int dt \tilde{f}_j(t)\hat{A}^\dagger(t), \tag{2.48}$$

where I have suppressed extraneous beam parameters such as transverse spatial mode and polarization. $\hat{a}^\dagger(\omega)$ is the monochromatic mode photon creation operator, and $\hat{A}^\dagger(t)$ is the photon creation operator at time t. Their commutation relations are $[\hat{a}(\omega), \hat{a}^\dagger(\omega')] = 2\pi\delta(\omega - \omega')$ and $[\hat{A}(t), \hat{A}^\dagger(t')] = \delta(t - t')$. They are related by Fourier transforms,

$$\hat{a}^\dagger(\omega) = \int dt e^{i\omega t}\hat{A}^\dagger(t), \quad \hat{A}^\dagger(t) = \frac{1}{2\pi}\int d\omega e^{-i\omega t}\hat{a}^\dagger(\omega). \tag{2.49}$$

The functions $f_j(\omega)$ are the complex spectral amplitudes of the TMs, while their Fourier transforms $\tilde{f}_j(t)$ are the corresponding temporal pulse shapes. Under the narrow-band approximation that validates Eq. 2.42, we can pick orthogonal TMs by simply choosing a set of mutually orthogonal functions for $f_j(\omega)$. Then, the mode operators would obey standard bosonic commutation relations,

$$\frac{1}{2\pi}\int d\omega f_j^*(\omega)f_k(\omega) = \int dt \tilde{f}_j^*(t)\tilde{f}_k(t) = \delta_{jk} \Rightarrow [\hat{A}_j, \hat{A}_k^\dagger] = \delta_{jk}. \tag{2.50}$$

Figure 8 shows the frequency spectra and the corresponding time-domain electric-field mode amplitudes for an example choice of Hermite-Gaussian pulses as TM shapes. Since the frequency spectra are meant to be overlapping, they are taken to be centered at the same central carrier frequency. This allows us to unique denote each mode by the electric-field temporal envelope function with the carrier

wave factored out. In the case of Fig. 8, these would also be Hermite-Gaussian functions.

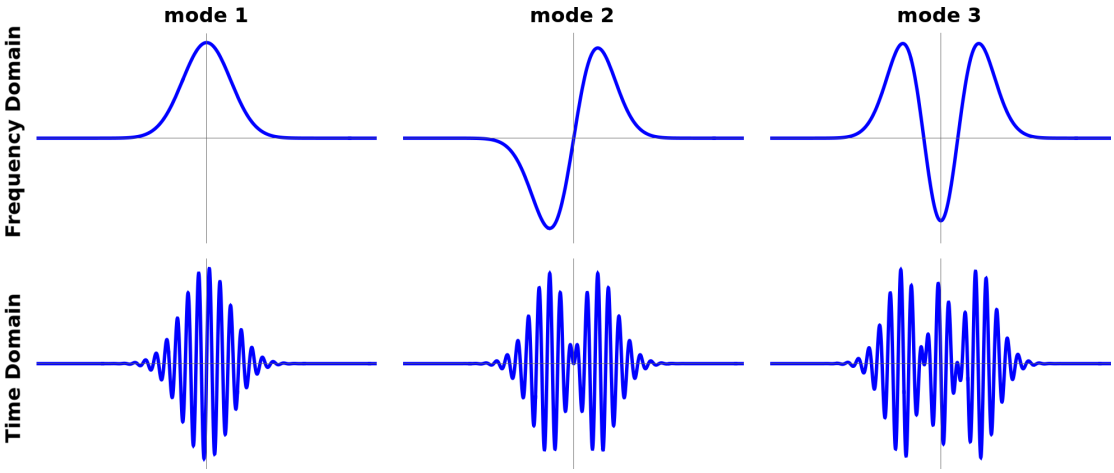

FIGURE 8. The frequency spectra (top row) and the corresponding time-domain field amplitudes (bottom row) for the first three lowest-order Hermite-Gaussian temporal modes.

Well defined continuous complex functions are elements of a vector space over the complex scalar field. With a complete, spanning basis set of TMs, it is possible to decompose any single-photon wave-packet state as a superposition of an arbitrary number of TM states,

$$|\Psi\rangle = \sum_{j=0}^{\infty} c_j \hat{A}_j^{\dagger} |0\rangle, \tag{2.51}$$

where c_j are complex coefficients with the appropriate normalization constraint $\sum_{j=0}^{\infty} |c_j|^2 = 1$. This allows for the treatment of the TM space as a Hilbert space for quantum states. Figure 9 illustrates a standard Bloch sphere for polarization states, and an analogous Bloch sphere constructed for the two-dimensional space formed by two orthogonally shaped TMs.

Figure 10 shows an example set of mutually unbiased TMs generated by superpositions of the three lowest-order Hermite-Gaussian shapes. TMs span an

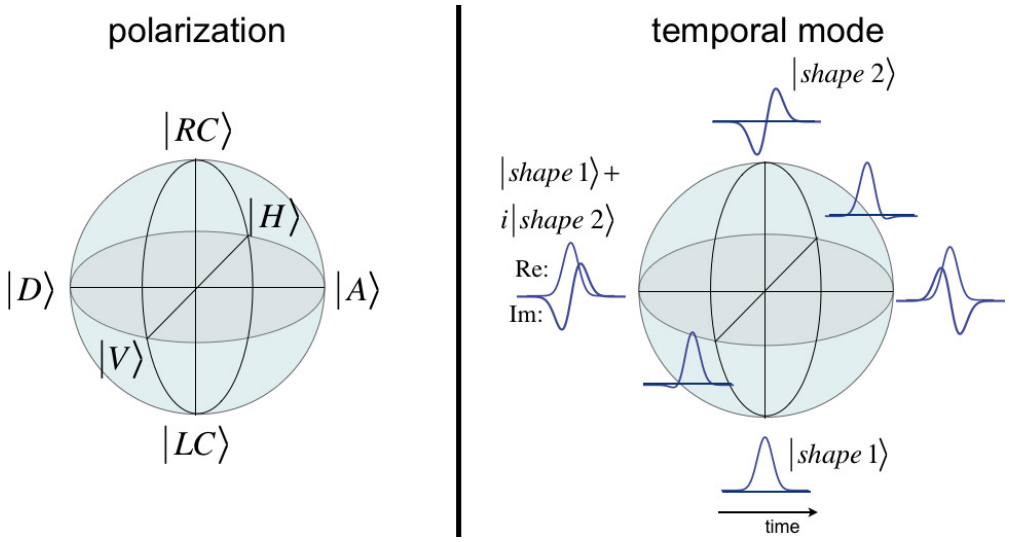

FIGURE 9. Standard polarization Bloch sphere, and the analogous TM Bloch sphere for two chosen orthogonal TM shapes and their linear combinations. The states $|H\rangle$, $|V\rangle$, $|D\rangle$, $|AD\rangle$, $|RC\rangle$, and $|LC\rangle$ stand for horizontal, vertical, diagonal, antidiagonal, right-circular and left-circular polarizated states respectively. Image produced by Prof. M. G. Raymer.

infinite dimensional vector space, although the total dimensionality will be limited by the acceptance bandwidths of the optical devices that will operate on them. This still allows for a very practical implementation of multidimensional qudit style protocols [56–58] in integrated optics systems which typically only support a single transverse guided mode.

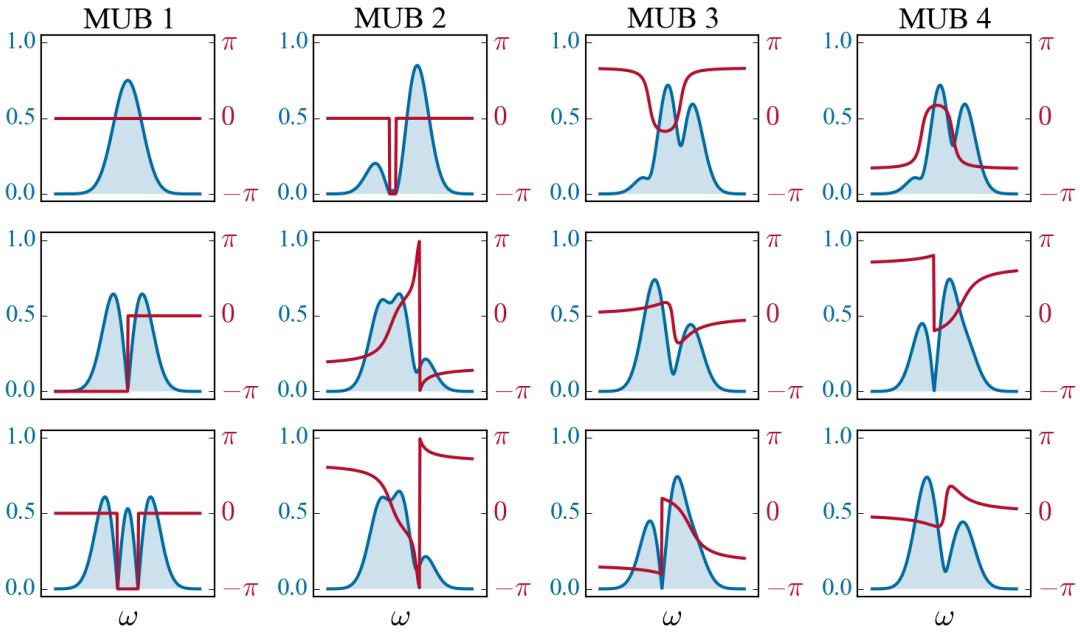

FIGURE 10. Absolute values of amplitudes and phases of four mutually unbiased bases (MUB) sets formed by linear combinations of three mutually orthogonal temporal modes. Image produced by Dr. B. Brecht.

CHAPTER III

NONLINEAR FREQUENCY CONVERSION

Origin of Refractive Index

In Chapter II, the monochromatic plane wave solution to the free space Hamiltonian had the phase form $\exp(i\mathbf{k}\cdot\mathbf{r} - i\omega t)$. Here $|\mathbf{k}| = \omega/c$ was a required constraint. This is the free-space linear dispersion relation between frequency and wave number. In other transparent media such as rare gases (like the atmosphere), liquids or solids, the dispersion relation is far from linear. This is because all electromagnetic waves traversing through the medium will interact with the electrons in the atoms, causing them to accelerate. These in turn function as source terms to the Maxwell's equations (Eqs. 2.1-2.4) and emit waves back into the electromagnetic field. This interplay between the incident and the re-emitted fields often manifests itself as an effective phase shift that is linearly dependent on the distance traversed through the medium. This effect is frequency dependent, and it is captured by a dimensionless material parameter called the refractive index.

Absorption and dispersion

Here, I present the simplified Lorentz model for absorption in a bulk medium. Quantum mechanics predicts that the electrons bound to an atom are restricted to occupy discrete energy levels. And electrons can transition between these levels by emitting or absorbing photons, subject to angular-momentum selection rules and Pauli's exclusion principle. The energy difference between two electronic

excitation levels has to match the energy of the photon for it to mediate the transition. If a photon, or a classical electromagnetic wave, lacked any frequency components close to valid resonant transitions, then the medium would be transparent to it. But the existence of these special "absorption lines" make their presence felt via dispersion.

Consider a bulk medium with only one isolated resonant absorption frequency ω_0. A bound electron under the influence of an oscillating, weak electric field, can then be modeled as a damped harmonic oscillator subject to forced oscillations. If r is the displacement of the electron from equilibrium, then under an electric field E, its equation of motion would be

$$\frac{d^2r}{dt^2} + 2\gamma_D \frac{dr}{dt} + \omega_0^2 r = -\frac{e}{m}E, \tag{3.1}$$

where e and m are the electrons charge and mass, respectively, and γ_D is the damping coefficient. If E is a monochromatic real field, then the solution to Eq. 3.1 is

$$r = -\frac{e}{m}E(\omega)\frac{\exp(-i\omega t)}{\omega_0^2 - 2i\gamma_D\omega - \omega^2} + \text{c.c.} \tag{3.2}$$

Due to the displacement of the negatively charged electron away from equilibrium in a neutral atom, we have induced an oscillating dipole moment. The atom is said to be polarized. In a medium with electron density N, the polarization density P is

$$P = -Ner = \chi^{(1)}(\omega)E(\omega)\exp(-i\omega t) + \text{c.c.} \tag{3.3}$$

A single atom under the influence of an oscillating electric field from a traveling, monochromatic plane wave would therefore oscillate at the same frequency, but at a different phase. Dipole radiation is toroidal, and this would result in the scattering of the incoming wave into arbitrary directions. However, in a bulk medium, the induced dipole moments on all the atoms in the longitudinal path of the incident wave will bear the relative phase imparted on them from said incident wave. Thus, their radiative fields will, in general, constructively interfere in the longitudinally forward direction, and more or less destructively interfere in transverse and backwards directions. We can speak of an induced polarization field within the bulk of the medium, acting as a source term to the wave equation:

$$\nabla^2\mathbf{E} - \mu_0\epsilon_0\partial_t^2\mathbf{E} = \mu_0\epsilon_0\partial_t^2\mathbf{P}. \tag{3.4}$$

Often, the polarization field $\mathbf{P}$ is expressed in terms of the electric field and the permittivity is modified, $\epsilon = (1 + \chi^{(1)})\epsilon_0$. For a plane wave, the new dispersion relation would then be

$$k = \frac{n(\omega)\omega}{c}, \quad n(\omega) = \sqrt{1 + \chi^{(1)}(\omega)}, \tag{3.5}$$

where $n(\omega)$ is called the refractive index of the material. Figure 11 depicts the frequency dependence of the refractive index in the neighborhood of an absorption line.

Typical dielectric media have several resonance/absorption lines. There is a non-negligible absorption coefficient [imaginary part of $n(\omega)$] for the electromagnetic wave close to an absorption frequency, which is beyond the scope of this document. I will restrict myself to frequencies that are far off resonance,

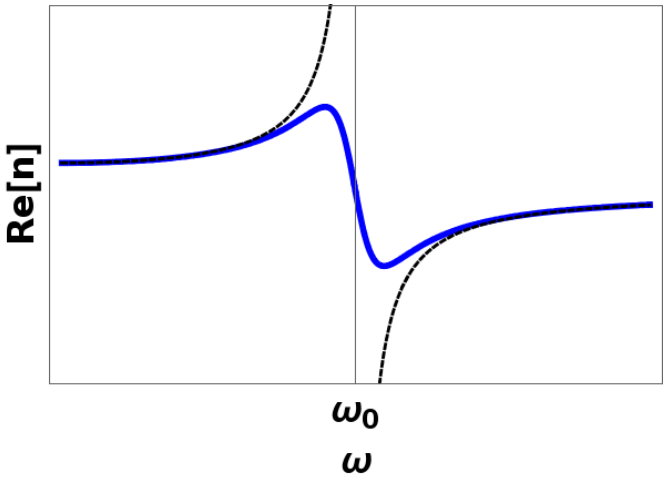

FIGURE 11. Real part of refractive index near a resonant-absorption frequency ω_0. The dotted curve is without damping.

where the medium is transparent to good approximation. The dependence of induced polarization in the medium on the electric field can also depend on the orientation of the electric field relative to some crystal-lattice axis. Figure 12 shows an example of this for lithium niobate, where the two curves are for orthogonal polarization orientations.

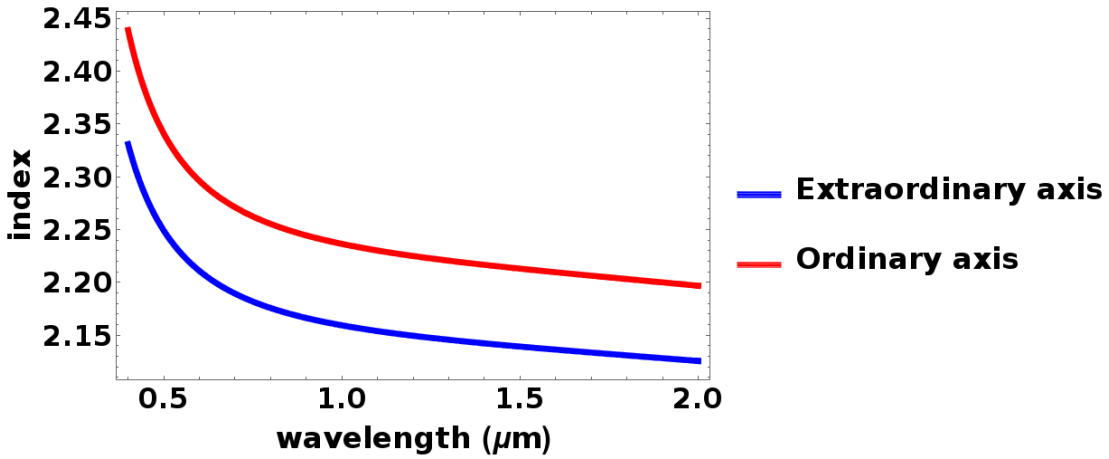

FIGURE 12. Lithium niobate (LN) bulk dispersion curves for two separate polarization directions. This is representative of the typical normal dispersion in both bulk crystals and waveguides.

Field-quantization of temporal modes with dispersion

Dispersion presents a challenge for field quantization, as there is no way to define local energy density [59, 60]. One way to work around this is to restrict ourselves to narrow spectral bands. I shall split the frequency axis into bands B_j centered at ω_j. The bands are assumed to be narrow enough such that we only need consider the slopes of the dispersion, and neglect second-order dispersion (also called group-velocity dispersion). I will capture the transverse spatial profiles into a mode function, and only quantize in the longitudinal direction z. After enumerating modes in a quantization volume (length L), I take the continuum limit thusly:

$$\sum_n \to \frac{L}{2\pi}\int dk, \quad k_n \to k, \quad \omega_n \to \omega(k), \tag{3.6}$$

$$\sum_m [\hat{a}_m, \hat{a}^\dagger_{m'}] = \sum_m \delta_{m,m'} = 1 \to \frac{L}{2\pi}\int dk [\hat{a}(k), \hat{a}^\dagger(k)] = 1. \tag{3.7}$$

We can define new operators $\hat{b}(k) = \sqrt{L}\hat{a}(k)$ such that $[\hat{b}(k), \hat{b}^\dagger(k')] = 2\pi\delta(k-k')$. The electric field in band B_j then becomes

$$\hat{\mathbf{E}}^{(+)}_j = i\int\limits_{B_j} \frac{dk}{2\pi}\sqrt{\frac{\hbar\omega(k)}{2\epsilon(\omega(k))}}\hat{b}(k)\exp[i(kz-\omega(k)t)]\mathbf{u}(x,y,k). \tag{3.8}$$

Note that the quantization length L does not appear in Eq. 3.8. Going forward, I prefer to use ω as the continuous variable, as it is a direct measurable, independent of the medium. If we define group velocity as the inverse of the slope of dispersion ($v_{g,j} = d\omega/dk|_{\omega_j}$), we can then change integration variables,

$$dk = \left.\frac{dk}{d\omega}\right|_{\omega_j} d\omega = \frac{1}{v_{g,j}} d\omega, \quad \mathbf{u}(x,y,k) \equiv \bar{\mathbf{u}}(x,y,\omega). \tag{3.9}$$

I define $\hat{a}_j(\omega) \equiv \sqrt{v_{g,j}}\hat{b}_j(k)$ for the band B_j. The commutation relations are $[\hat{a}_j(\omega), \hat{a}_k^\dagger(\omega')] = 2\pi\delta_{j,k}\delta(\omega - \omega')$. The field operator then becomes

$$\hat{\mathbf{E}}_j^{(+)}(\mathbf{r},t) = i \int\limits_{B_j} \frac{d\omega}{2\pi} \sqrt{\frac{\hbar\omega}{2\epsilon(\omega)v_{g,j}}} \hat{a}_j(\omega) \exp[i(k(\omega)z - \omega t)] \bar{\mathbf{u}}(x,y,\omega). \tag{3.10}$$

Temporal mode operators contained within the B_j band can then be defined as weighted superpositions of $\hat{a}_j(\omega)$ in the usual way covered in Chapter II. It is worth explicitly stating that $\hat{a}_j(\omega)$ are nonlocal quantities. This description is only good for treating travel through dispersive media (and even nonlinear interband interactions) as scattering problems, and used to decompose input and output states. We can, however, define the total energy in the quantization volume within the band B_j as

$$H_{B_j} = \frac{1}{2} \int\limits_V d^3r (\epsilon_j \hat{\mathbf{E}}_j^2 + \frac{1}{\mu}\hat{\mathbf{B}}_j^2) \approx \int\limits_V d^3r \epsilon_j \hat{\mathbf{E}}_j^{(+)} \cdot \hat{\mathbf{E}}_j^{(-)} + \text{H.c.}, \tag{3.11}$$

$$= \int\limits_{B_j} \frac{d\omega}{2\pi} \hbar\omega \left(\hat{a}_j^\dagger(\omega)\hat{a}_j(\omega) + \frac{1}{2} \right). \tag{3.12}$$

Wave Mixing

The polarization field induced in a transparent medium due to a monochromatic, sinusoidal plane wave would itself be sinusoidal for the model considered thus far. All of the individual dipoles would oscillate in concert to

emit a plane wave in the forward direction at the same frequency. However, if the incident plane wave were strong enough, the displacement of the individual electrons from their equilibrium positions would exceed the linear harmonic limit, and Eq. 3.1 would have to be modified with anharmonic terms. This can occur due to several factors, be it a directional difference in local Coulombic potential in a crystal lattice, or just the slope of the shielded point-charge potential from the nucleus. We can capture this nonlinearity by Taylor-expanding the electric-field dependence of the polarization field:

$$P = \alpha E(1 + a_1 E + a_2 E^2 + a_3 E^3 + ...). \tag{3.13}$$

Consider only the quadratic term. If two monochromatic traveling waves with frequencies ω_1 and ω_2 were to be incident on such a crystal, then the polarization field will have oscillations at frequency components: 0, $2\omega_1$, $2\omega_2$, $\omega_1 + \omega_2$ and $\omega_1 - \omega_2$. While the DC component only acts as an effective, electric-field-intensity dependent change in refractive index (electrooptic effect), the polarization field can emit electromagnetic energy at the other frequency components, even though those modes had no incident amplitudes to begin with. This, we can see how nonlinearities in the electric-field responses of media can facilitate energy exchange between different frequencies, while the free-space Hamiltonian forbids it.

In general, the nonlinear coefficients in Eq. 3.13 are frequency dependent. As we have already seen, the linear term has the coefficient $\chi^{(1)}(\omega)$. The general second-order term has two arguments,

$$P_{second} = \sum_{n,m} \chi^{(2)}(\omega_n, \omega_m) E(\omega_n) E(\omega_m) \exp[-i(\omega_n + \omega_m)t]. \tag{3.14}$$

Equation 3.14 can mediate interaction between three frequencies: ω_n, ω_m, and $\omega_n + \omega_m$. The class of processes that rely on second-order or $\chi^{(2)}$-nonlinearity is called "three-wave mixing" (TWM). Similarly, third-order or $\chi^{(3)}$-nonlinearity can facilitate four-wave mixing (FWM). These coefficients can be anisotropic, and can mix orthogonally polarized electric-field modes as well. The tensor components, however, are highly constrained by geometric and other permutation-based symmetry relations [61].

As an illustrative example, consider three-wave mixing between three frequencies related arithematically as $\omega_1 + \omega_2 = \omega_3$. Let us ignore the transverse field profiles and consider just the longitudinal complex field amplitudes $E_j(z,t) = \bar{E}_j(z)\exp[-i(k_j z - \omega_j t)]$ for $j \in \{1,2,3\}$. Here, I am solving for the z-dependent amplitudes due to propagation starting from some initial conditions. The polarization components at the three frequencies are

$$P_1(z,t) = \chi^{(2)} E_2^*(z) E_3(z) \exp[-i((k_3 - k_2)z - (\omega_3 - \omega_2)t)], \tag{3.15}$$

$$P_2(z,t) = \chi^{(2)} E_3(z) E_1^*(z) \exp[-i((k_3 - k_1)z - (\omega_3 - \omega_1)t)], \tag{3.16}$$

$$P_3(z,t) = \chi^{(2)} E_1(z) E_2(z) \exp[-i((k_1 + k_2)z - (\omega_1 + \omega_2)t)]. \tag{3.17}$$

The evolution of the polarization components takes the form

$$\frac{\partial^2 P_1}{\partial t^2} = -(\omega_3 - \omega_2)^2 \chi^{(2)} E_2^*(z) E_3(z) \exp[-i((k_3 - k_2)z - (\omega_3 - \omega_2)t)], \tag{3.18}$$

with similar expressions for the other two frequencies. If we use the slowly varying approximation for the electric field amplitudes, we can derive the following:

$$\frac{dE_1(z)}{dz} = -i\frac{2\pi\omega_1^2}{k_1c^2}\chi^{(2)}E_2^*(z)E_3(z)\exp[i(k_3-k_2-k_1)z], \tag{3.19}$$

$$\frac{dE_2(z)}{dz} = -i\frac{2\pi\omega_2^2}{k_2c^2}\chi^{(2)}E_1^*(z)E_3(z)\exp[i(k_3-k_2-k_1)z], \tag{3.20}$$

$$\frac{dE_3(z)}{dz} = -i\frac{2\pi\omega_3^2}{k_3c^2}\chi^{(2)}E_1(z)E_2(z)\exp[i(k_1+k_2-k_3)z]. \tag{3.21}$$

Thus, we see that energy can be exchanged between these three modes. The ω_3 component is different from the other two because it is the sum-frequency component. It can either gain or lose energy from the other two, but cannot mediate energy exchange between the other two. A common trick is to make one of the other two fields (say ω_2-component) very strong relative to the rest. Then we can ignore its variation with respect to z, thus eliminating Eq. 3.20 and substituting a constant amplitude $E_2(z) \rightarrow E_2$ into Eqs. 3.19 and 3.21. Then we would have a situation where modes $E_1(z)$ and $E_3(z)$ are exchanging energy between each other, and the coupling strength is proportional to E_2. This is the basic design for nonlinear frequency conversion. The strong field E_2 is referred to as the pump field. And the mixing fields $E_1(z)$ and $E_3(z)$ are referred to typically as signal and idler fields.

Although the three modes obey energy conservation ($\omega_1 + \omega_2 = \omega_3$), the highly-oscillatory z-phase term in Eqs. 3.19-3.21 can prevent any significant coherent build-up of energy exchange over macroscopic distances. This is due to the traveling waves acquiring phases at different rates due to dispersion. Unless the phase mismatch $\Delta k = k_3 - k_1 - k_2$ can be set to zero (essentially ensuring momentum conservation), our frequency conversion device will not function. Phase matching can sometimes be achieved by employing birefringence of the

medium (see Fig. 12), or by angle-tuning in bulk media. But for single-transverse mode waveguides, a popular way is to periodically switch the sign of the nonlinearity $\chi^{(2)}$ of the medium in the direction of propagation by reorienting the lattice bond directions (Fig. 13). This technique is called quasi-phase matching.

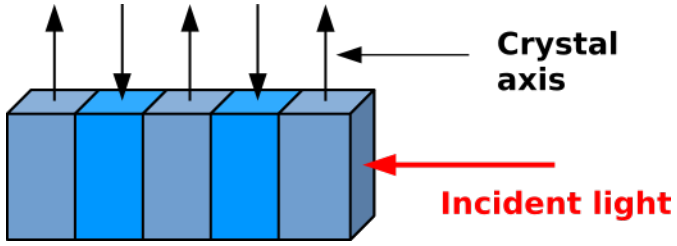

FIGURE 13. Quasi-phase matching by periodic poling in a nonlinear crystal: a process which involves alternating the directional orientation of certain lattice structures via application of strong, local electric fields during manufacture.

The idea is to pole the nonlinear coefficient at a spatial period Λ such that we can compensate for the phase mismatch,

$$k_3 = k_1 + k_2 + \frac{2\pi}{\Lambda}. \tag{3.22}$$

The medium will then act like a Bragg reflector and provide the necessary momentum "kick" for nonlinear frequency conversion to occur.

Pulsed Frequency Conversion

Nonlinear frequency conversion (FC) has been a trending topic for optics research for several decades. Its viability as a quantum state preserving unitary transform was established in the early 90's by Kumar et. al. [62]. Hence, I sometimes refer to it as quantum frequency conversion (QFC). Its applications range from bandwidth compression/expansion to frequency translation into bands that are more convenient for transmission, storage, or detection [63–66]. Figure

14 shows a schematic of a typical TWM-QFC unit. They are marketed either as quasi-phasematched (periodically poled) bulk crystals or waveguides.

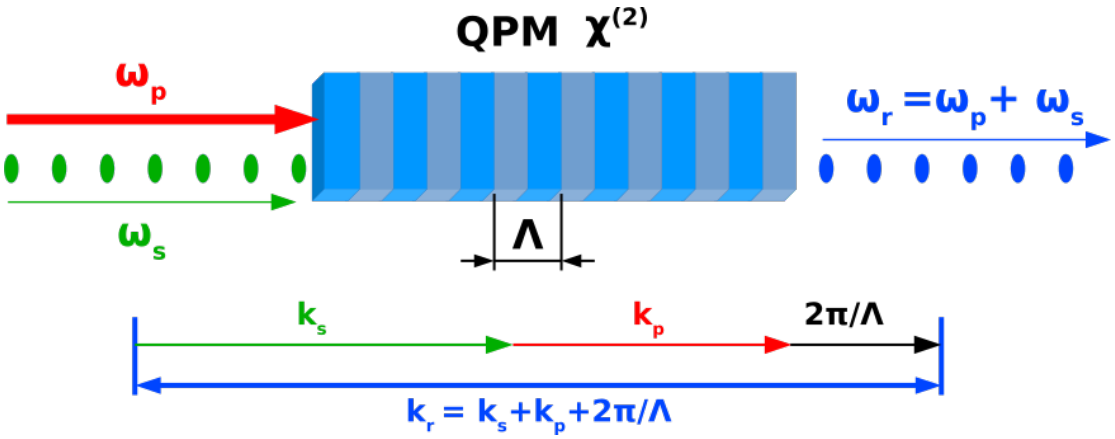

FIGURE 14. Illustration of sum-frequency generation in a quasi-phasematched waveguide. ω_p is the strong laser pump, and ω_s is a weak input signal, which could be single photons, or other quantum states.

When such devices were pumped with pulsed lasers (as opposed to CW laser beams), the conversion efficiency of the process was found to depend not only on the nonlinearity, transverse-mode overlap, laser power, medium length, and such parameters, but also on the temporal mode of the signal field. This prompted the possible use of TWM-QFC as a quantum pulse gate.

For our analysis of TWM, without loss of generalization, I will choose the labels p, s, and r for the pump, signal, and idler frequency bands and denote their central carrier frequencies with ω_p, ω_s, and ω_r respectively. I will assume that the process will occur in a single collinear propagating direction in a single-transverse-mode waveguide geometry, and both energy conservation ($\omega_p+\omega_s = \omega_r$) and phasematching conditions $k_r - k_p - k_s - 2\pi/\Lambda = 0$ are satisfied. Due to the unitarity of the FC process, the same pump can mediate amplitude/energy transfer between the signal-idler pair in either direction. Hence, sum-frequency generation

(SFG) and difference-frequency generation (DFG) are inverse phenomena (Fig. 15).

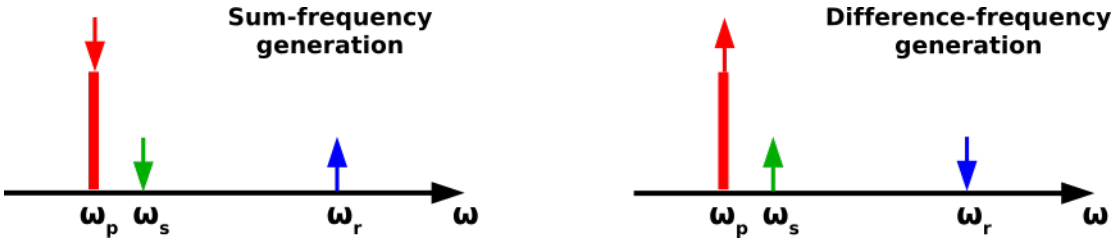

FIGURE 15. Schematic of sum-frequency generation and difference-frequency generation on the frequency axis. The pump field in the p-band is considered strong and nondepleting.

When dealing with pulsed temporal modes (as opposed to CW or quasi-CW modes) with a respectable non-zero bandwidth, we not only need to account for the wave number at the central frequencies in question (as in Eqs. 3.19-3.21), but also the local slope of the dispersion curve. The pulses at the three frequency bands will travel at different group velocities as they overlap and interact with each other. If we were to represent the three fields by the pulse-mode envelope functions $A_j(z,t)$, then the equation of motion would be

$$(\partial_z + \beta_r'\partial_t)\hat{A}_r(z,t) = i\gamma A_p(t-\beta_p' z)\hat{A}_s(z,t), \tag{3.23}$$

$$(\partial_z + \beta_s'\partial_t)\hat{A}_s(z,t) = i\gamma A_p^*(t-\beta_p' z)\hat{A}_r(z,t), \tag{3.24}$$

where $\beta_j' = d\omega/dk|_{\omega_j}$ is the group slowness, or inverse group velocity of the j-band. The pump envelope is considered a classical, nondepleting, square-normalized function $\int_{-\infty}^{\infty} dt|A_p(t)|^2 = 1$. The coupling constant γ includes the nonlinearity coefficient $\chi^{(2)}$, the transverse-mode overlap integrals, as well as the square root of the pump energy.

The symbols $\hat{A}_j(z,t)$ for $j \in \{s,r\}$ have been elevated to photon-annihilation operators (at time t) for their respective bands, but they can also stand for the classical amplitudes of weak-coherent pulses. We must treat this model as a scattering problem, with the FC occurring between $z = 0$ and $z = L$. And Eqs. 3.23 and 3.24 relate the input operators $\hat{A}_j(0,t)$ to the output operators $\hat{A}_j(L,t)$. Equations 3.23-3.24 model not just TWM-QFC but a wide general class of pulse interaction processes.

CHAPTER IV

TEMPORAL-MODE SELECTIVITY

This chapter contains text, equations, and figures from [40–42], and equations from [43]. I am the primary author in [40–42], and was the primary source of the main derivation of the work, and acknowledge the role of my co-authors Dr. Lasse Mejling, Dr. Colin J. McKinstrie, Prof. Karsten Rottwitt, and Prof. Michael G. Raymer in these publications. I also acknowledge Dr. Jesper B. Christensen, the primary author of [43], for his role in deriving Eqs. 4.78-4.80.

The equations of motion for quantum frequency conversion of pulsed modes via three-wave mixing take the form of very general, coupled-mode equations that describe a wide range of systems, including solid-state or atomic-ensemble quantum memories. They apply as long as the interactions are between single transverse modes (perhaps guided modes) and the medium of interaction is uniform. In order to analyze such systems for TM selectivity and related properties, I shall solve them abstractly in various parameter regimes. To recap, the essential nonlinear interaction between temporal modes in two seperate 'signal' and 'idler' bands (designated by the indices s and r) that is mediated by a third control field or pump (index p) is given by

$$(\partial_z + \beta_r' \partial_t) A_r(z,t) = i\gamma A_p(t - \beta_p' z) A_s(z,t), \tag{4.1}$$

$$(\partial_z + \beta_s' \partial_t) A_s(z,t) = i\gamma A_p^*(t - \beta_p' z) A_r(z,t), \tag{4.2}$$

where for $j \in \{s, r, p\}$, β'_j are the group slownesses of pulses (inverse group velocities) in any arbitrary frame, and γ is a measure of the mode-coupling strength, which is a product of the effective nonlinearity coefficient, transverse beam overlaps, and the square root of the pump energy. The functions $\{A_s(z,t), A_r(z,t)\}$ are, as discussed at the end of Chapter III, photon creation operators at time t in their respective bands. But they could equivalently be viewed as classical envelope functions of coherent pulses. The argument z keeps track of the interaction length. The pump amplitude is square-normalized $\left(\int |A_p(t)|^2 dt = 1\right)$. For these spatio-temporal equations to be valid to physical situations, the pump pulse has to be strong enough that it remains unaltered by the interaction. This is generally called the nondepleting pump approximation. This chapter will focus on the abstract model of interacting pulses traveling at different velocities. Note that Eqs. 4.1 and 4.2 can be solved with a frame shift to some arbitrary group velocity. This is accomplished by subtracting all three β'_j by the group-slowness of the frame. It will often be convenient to work in the frame of one of the pulses in question.

Schmidt Modes and Selectivity

I denote the length of our uniform-medium with L, and assume the interaction starts at $z = 0$. The solutions to Eqs. (4.1) and (4.2) can be represented using the Green function (GF) formalism as

$$A_j(L,t) = \sum_{k=r,s} \int_{-\infty}^{\infty} G_{jk}(t,t') A_k(0,t') dt', \tag{4.3}$$

where $A_k(0,t')$ are the input amplitudes and $A_j(L,t)$ are the output amplitudes for $j,k \in \{r,s\}$. The overall GF is unitary, but the block transfer functions ($G_{jk}(...)$) by themselves, are not. We can affect the GF of the process by varying the medium length (L), pump power (γ), pump pulse-shape ($A_p(t)$) and the group-slownesses (inverse group velocities) of the various bands (β_j'). If the GF is 'separable', i.e. $G_{rs}(t,t') \propto \Psi(t)\phi^*(t')$, then with sufficient pump power, an incident s-band signal of temporal shape $\phi(t')$ can be 100% converted into the outgoing r-band packet $\Psi(t)$, and any incoming signal that is orthogonal to $\phi(t')$ will be left unconverted. In general however, the GF is not separable. For time-nonstationary situations, as would be the case for a continuous-wave pump, the GF would be a function of a single variable $(t-t')$. This necessitates the usage of pulsed pumps. The GF formalism is convenient for analysis of temporal-mode selectivity [40, 41], as the separability of the four Green function subkernels can be quantified via their singular-value decomposition [67–70]:

$$\begin{bmatrix} G_{rr}(t,t') & G_{rs}(t,t') \\ G_{sr}(t,t') & G_{ss}(t,t') \end{bmatrix} = \begin{bmatrix} \sum_n \tau_n \Psi_n(t)\psi_n^*(t') & \sum_n \rho_n \Psi_n(t)\phi_n^*(t') \\ -\sum_n \rho_n^* \Phi_n(t)\psi_n^*(t') & \sum_n \tau_n^* \Phi_n(t)\phi_n^*(t') \end{bmatrix}. \tag{4.4}$$

The function sets $\{\psi_n(t')\}, \{\phi_n(t')\}$ are the input "Schmidt modes" and $\{\Psi_n(t)\}, \{\Phi_n(t)\}$ are the corresponding output Schmidt modes for the r and s bands respectively. The sets are, in general, infinite in size. These functions are uniquely determined by the GF, and form orthonormal bases in their relevant bands. The "transmission" and "conversion" Schmidt-coefficients (singular values) $\{\rho_n\}$ and $\{\tau_n\}$ are constrained by $|\tau_n|^2 + |\rho_n|^2 = 1$ to preserve unitarity.

It is convenient to choose the mode index 'n' in decreasing order of Schmidt-mode conversion efficiency (CE), so that $|\rho_1|^2 \geq |\rho_2|^2 \geq |\rho_3|^2$... and so on. An FC device with perfect mode discrimination would have a non-zero ρ_1, and $\rho_{n>1} = 0$, meaning the GF subkernel is separable but not necessarily 100% efficient. A device with perfect mode *selectivity* would have $\rho_j = \delta_{j,1}$ (i.e., the process performs full frequency conversion on one particular input mode and transmits all power from any orthogonal mode in the same input band). We can quantify the add/drop quality of the GF using the ordered-set of conversion efficiencies to define an add/drop 'selectivity' (first introduced in [40]):

$$S = \frac{|\rho_1|^4}{\sum_{n=1}^{\infty} |\rho_n|^2} \leq 1. \tag{4.5}$$

I call the factor $|\rho_1|^2/(\sum_{n=1}^{\infty} |\rho_n|^2)$ the 'separability', and the additional multiplier ($|\rho_1|^2$) is the CE of the dominant temporal mode. The selectivity characterizes both the degree of separability of the GF and the process efficiency. High separability is easier to achieve at the expense of reduced CE for the target TM [71, 72]. Selectivity serves as a single scalar figure of merit for both high separability and high CE. The equality in Eq. (4.5) holds for a perfect QPG. The unitary nature of the transformation imposes a pairing between the Schmidt modes across the r and s bands [67, 73].

The effect of FC on an arbitrary input temporal mode can be easily computed by expressing said input state in the natural input Schmidt-mode basis of the device and employing the Schmidt-coefficient beam-splitter relations. The remarkable aspect of the beam-splitter-like transformation is that, when working with the natural Schmidt modes defined by the process, only the modes of the

same Schmidt index n interact. The temporal Schmidt modes of different n are transparent to one another. (The challenge in the experiment is to shape the TMs of the signal pulses being used to match the natural Schmidt modes of the process, which are in turn defined by the pump shape and properties of the medium.)

To illustrate in detail, consider arbitrary input and output fields expressed as discrete sums over corresponding Schmidt modes,

$$A_r(0,t) = A_r(t)|_{\text{in}} = \sum_n a_n \psi_n(t), \quad A_r(L,t) = A_r(t)|_{\text{out}} = \sum_n c_n \Psi_n(t), \tag{4.6}$$

$$A_s(0,t) = A_s(t)|_{\text{in}} = \sum_n b_n \phi_n(t), \quad A_s(L,t) = A_s(t)|_{\text{out}} = \sum_n d_n \Phi_n(t). \tag{4.7}$$

The coefficients $\{a_n, b_n, c_n, d_n\}$ are pairwise related via a unitary beam-splitter-like transformation [67], which, if we assume real τ_n and ρ_n, are expressed as

$$c_n = \tau_n a_n + \rho_n b_n, \tag{4.8}$$

$$d_n = \tau_n b_n - \rho_n a_n, \tag{4.9}$$

where the n^{th}-Schmidt mode CE ($|\rho_n|^2 = 1 - |\tau_n|^2$) is analogous to "reflectance". All time-domain functions described thus far have corresponding frequency-domain analogs. The form of the GF in frequency domain can also provide meaningful insights. If we define functions $\widetilde{\Psi}_n(\omega)$ and $\widetilde{\phi}_n(\omega)$ as the Fourier-transforms of the corresponding time-domain Schmidt modes $\Psi_n(t)$ and $\phi_n(t)$, then

$$\widetilde{G}_{rs}(\omega,\omega') = \int dt \int dt' \exp[i\omega t] G_{rs}(t,t') \exp[-i\omega' t'] = \sum_n \rho_n \widetilde{\Psi}_n(\omega) \widetilde{\phi}_n^*(\omega'). \tag{4.10}$$

The above analysis has been shown [67, 68] to apply equally well to quantum wave-packet states as to classical fields, for the simple reason that all the relations are linear in the mode creation and annihilation operators. Thus the GFs found here can model experiments on frequency conversion (FC) of single-photon wave-packet states [74–76] or FC of other quantum states such as squeezed states containing multiple photons.

Low-Conversion Limit and Green Functions

We are attempting to model a coupling between three separate pulses, each of which is convecting through our medium at a different speed. Even with the simplification of the nondepleting pump approximation, closed-form expressions of the Green functions for all possible parameter sets or regimes are not known to exist.

We can develop an important guide to the different regimes of TWM by solving the problem perturbatively for small interaction strengths (γ) for arbitrary group slownesses and pulse shapes (following the discussion in [77]). I define the coupling coefficient as $\kappa(z,t) = \gamma A_p(t - \beta_p' z)$. For this calculation, we could allow the nonlinearity $\gamma(z)$ to be position dependent, which can be used as a design feature if desired [30, 78], but for simplicity I continue to assume that the medium is uniform. By integrating Eqs. (4.1) and (4.2) with respect to z, we get the exact relations:

$$A_r(L,t) = A_r(0, t - \beta_r' L) + i \int_0^L dz' \kappa(z', t_r') A_s(z', t_r'), \tag{4.11}$$

$$A_s(L,t) = A_s(0, t - \beta_s' L) + i \int_0^L dz' \kappa^*(z', t_s') A_r(z', t_s'). \tag{4.12}$$

where $t'_r := t - \beta'_r(L - z')$ and $t'_s := t - \beta'_s(L - z')$. Treating the coupling as a perturbation, we get

$$A_r(L,t) \approx A_r(0,t_r) + i \int_0^L dz' \kappa(z', t'_r) A_s(0, t_r + \beta'_{rs} z'), \tag{4.13}$$

$$A_s(L,t) \approx A_s(0,t_s) + i \int_0^L dz' \kappa^*(z', t'_s) A_r(0, t_s - \beta'_{rs} z'). \tag{4.14}$$

where $t_r = t - \beta'_r L$, $t_s = t - \beta'_s L$. The $\approx$ symbols indicate that perturbative approximations render Eqs. (4.13) and (4.14) weakly non-unitary. By defining $t' = t - \beta'_r L + \beta'_{rs} z'$, where $\beta'_{rs} = \beta'_r - \beta'_s$ is the difference in slownesses, one can change the integration variable to time, and rewrite Eqs. (4.13) and (4.14) using the approximate Green function $\overline{G}_{jk}(t,t')$ in the low-conversion limit [77]:

$$A_j(L,t) \approx A_j(0,t_j) + \int_{-\infty}^{\infty} dt' \overline{G}_{jk}(t,t') A_k(0,t') \Big|_{k \neq j}, \tag{4.15}$$

$$\overline{G}_{rs}(t,t') = i \frac{\gamma}{\beta'_{rs}} A_p \left(\frac{\beta'_{rp} t' - \beta'_{sp}(t - \beta'_r L)}{\beta'_{rs}} \right) H(t' - t + \beta'_r L) H(t - t' - \beta'_s L), \tag{4.16}$$

$$\overline{G}_{sr}(t,t') = -i \frac{\gamma^*}{\beta'_{rs}} A^*_p \left(\frac{\beta'_{rp}(t - \beta'_s L) - \beta'_{sp} t'}{\beta'_{rs}} \right) H(t' - t + \beta'_s L) H(t - t' - \beta'_r L), \tag{4.17}$$

where $t_j = t - \beta'_j L$, $\beta'_{jp} = \beta'_j - \beta'_p; \forall j \in \{r, s\}$, and $H(x)$ is the Heaviside step-function.

Eqs. (4.16) and (4.17) provide a simple way to understand the FC process for arbitrary relations between group slownesses. A first observation is that the

Heaviside step-functions represent that because the medium length is finite, the time of interaction is restricted to the t' interval $t' \in (t-\beta'_r L, t-\beta'_s L)$. In the (t,t') domain, this interval corresponds to a 45°-tilted band with width $\beta'_{rs}L$. Therefore, if the goal is to have the GF separable in t and t', the shape of this interval poses a challenge. Whatever the pulse shape of the pump, the low-conversion Green function is proportional to a scaled version of that shape. Note that if ($\beta'_{rp} = 0$ or $\beta'_{sp} = 0$), then the factor $A_p(...)$ in Eqs. (4.16) and (4.17) depends only on t (or t'), making that factor in the GF separable. Further insight is obtained by plotting the GF, as in Fig. 16, for the case of a (normalized) Gaussian pump pulse $A_p(t) = \left(\tau_p^2\pi\right)^{-1/4} \exp[(-t^2/(2\tau_p^2)]$ with duration τ_p.

For the four GF's plotted in Fig. 16, the computed CE's for the first four temporal modes are listed in Table 1, where $\overline{\gamma} = \gamma/\beta'_{rs}$ is of order 0.01. The corresponding selectivities are: $S =$ **(a)** $0.646\overline{\gamma}^2$, **(b)** $0.676\overline{\gamma}^2$, **(c)** $0.646\overline{\gamma}^2$, **(d)** $0.610\overline{\gamma}^2$. The Schmidt coefficients were numerically computed by performing a singular value decomposition (SVD) of the GF in Eq. (4.16).

TABLE 1. Conversion efficiencies for the first four dominant Schmidt modes for the Green functions from Fig. 16. $\overline{\gamma} = \gamma/\beta'_{rs}$.

(a)	$1.0\overline{\gamma}^2$	$0.306\overline{\gamma}^2$	$0.088\overline{\gamma}^2$	$0.037\overline{\gamma}^2$
(b)	$1.0\overline{\gamma}^2$	$0.275\overline{\gamma}^2$	$0.064\overline{\gamma}^2$	$0.033\overline{\gamma}^2$
(c)	$1.0\overline{\gamma}^2$	$0.306\overline{\gamma}^2$	$0.088\overline{\gamma}^2$	$0.037\overline{\gamma}^2$
(d)	$1.0\overline{\gamma}^2$	$0.342\overline{\gamma}^2$	$0.115\overline{\gamma}^2$	$0.047\overline{\gamma}^2$

The slope of the line along the highest part of the band (lightest color) is given by

$$\text{slope} = \frac{dt'}{dt}\bigg|_{\max} = \frac{\beta'_s - \beta'_p}{\beta'_r - \beta'_p}. \tag{4.18}$$

In an attempt to create an approximately separable GF, one can choose parameters as in Fig. 17. The computed CE's for the first four temporal modes in

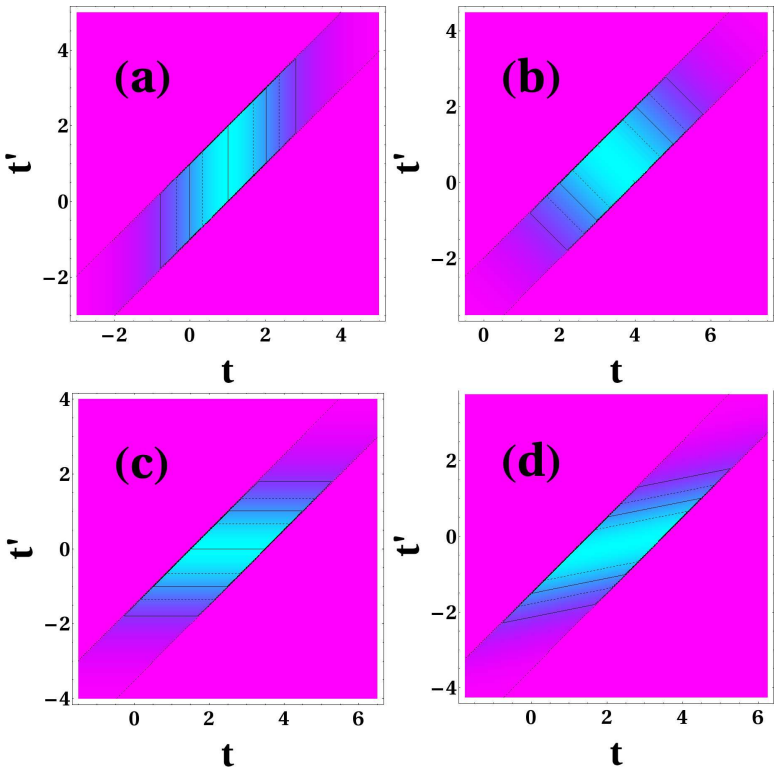

FIGURE 16. Green function $\overline{G}_{rs}(t,t')$ in low-conversion limit for medium length $L = 1$, and Gaussian pump duration $\tau_p = 1$. **(a)** $\beta'_r/\beta'_p = 1$, $\beta'_s/\beta'_p = -1$, **(b)** $\beta'_r/\beta'_p = 4/3$, $\beta'_s/\beta'_p = 2/3$, **(c)** $\beta'_r/\beta'_p = 3.5/1.5$, $\beta'_s/\beta'_p = 1$, **(d)** $\beta'_r/\beta'_p = 3.5$, $\beta'_s/\beta'_p = 1.5$. All times in units of τ_p. Reproduced from [40].

this case are $\{1.0\overline{\gamma}^2, 0.029\overline{\gamma}^2, 0.028\overline{\gamma}^2, 0.011\overline{\gamma}^2\}$, where $\overline{\gamma} = \gamma/\beta'_{rs}$ is of order 0.01. The selectivity is $S = 0.913\overline{\gamma}^2$. While the separability is high, the CE of the first Schmidt mode is of the order of $\overline{\gamma}^2$.

Improved selectivity can be achieved using the strategy proposed in [29], where one of the signals is matched in slowness to the pump, as in Fig. 16(a), and the pump pulse is made very short. The short pump width helps counter the ill effects of the 45°-sloping step-functions on GF separability by selecting a narrow vertical or horizontal region in (t,t') space. These choices give the GF's (in the low-CE limit) in Fig. 18.

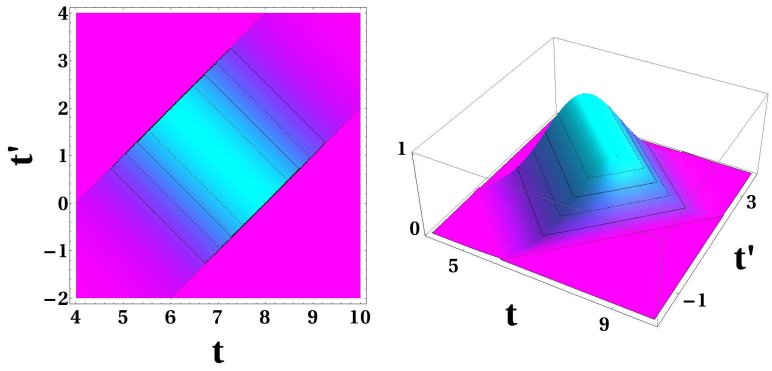

FIGURE 17. Low-conversion Green function for $\beta'_r = 8$, $\beta'_s = 4$, $\beta;_p = 6$, $\tau_p = 0.707$, $L = 1$. Top view and perspective view. Reproduced from [40].

The numerically computed CE's for the first four temporal modes in Fig. 18(a) are $\{1.0\overline{\gamma}^2, 0.022\overline{\gamma}^2, 0.006\overline{\gamma}^2, 0.003\overline{\gamma}^2\}$, and the selectivity is $S = 0.967\overline{\gamma}^2$. In Fig. 18(b) the CE's and the selectivities are identical to case in Fig. 18(a). $\overline{\gamma}$ is of order 0.01.

The temporal Schmidt modes for the case in Fig. 18(b) are shown in Fig. 19. It is seen that the input modes mimic the projection of the GF onto the t'-axis, while the output modes mimic the projection onto the t-axis. If the input field occupies only the dominant ($j = 1$) Gaussian-like mode, then it is frequency converted with efficiency $|\rho_1|^2 \approx \overline{\gamma}^2$ and generates an output pulse that is much longer and rectangular in shape. Such pulse shaping may or may not be desirable, depending on the application.

The s-output modes for case 18(a) and the r-output modes for case 18(b) will have temporal width $\beta'_{rs}L$, which is the maximum duration of interaction within the medium. Since the pump copropagates with a matched slowness with one of the input bands, and the CE is low enough to prevent input-band depletion, FC occurs throughout the traversed medium length, stretching the generated output mode in the other band due to difference in slownesses (β'_{rs}).

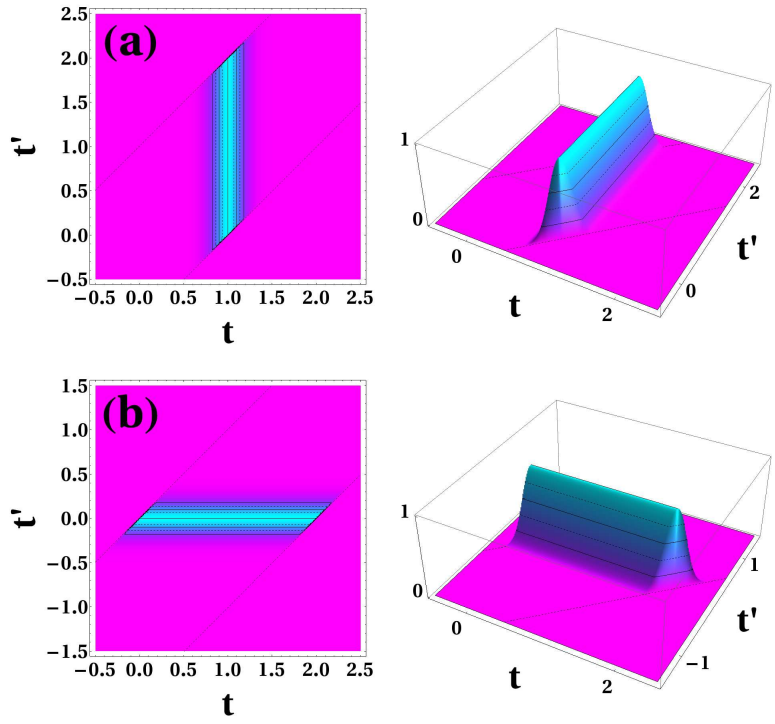

FIGURE 18. Low converison Green function for **(a)** $\beta'_r = \beta'_p = 1$, $\beta'_s = -1$, $\tau_p = 0.1$, $L = 1$. For **(b)** $\beta'_r = 2$, $\beta'_s = \beta'_p = 0$, $\tau_p = 0.1$, $L = 1$. Reproduced from [40].

To demonstrate the ability to choose which temporal mode is selected for FC, Fig. 20 shows the results for a pump pulse with the shape proportional to a first-order Hermite-Gaussian function $HG_1(x) \propto x \exp[-x^2/2]$, which has a zero-crossing at its "midpoint". The efficiencies are $\{1.0\overline{\gamma}^2, 0.049\overline{\gamma}^2, 0.007\overline{\gamma}^2, 0.005\overline{\gamma}^2\}$ and the selectivity is $S = 0.936\overline{\gamma}^2$, where $\overline{\gamma} = \gamma/\beta'_{rs}$ is of order 0.01. The dominant mode has a shape similar to the pump pulse.

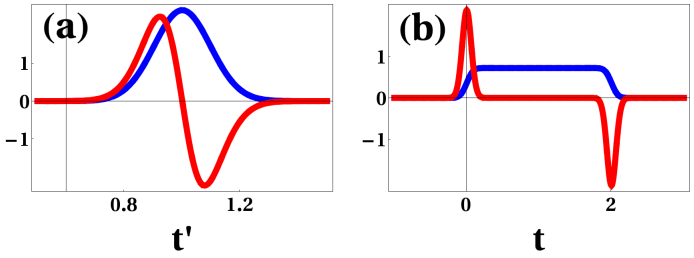

FIGURE 19. Temporal Schmidt modes for the case in Fig. 18(b) $\beta'_r = \beta'_p = 1$, $\beta'_s = -1$, $\tau_p = 0.1$, $L = 1$. **(a)** First two input modes. **(b)** Corresponding output modes. First modes are in blue. Second modes are in red. Reproduced from [40].

Alternatively, the preceding analysis can be carried out in the frequency-domain, where the GF takes the form:

$$\widetilde{\overline{G}}_{rs}(\omega,\omega') = i\frac{\gamma}{\beta'_{rs}}\widetilde{A}_p(0,\omega-\omega')\exp[-iL\beta'_r(\omega-\omega')\beta'_{sp}/\beta'_{rs}]$$
$$\times \frac{\sin(\overline{\omega}'\beta'_{rs}L)}{\overline{\omega}'}\exp[iL\overline{\omega}'(\beta'_r+\beta'_s)] \tag{4.19}$$
$$= g_1(\omega-\omega')\times g_2(\overline{\omega}'), \tag{4.20}$$

where $\overline{\omega}' = (\beta'_{rp}\omega - \beta'_{sp}\omega')/(2\beta'_{rs})$. Varying the pump duration τ_p changes the bandwidth of factor $g_1(\omega-\omega')$, and the choice of slowness (β'_j) and medium length (L) affects the slope and the phase-matching bandwidth of factor $g_2(\overline{\omega}')$ in (ω,ω') space. The separability of $\overline{G}_{rs}(t,t')$ is also evident in (ω,ω')-space. As pointed out in [67], for the case in Fig. 18(a) with $\beta'_{rp} = 0$, $g_2(\overline{\omega}')$ would be a sinc-function parallel to the ω-axis with a phase-matching bandwidth proportional to $1/(\beta'_{sp}L)$ (a measure of the vertical separation between the edges of the Heaviside-step functions in Fig. 18(a)), and the shortness of the pump will cause $g_1(\omega-\omega')$ to have a wider bandwidth, intersecting $g_2(\overline{\omega}')$ at a 45° inclination. Alternatively, one could choose parameters such that $\beta'_{sp} = -\beta'_{rp}$, giving $g_2(\overline{\omega}')$ a −45° inclination. In the frequency domain, if the pump bandwidth and medium length are optimized,

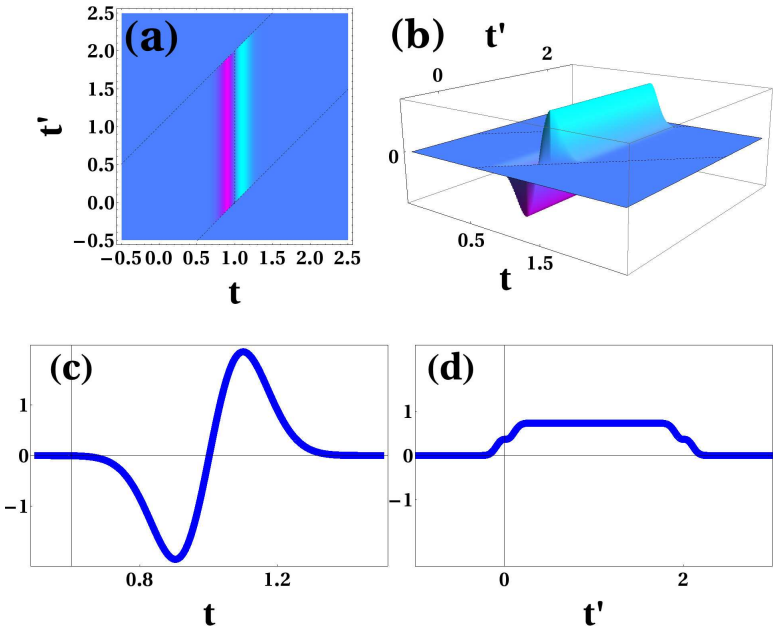

FIGURE 20. **(a), (b)** Low-conversion Green function with higher-order pump pulse and $\beta_r' = \beta_p' = 1$, $\beta_s' = -1$, $\tau_p = 0.1$, $L = 1$. **(c)** Dominant input Schmidt mode. **(d)** Dominant output Schmidt mode. Reproduced from [40].

we can reproduce a roughly separable GF as in Fig. 17, with (t, t') replaced by (ω, ω'). GF separability suffers in this regime if the pump bandwidth is made much larger than the phase-matching bandwidth.

To summarize, in the low CE limit, we are able to achieve high temporal mode separability when the GF is nearly separable (Fig. 18) and moderate separability when the GF has a modicum of symmetry (Fig. 17). But the low CE diminishes the selectivity. I next address whether high selectivity can also be found in cases with higher conversion efficiencies.

Numerical Simulation Method

As mentioned above, no closed-form expressions exist for the GF for general values of parameters. In order to derive the numerical GF for TWM, I first implemented a coupled mode equation solver [68, 79] that accepts arbitrary input

functions ($A_r(0,t')$, $A_s(0,t')$) as arguments, and computes the resultant output functions ($A_r(L,t)$, $A_s(L,t)$) for Eqs. (4.1) and (4.2). This is achieved using a Runge-Kutta based method. The solver iterates over differential steps in pulse-propagation (Δz) from $z = 0$ to L (medium length). Every iteration consists of an upwinded z-propagation scheme for all three pulses (signal, pump and idler) by a step (Δz), followed by a fourth-order Runge-Kutta implementation of the coupled nonlinear interaction, all in space-time domain. Next, I determine the GF by computing the outputs for an orthogonal set of input 'test signals'. To ellaborate, consider the GF submatrix and its singular-value-decomposition (SVD):

$$G_{rs}(t,t') = \sum_j \rho_j \Psi_j(t) \phi_j^*(t'). \tag{4.21}$$

The objective is to calculate all the individual components (ρ_j, $\Psi_j(t)$, $\phi_j(t')$) on the right-hand-side. I first pick two arbitrary spanning-sets of basis functions $\{B_{r,k}\}$ and $\{B_{s,l}\}$ and re-express the Schmidt modes as:

$$\Psi_j(t) = \sum_k U_{jk} B_{r,k}(t); \quad \phi_j^*(t') = \sum_l V_{jl} B_{s,l}^*(t'), \tag{4.22}$$

$$G_{rs}(t,t') = \sum_{k,l} \left[\sum_j U_{jk} \rho_j V_{jl} \right] B_{r,k}(t) B_{s,l}^*(t') = \sum_{k,l} \left[\overline{G}_{rs} \right]_{kl} B_{r,k}(t) B_{s,l}^*(t'). \tag{4.23}$$

Using ($A_r(0,t) = 0$, $A_s(0,t') = B_{s,l}(t')$) as inputs for the solver, and decomposing the resulting r-band outputs $A_r(L,t)$ in the $\{B_{r,k}\}$ basis will yield the entire l^{th}-column of the complex matrix $\overline{G}_{rs}$. Once this matrix is determined, its SVD will directly reveal $\{U_{jk}\}$, $\{V_{jl}\}$, and $\{\rho_j\}$, and through them, the Schmidt modes. For the results presented in this chapter, I chose Hermite-Gaussian functions for the

spanning-set of basis functions for both input and output Schmidt modes, since the low-CE Schmidt modes for Gaussian pump shapes are nearly Hermite-Gaussian.

Since the computation of the GF involved repeated execution of the same solver for the same set of system parameters and iteration numbers with only a change in the inputs, this task was parallelized for rapid execution. This was achieved through the utilization of multiple CPU nodes and cores on the ACISS computing cluster at the University of Oregon. Several slave nodes would run a device simulator that would accept input fields from a master node, and return the corresponding output fields after simulation. The master node would assign free/available slave nodes different input field functions necessary for computation of the GF. The slave code was written in FORTRAN programming language, whereas the master code was written in MATLAB. The message passing between the master and slave nodes was handled through openMPI libraries on the slave side, and a proprietary "parallel-gateway" library developed by Craig Rasmussen at the University of Oregon.

Regimes and Selectivity Barrier

Assuming energy conservation and perfect phase-matching for the band carrier frequencies, the choice of waveguide/material dispersion is reflected in our equations via the relative magnitudes of the band group slownesses. I classify the different regimes of operation as follows:

- **Single-sideband, group-velocity matched**

  GVM: $\beta'_s = \beta'_p \neq \beta'_r$ or $\beta'_r = \beta'_p \neq \beta'_s$

- **Symmetrically counter-propagating**

  SCuP: $\beta'_{rp} = -\beta'_{sp}$

– **Counter-propagating signals**

  CuP: $\beta'_{sp}\beta'_{rp} < 0, \quad \beta'_s \neq \beta'_r$

– **Co-propagating signals**

  CoP: $\beta'_{sp}\beta'_{rp} > 0, \quad \beta'_s \neq \beta'_r$

– **Exactly co-propagating**

  ECoP: $\beta'_r = \beta'_s$

In this section, I employ numerical techniques similar to those used in [68] to construct the GF for any given set of pump parameters. To accomplish this I numerically propagate a large number of 'test signals' through the medium (chosen to be members of a complete, orthonormal set of Hermite-Gaussian functions of appropriate temporal width) to find the effects of the process on an arbitrary input. This method enables a comprehensive study of TWM, even for cases for which analytical solutions are not known.

I first present numerical results for the GVM regime, which has been favored by C. Silberhorn's group [30], and has yielded the best results in terms of selectivity [44, 71, 72, 80].

($\beta'_{sp} = 0, \beta'_{rs} \neq 0$) Single-sideband, group-velocity matched regime

The function of an effective QPG is to efficiently discriminate between orthogonal temporal modes. Since any band input enters and traverses through the waveguide in causal sequence (linearly with the pulse function argument), to achieve discrimination the pump pulse must overlap with all segments (temporal slices) of the input pulse for a non-zero amount of time within the waveguide. This ensures that: (a) all the power distributed among all the segments of the

first input Schmidt mode has a chance of interacting with the pump and being FC'd into the other band, and (b) the device "measures" the entire shape of the temporal input mode, which is essential for discriminating between different temporal mode shapes.

Two orthogonal temporal modes (say in band r) can have locally similar shapes in certain segments. When these segments overlap with the pump pulse within the nonlinear medium, the only way for the device to react to them differently is for the local instantaneous mode features in band s to differ [Eq. (4.1)], which is determined by all the wave-mixing that has occurred until that time instant. Both of these intuitive requirements are satisfied if one of the band slownesses is matched to the pump slowness (single sideband group-velocity matched or GVM), and the temporal pump width is much shorter than the interaction time $\beta'_{rs}L$. The preceding low CE-limit analysis has already deemed this regime favorable for separability, and other groups have predicted [29] and demonstrated [72, 80] significant success at higher CE's as well. I now present the numerical results for the same. I present the complete, exact analytical solution for the GVM case at the end of this section.

In the GVM regime, for a given pump shape, the selectivity is influenced most by the GF aspect ratio ($\tau_p/(\beta'_{rs}L)$) and effective interaction strength ($\overline{\gamma} = \gamma/\beta'_{rs}$). In Fig. 21, I plot the numerically determined CE for the first five Schmidt modes for various $\overline{\gamma}$ for a Gaussian pump-pulse with parameters from Fig. 18(b) ($\beta'_r = 2$, $\beta'_s = \beta'_p = 0$, $\tau_p = 0.1$, $L = 1$). The selectivity values are listed in the inset. A maximum selectivity of 0.81 is found for $\overline{\gamma} = 1.0$.

Although the GF displays good mode-separability at low-CE's, the selectivity is unable to maintain high values beyond a certain $\overline{\gamma}$. Figure 22 shows the first

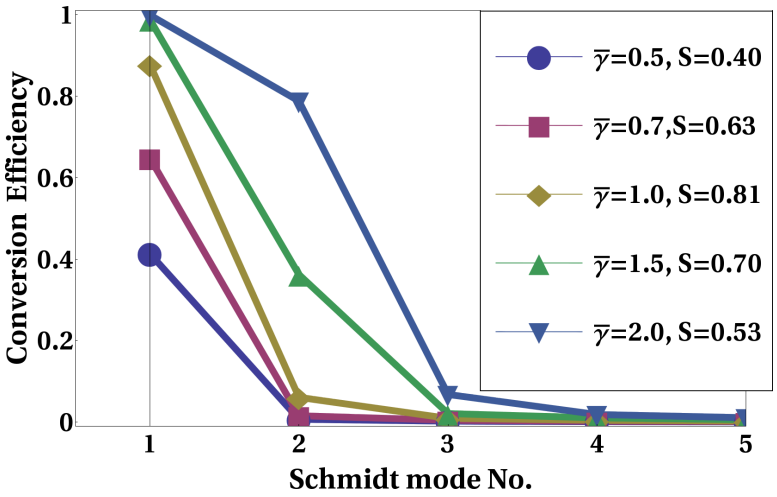

FIGURE 21. Numerically determined conversion efficiencies of the first five Schmidt modes for the GVM case in Fig. 18(b) for various $\overline{\gamma}$. The resulting selectivities S is given in the legend. Reproduced from [40].

three input and output Schmidt modes for $G_{rs}(t,t')$ for the same case. Figure 23 shows the first Schmidt modes from both bands for increasing $\overline{\gamma}$. Note the strong shape distortion relative to the low-CE case, reflecting the change in the GF shape with increasing $\overline{\gamma}$. This illustrates the limits of validity of the approximation used in [29].

Shortening the pump width by a factor of 10 minutely improves the selectivity, while lengthening pump width causes it to decrease. I present the analytical solution for this GVM regime at the end of this section, where I show that this case leads to the highest selectivity of all the regimes treated in this study.

($\beta'_{rp} = -\beta'_{sp}$) Symmetrically counter-propagating signals regime, shape preserving frequency conversion

I now treat the SCuP regime, in which the signals propagate in opposite directions in the pump frame with the same slowness relative to the pump pulse. Specifically, for this subsection I work with parameter values: $\beta'_s = 0$, $\beta'_p = 2$,

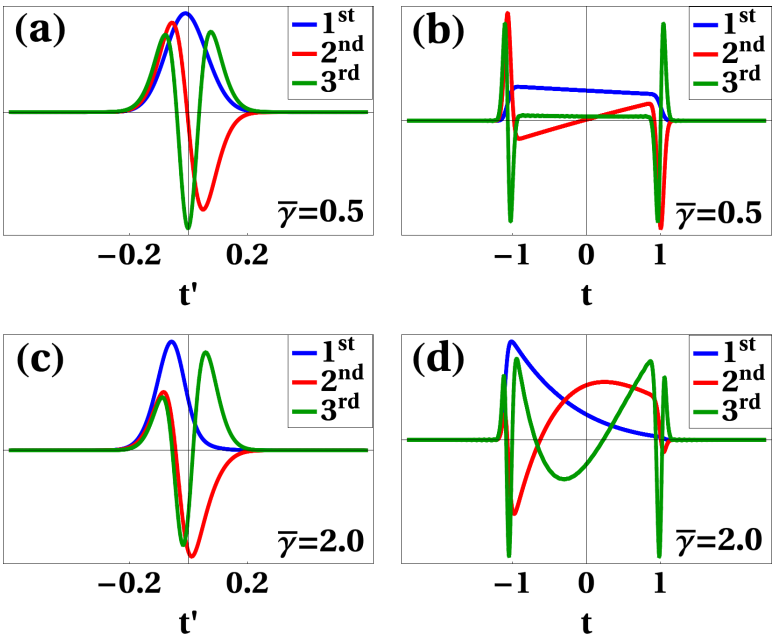

FIGURE 22. The first three s input (a, c) and r output (b, d) Schmidt modes for $\overline{\gamma} = 0.5$(a, b), 2.0(c, d), for parameters from Fig. 18(b). Numerical results. Reproduced from [40].

$\beta'_r = 4$, $L = 1$, and Gaussian-shaped pump. For pump width $\tau_p = 0.707$, the low-CE Green function matches a time-shifted version of the plot in Fig. 17. Increasing $\overline{\gamma}$ to higher-CE will cause the selectivity S to rise to a maximum, and then fall back to lower values, just like in the GVM regime, Fig. 24 plots selectivity vs. $\overline{\gamma}$ for various pump widths.

I sought to improve this result by varying the low-CE GF aspect ratio $(\tau_p/(\beta'_{rs}L))$ by changing τ_p. Starting from narrow pumps and increasing the width, I could optimize the selectivity-maxima to about $S \approx 0.7$ for a Gaussian pump width of $\tau_p \approx 1.5$ and $\overline{\gamma} \approx 0.75$. Further increasing τ_p stretched the GF shape in the $t = t'$ direction, reducing its separability/selectivity-maximum, as shown in Fig. 24. The selectivity maximum moves to larger $\overline{\gamma}$ for increasing τ_p because longer pump durations correspond to smaller peak intensity.

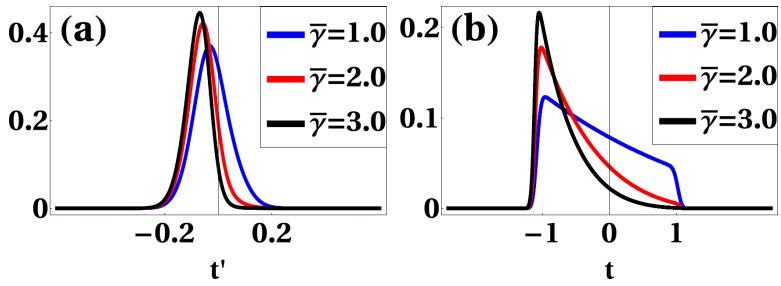

FIGURE 23. Distortion of the first Schmidt modes (r input (a) and s output (b)) with increasing $\overline{\gamma}$, for parameters from Fig. 18(b). Numerical results. Reproduced from [40].

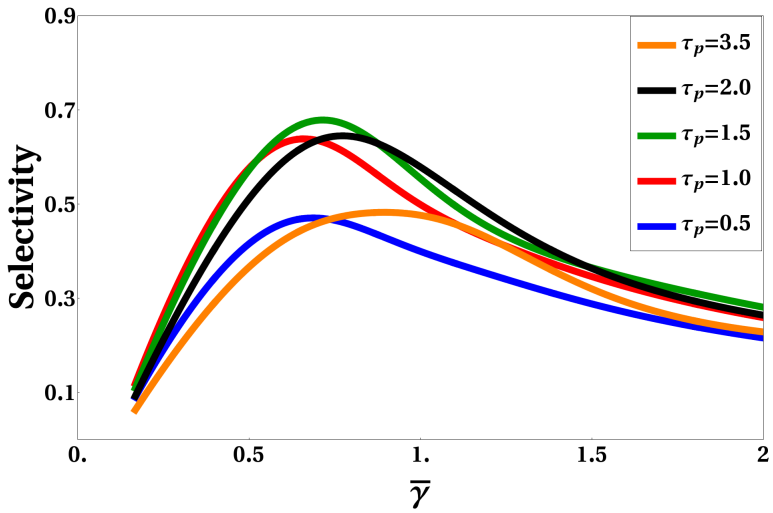

FIGURE 24. Selectivity vs. $\overline{\gamma}$ for Gaussian pumps of various widths. $\beta_s' = 0$, $\beta_p' = 2$, $\beta_r' = 4$, $L = 1$. Numerical results. Reproduced from [40].

Figure 25 shows how the CEs for the first ten Schmidt modes change with $\overline{\gamma}$ for various τ_p. For large $\overline{\gamma}$, higher-order CEs tend to decrease with increasing τ_p, suggesting mildly improved selectivity. They also appear to oscillate about a decreasing central value in a damped fashion with increasing τ_p. For the values plotted, this is most pronounced in the CE of the third Schmidt mode for $\overline{\gamma} = 1.18$.

In this SCuP regime I found that the shapes of the output (r) Schmidt modes are essentially identical to those of the input (s) Schmidt modes. Figure 26 shows the dominant s input and r output Schmidt modes at $\overline{\gamma} = 3.36$, for select τ_p. This

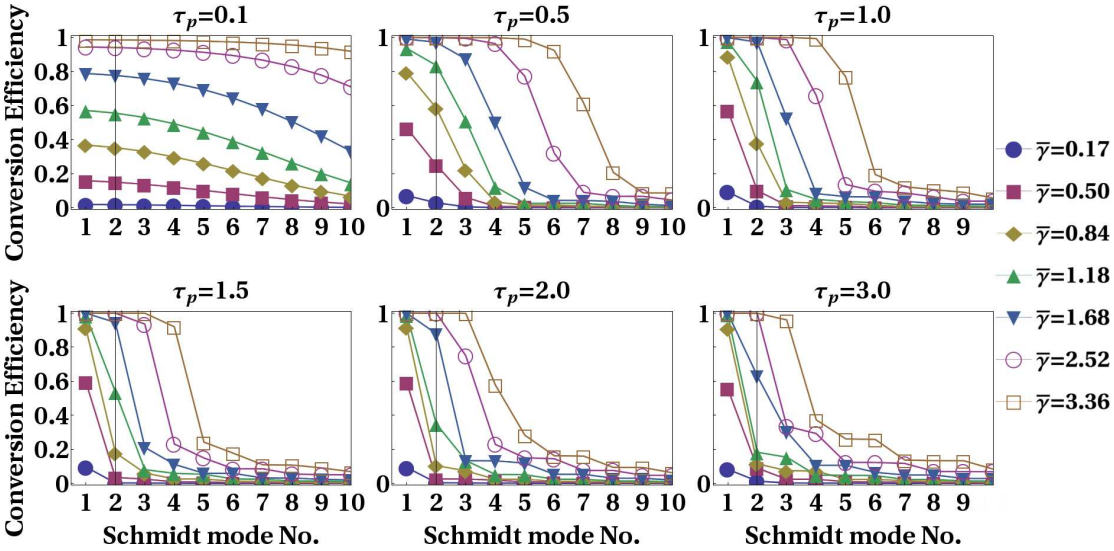

FIGURE 25. Conversion efficiencies for the first ten Schmidt modes for various $\overline{\gamma}$ and Gaussian pump widths (τ_p). $\beta'_s = 0$, $\beta'_p = 2$, $\beta'_r = 4$, $L = 1$. Numerical results. Reproduced from [40].

shape-preserving behavior is related to the GF consisting of the pump shape as a factor sloping parallel to the $t = -t'$ direction, and is independent of $\overline{\gamma}$ for the values tested. The individual Schmidt mode shapes, however, do change with $\overline{\gamma}$. For $\tau_p \gg 0.1$, the Schmidt mode widths scale linearly with the pump width.

The time-widths of the Schmidt modes have a lower bound of $\beta'_{rs}L/2$ due to the Heaviside step-function boundaries. Decreasing τ_p to small values relative to $\beta'_{rs}L$ (e.g., 0.1) causes the convergence of Schmidt mode shapes to those plotted in Fig. 51(a,b). The dominant CE's for the short-pump case nearly match each other in values, especially for very low and very high $\overline{\gamma}$, making for a non-selective add/drop device. These features cause the short-pump SCuP regime to preserve the shapes of a large family of input pulses during FC (even for CE's approaching unity). For example, for the $\tau_p = 0.1, \overline{\gamma} = 3.36$ case in Fig. 25, all the first seven Schmidt modes have near unity CE's. So any input pulse that can be completely constructed by a linear superposition of the first seven input Schmidt modes will

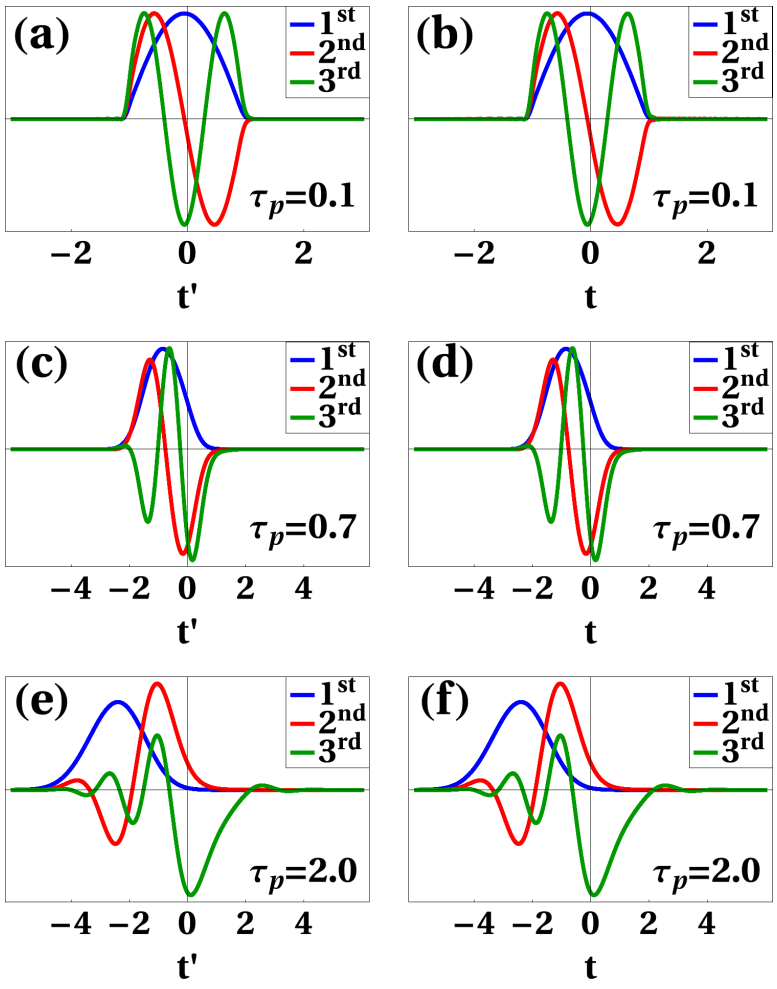

FIGURE 26. The first three s input (a,c,e) and r output (b,d,f) Schmidt modes for $\overline{\gamma} = 3.36$, and $\tau_p = 0.1$(a,b), 0.7(c,d), and 2.0(e,f). $\beta_s' = 0$, $\beta_p' = 2$, $\beta_r' = 4$, $L = 1$. Numerical results. Reproduced from [40].

FC into the other band into the exact same superposition of the first seven output Schmidt modes, which also match the corresponding input Schmidt mode shapes (Fig. 26). I hypothesize that this results from the $t' = -t$ direction of the GF being more pronounced for shorter τ_p (Fig. 27), which maps local time-slices/segments of the input and output pulses in a one-to-one fashion.

Note that the pump in the GF is constant along the $-45°$ direction. So the interaction of each time segment of the signal with the corresponding segment in

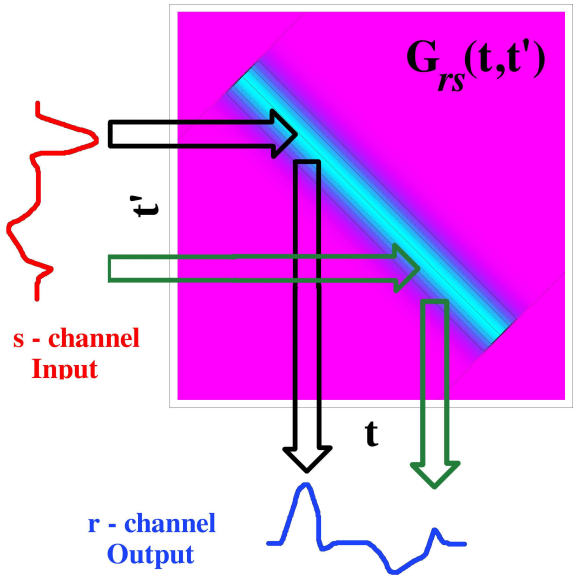

FIGURE 27. Proposed mechanism for shape-preserving frequency conversion in the short-pump "symmetrically counter-propagating signals" regime. Reproduced from [40].

the idler is driven by the same pump profile. The resolution of such one-to-one segment mappings is determined by the pump width. For broad pumps, any given time segment of the signal would then influence a larger portion of the idler pulse, and vice versa. The inability of the global shape of an input pulse to influence its CE results in a poor QPG, but this feature, which we call shape-preserving FC, has potential applications in multi-color quantum interference [67, 81, 82].

($\beta'_{rp}\beta'_{sp} < 0$) counter-propagating signals regime

The previous subsection dealt with the parameter set $\beta'_s = 0$, $\beta'_r = 4$, $\beta'_p = 2$. Holding the β'_s and β'_r slownesses at these values, I now vary the pump slowness (β'_p) within the range $[0, 4]$ and chart the properties of the GF. At values 0 and 4, the results matched those of the GVM regime. The range $\beta'_p \in [0, 2]$ showed a one-to-one symmetrically-mapped correspondence with the range $[2, 4]$. That is,

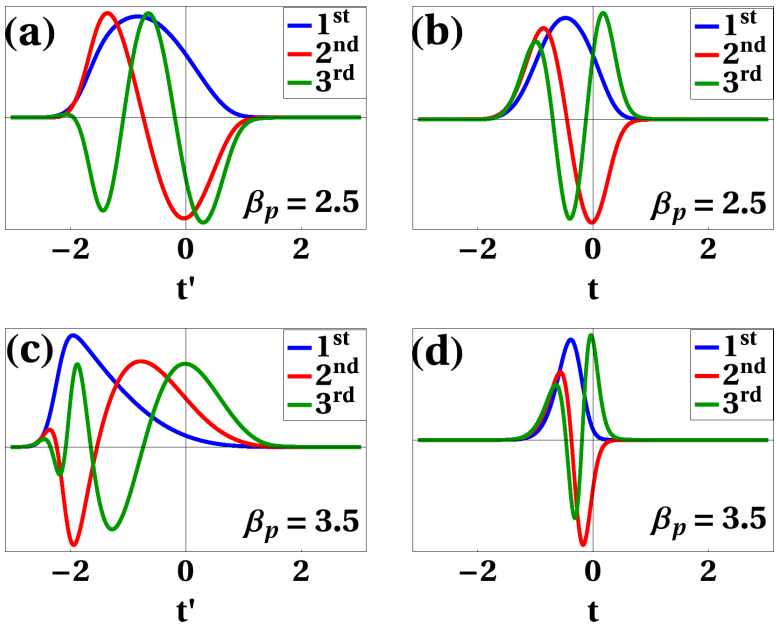

FIGURE 28. The first three s input (a,c) and r output (b,d) Schmidt modes for $\overline{\gamma} = 3.36$, $\tau_p = 0.5$, and $\beta_p' = 2.5$(a,b), and 3.5(c,d). $\beta_s' = 0$, $\beta_s' = 0$, $\beta_r' = 4$, $L = 1$. Numerical results. Reproduced from [40].

for every Δ in the range $[0, 2]$, the GF had the same selectivities for $\beta_p' = (2-\Delta)$ as well as $(2+\Delta)$. Even the Schmidt modes were identical but interchanged between the signal bands.

As the low-CE GF plots in Fig. 16 show, the pump-shape factor in $G_{rs}(t, t')$ has slope β_{sp}'/β_{rp}', defined in Eq. (4.18). For fixed $L = 1$, changing this slope, particularly for small pump widths, will change the projected width of the GF on the t and t' axes, which changes the widths of the Schmidt modes. This is also true for arbitrary CE's, as is shown in Fig. 28. Bringing β_p' closer to β_r' will tend to align $G_{rs}(t, t')$ with the vertical t'-direction. This increases the s-band Schmidt mode widths, and decreases the r-band Schmidt mode widths.

Figure 29 shows the plots of selectivity vs. $\overline{\gamma}$ for different β_p' values and pump widths. While in the SCuP regime, the selectivity-maximum was highest for $\tau_p \approx 1.5$. As β_p' drew closer to $\beta_r' = 4$, the optimum-selectivity-pump width was

seen to decrease. This is consistent with our finding for the GVM regime, which shows larger selectivity-maxima for shorter pumps. The selectivity-maximum also increased as we approached the GVM regime.

The selectivities for short-pumps were hyper-sensitive to changes in β_p' since the shape of the GF is affected the most (due to pump-factor slope defined in Eq. (4.18)) for shorter pumps. This implies that the closer we are to GVM regimes (but not in it), the shorter our pump needs to be for the FC to still be shape-preserving. Selectivities for wider-pumps did not show the same sensitivity to changes in β_p'.

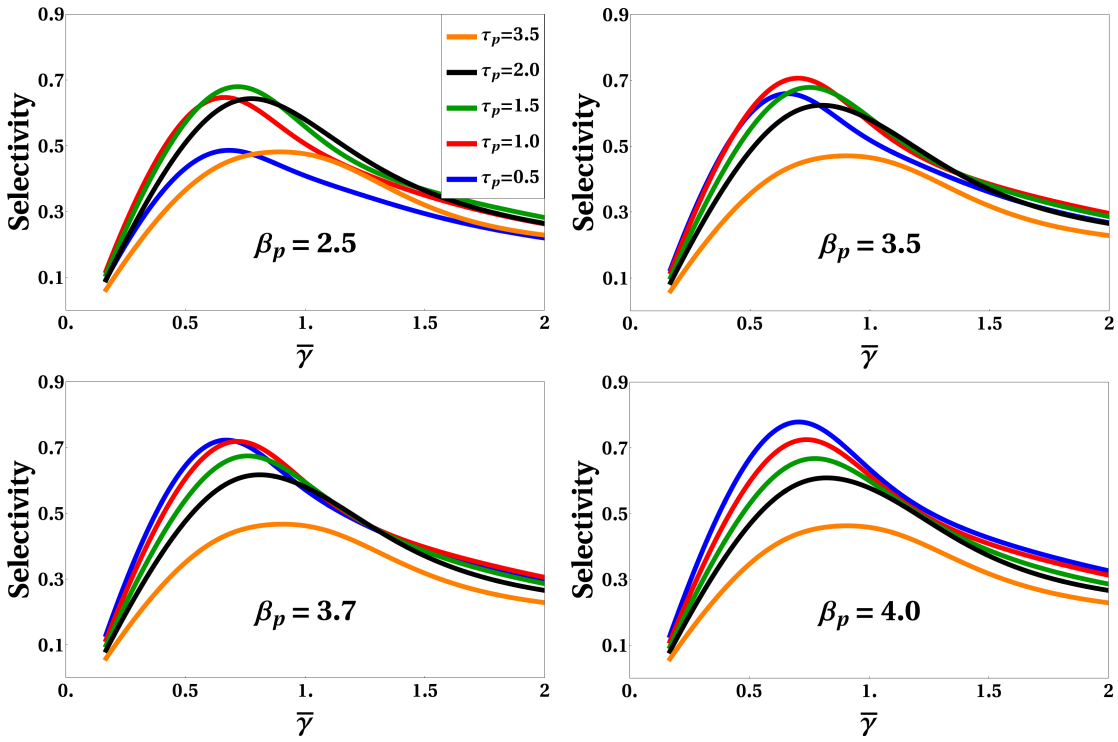

FIGURE 29. Selectivity vs. $\overline{\gamma}$ for Gaussian pumps of various widths and various β_p'. $\beta_s' = 0$, $\beta_r' = 4$, $L = 1$. Numerical results. Reproduced from [40].

($\beta'_{rp}\beta'_{sp} > 0$) co-propagating signals regime

In this subsection, I explore the regime in which the slope of the pump factor in the low-CE GF, i.e. the quantity β'_{sp}/β'_{rp} is positive. I do this by fixing $\beta'_p = 4$, $\beta'_s = 0$, $L = 1$, and varying β'_r within the range $[0, 4]$. Selectivity behavior for negative values of β'_r mapped bijectively to the corresponding positive β'_r that resulted in an inversion in pump-factor slope, while the Schmidt modes swapped across the r and s bands.

Figure 30 consists of selectivity vs. $\overline{\gamma}$ plots for various pump widths and β'_r. The selecivity maximum for any given τ_p, apart from decreasing in magnitude with decreasing β'_r, also migrates to higher $\overline{\gamma}$ values. This effect is more pronounced for shorter pumps. The optimum pump width (with the highest selectivity maximum) also increases with decreasing β'_r.

As $\beta'_r \to \beta'_s$, the pump-factor slope approaches unity. This allows for shape-preserving FC behavior when using short pumps, through a mechanism analogous to that illustrated in Fig. 27, except here the idler pulse convects through the pump in the same direction as the signal pulse. CE's for the first ten Schmidt modes for small β'_r tended to match each other, confirming non-shape-descriminatory GF. This "rotation" of the GF pump-factor causes the Schmidt mode widths to track the GF projection on the (t, t')-axes. The difference is most noticeable for short pumps (Fig. 31). The dominant Schmidt modes in both bands converge to matching shapes, as expected for shape-preserving FC.

The pump-factor slope can also be made to approach unity by keeping β'_r and β'_s fixed and increasing β'_p to very high magnitudes. This approach would maintain the spacing between the Heaviside step-functions and prevent the selectivity

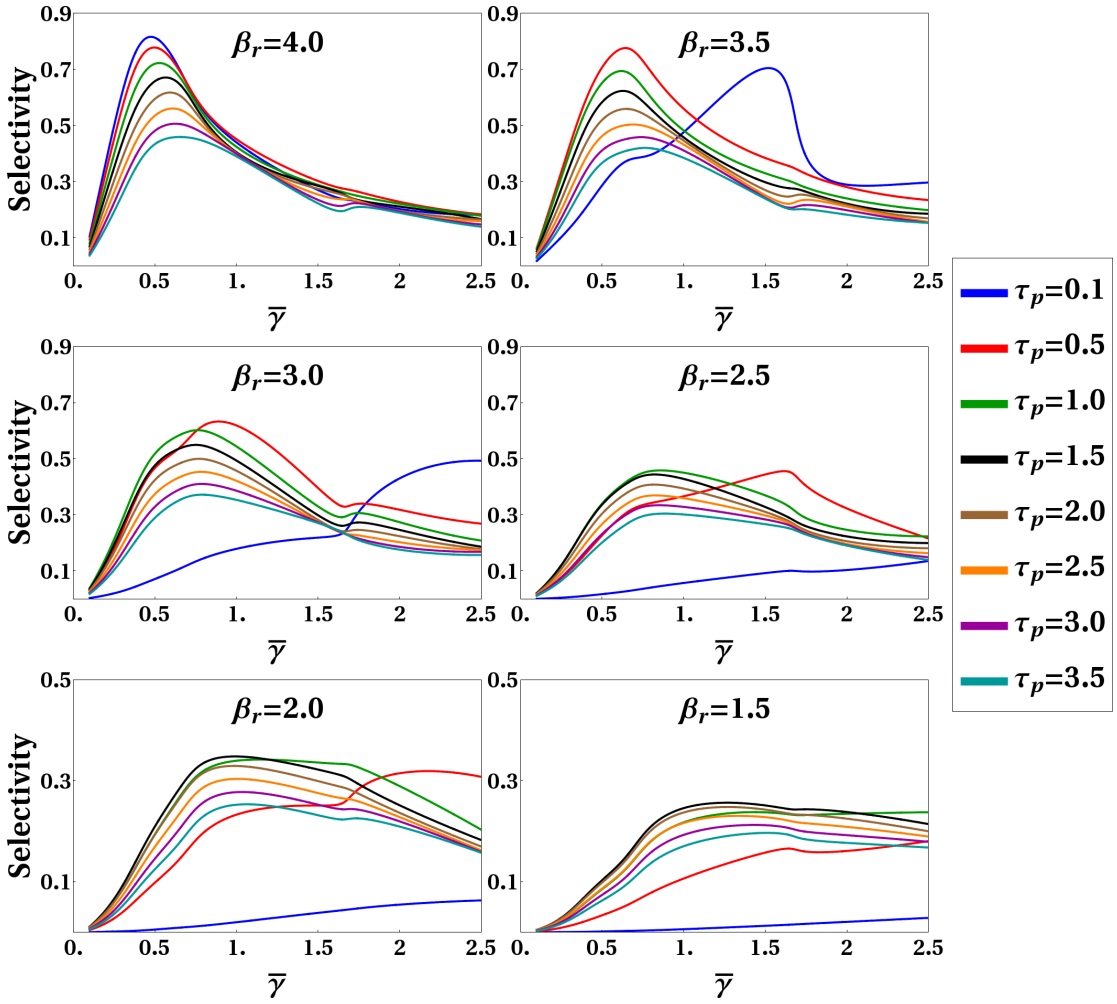

FIGURE 30. Selectivity vs. $\overline{\gamma}$ for Gaussian pumps of various τ_p and β'_r. $\beta'_p = 4$, $\beta'_s = 0$, $L = 1$. Numerical results. Reproduced from [40].

maximum from migrating to higher $\overline{\gamma}$ values. Numerical constraints restrain us from covering the entire range of the pump-factor slope using this method.

($\beta'_r = \beta'_s$) Exactly co-propagating signals regime

The ECoP regime is special in that I cannot plot the low-CE GF as I did for all the other regimes. As $\beta'_{rs} \to 0$, the separation between the Heaviside step-functions also converges to zero. We can however, explicitly write down

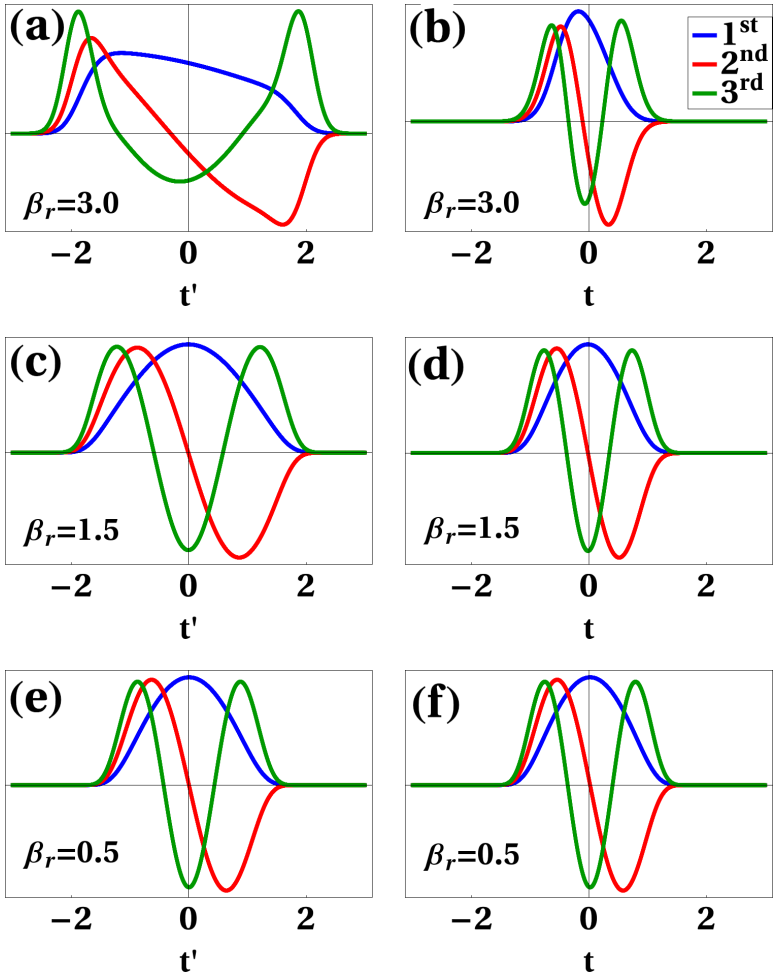

FIGURE 31. The first three s input (a,c,e) and r output (b,d,f) Schmidt modes for $\overline{\gamma} = 0.5$, $\tau_p = 0.5$, and $\beta'_r = 3.0$(a,b), 1.5(c,d), and 0.5(e,f). $\beta'_p = 4$, $\beta'_s = 0$, $L = 1$. Numerical results. Reproduced from [40].

the complete analytical solution for real pump-functions. If $\beta'_s = \beta'_r = 0$ and $A_p(x) \in \mathbb{R}$, then:

$$\partial_z A_r(z,t) = i\gamma A_p(t-\beta_p' z)A_s(z,t), \tag{4.24}$$

$$\partial_z A_s(z,t) = i\gamma A_p(t-\beta_p' z)A_r(z,t), \tag{4.25}$$

$$A_r(L,t) = A_r(0,t)\cos\left[P(L)\right] + iA_s(0,t)\sin\left[P(L)\right], \tag{4.26}$$

$$A_s(L,t) = A_s(0,t)\cos\left[P(L)\right] + iA_r(0,t)\sin\left[P(L)\right], \tag{4.27}$$

where $P(z) := (\gamma/\beta_p')\int_{t-\beta_p' z}^{t} A_p(x)dx$, and $\lim_{\beta_p'\to 0} P(z) = \gamma A_p(t)z$. The GF are δ-functions in t', and do not lend themselves to numerical Schmidt decomposition. This regime is beyond the scope of our simulation methodology.

The absence of walk-off between the two signal bands implies that the evolution of $A_r(z,t)$ for a given local time index 't' is insensitive to the global shapes of the input wavepackets ($A_r(0,t')$, $A_s(0,t')$). This results in a poor QPG. Different temporal slices of arbitrary input pulses will undergo the same transformation as they sweep across the pump, allowing for distortionless conversion.

Analytical solution for single-sideband, group-velocity matched regime

The GVM regime, where $\beta_s' = \beta_p'$, and all other parameters are arbitrary, was shown above to be the optimal regime for the drop/add process. Fortunately, in this same regime the problem can be solved analytically, following [83]. Consider the equations of motion [Eqs. (4.1) and (4.2)] for frequency conversion (FC) by

three-wave mixing (TWM):

$$(\partial_z + \beta'_r \partial_t)\bar{A}_r(z,t) = i\gamma A_p(t - \beta'_p z)\bar{A}_s(z,t), \tag{4.28}$$

$$(\partial_z + \beta'_s \partial_t)\bar{A}_s(z,t) = i\gamma A^*_p(t - \beta'_p z)\bar{A}_r(z,t). \tag{4.29}$$

For the group-velocity matched case in which $\beta'_s = \beta'_p$, it is convenient to define the retarded time variable $\tau = t - \beta'_s z$ and the normalized distance variable $\zeta = \beta'_r z - t$. By using these variables, one can rewrite the equations of motion in the simplified forms

$$\partial_\tau A_r(\tau,\zeta) = i\overline{\gamma} A_p(\tau) A_s(\tau,\zeta), \tag{4.30}$$

$$\partial_\zeta A_s(\tau,\zeta) = i\overline{\gamma} A^*_p(\tau) A_r(\tau,\zeta), \tag{4.31}$$

where the modified coupling coefficient $\overline{\gamma} = \gamma/\beta'_{rs}$ and the differential slowness (walk-off parameter) $\beta'_{rs} = \beta'_r - \beta'_s > 0$. The equations are to be solved for $-\infty < \tau < \infty$ and $0 \leq \zeta < \infty$. An easy way to do this is by Laplace transformation in space ($\zeta \to s$) [84, 85]. If an impulse is applied to the signal at the input boundary ($z = 0$), the transformed equations are

$$\partial_\tau A'_r(\tau,s) = i\overline{\gamma} A_p(\tau) A'_s(\tau,s), \tag{4.32}$$

$$sA'_s(\tau,s) = i\overline{\gamma} A^*_p(\tau) A'_r(\tau,s) + \delta(\tau - \tau'), \tag{4.33}$$

where τ' is the source time. If $H(\tau-\tau')$ is the Heaviside- step function and the effective time variable $\eta(\tau,\tau')=\int_{\tau'}^{\tau}|A_p(x)|^2dx$, the solutions are:

$$A_r'(\tau,s) = i\overline{\gamma}\frac{A_p(\tau')}{s}\exp[-\overline{\gamma}^2\eta(\tau,\tau')/s]H(\tau-\tau'), \tag{4.34}$$

$$A_s'(\tau,s) = \frac{\delta(\tau-\tau')}{s} - \left[\frac{\overline{\gamma}^2A_p^*(\tau)A_p(\tau')}{s^2}\right]\exp[-\overline{\gamma}^2\eta(\tau,\tau')/s]H(\tau-\tau'). \tag{4.35}$$

One can rewrite solutions in the space domain by using tables of inverse transforms [86]. The results are

$$A_r(\tau,\zeta) = i\overline{\gamma}A_p(\tau')J_0\{2\overline{\gamma}\sqrt{\eta(\tau,\tau')\xi}\}H_H(\tau,\tau',\zeta,\zeta'), \tag{4.36}$$

$$A_s(\tau,\zeta) = \delta(\tau-\tau')H(\xi) - \overline{\gamma}A_p^*(\tau)A_p(\tau')\sqrt{\xi/\eta(\tau,\tau')} \tag{4.37}$$

$$\times J_1\{2\overline{\gamma}\sqrt{\eta(\tau,\tau')\xi}\}H_H(\tau,\tau',\zeta,\zeta'), \tag{4.38}$$

where J_n is a Bessel function of order n, $\xi=\zeta-\zeta'$,and $H_H(\tau,\tau',\zeta,\zeta')=H(\tau-\tau')H(\zeta-\zeta')$. In the text, these solutions are referred to as the Green functions G_{rs} and G_{ss}, respectively.

If an impulse is applied to the idler at the input boundary, the transformed equations of motion and solutions are

$$\partial_\tau A_r(\tau,s) = i\overline{\gamma}A_p(\tau)A_s(\tau,s)+\delta(\tau-\tau'), \tag{4.39}$$

$$sA_s(\tau,s) = i\overline{\gamma}A_p^*(\tau)A_r(\tau,s), \tag{4.40}$$

$$\Rightarrow A_r(\tau,s) = \exp[-\overline{\gamma}^2\eta(\tau,\tau')/s]H(\tau-\tau'), \tag{4.41}$$

$$A_s(\tau,s) = i\overline{\gamma}\frac{A_p^*(\tau)}{s}\exp[-\overline{\gamma}^2\eta(\tau,\tau')/s]H(\tau-\tau'). \tag{4.42}$$

By using the aforementioned tables of inverse transforms [86], one finds that

$$A_r(\tau,\zeta) = H(\tau-\tau')\delta(\zeta-\zeta') - \overline{\gamma}\sqrt{\eta(\tau,\tau')/\xi} \tag{4.43}$$

$$\times J_1\{2\overline{\gamma}\sqrt{\eta(\tau,\tau')\xi}\}H_H(\tau,\tau',\zeta,\zeta'), \tag{4.44}$$

$$A_s(\tau,\zeta) = i\overline{\gamma}A_p^*(\tau)J_0\{2\overline{\gamma}\sqrt{\eta(\tau,\tau')\xi}\}H_H(\tau,\tau',\zeta,\zeta'). \tag{4.45}$$

These solutions are referred to as the Green functions G_{rr} and G_{sr}, respectively. These Green functions are stable analogs of the Green functions for stimulated Brillouin scattering (SBS) and stimulated Raman scattering (SRS) [84, 85], and are equivalent to the Green functions for anti-Stokes SRS [87].

The exact GF is found to be

$$G_{rr}(t,t') = H(\tau-\tau')\delta(\zeta-\zeta') - \overline{\gamma}\sqrt{\eta/\xi}J_1\{2\overline{\gamma}\sqrt{\eta\xi}\}H_H(\tau,\tau',\zeta,\zeta'), \tag{4.46}$$

$$G_{sr}(t,t') = i\overline{\gamma}A_p^*(\tau)J_0\{2\overline{\gamma}\sqrt{\eta\xi}\}H_H(\tau,\tau',\zeta,\zeta'), \tag{4.47}$$

$$G_{rs}(t,t') = i\overline{\gamma}A_p(\tau')J_0\{2\overline{\gamma}\sqrt{\eta\xi}\}H_H(\tau,\tau',\zeta,\zeta'), \tag{4.48}$$

$$G_{ss}(t,t') = \delta(\tau-\tau')H(\zeta-\zeta') - \overline{\gamma}A_p^*(\tau)A_p(\tau')\sqrt{\zeta/\eta}J_1\{2\overline{\gamma}\sqrt{\eta\xi}\}H_H(\tau,\tau',\zeta,\zeta'). \tag{4.49}$$

Here $\tau = t - \beta_s' L$, $\tau' = t'$, $\zeta = \beta_r' L - t$, $\zeta' = -t'$, $\xi = \zeta - \zeta'$, $\overline{\gamma} = \gamma/\beta_{rs}'$, and $\eta = \int_{\tau'}^{\tau} |A_p(x)|^2 dx$; $J_n(...)$ is the Bessel function of order n, and $H_H(\tau,\tau',\zeta,\zeta') = H(\tau-\tau')H(\zeta-\zeta')$, with $H(x)$ being the Heaviside-step function.

For an analysis of selectivity/separability, we need only consider the structure of $G_{rs}(t,t')$, which has two non-separable factors in (t,t'): the Bessel function $J_0\{2\overline{\gamma}\sqrt{\eta\xi}\}$, and the step-functions $H_H(\tau,\tau',\zeta,\zeta')$. Decreasing the pump width relative to the effective interaction time ($\beta_{rs}' L$) can diminish the ill effects of the step-functions on GF-separability, but the effect of the Bessel function worsens at

higher $\overline{\gamma}$. A numerical singular value decomposition of this analytical GF in Eq. (4.48) for high $\overline{\gamma}$ plotted in Fig. 32 confirms our numerical results from section 4.1.

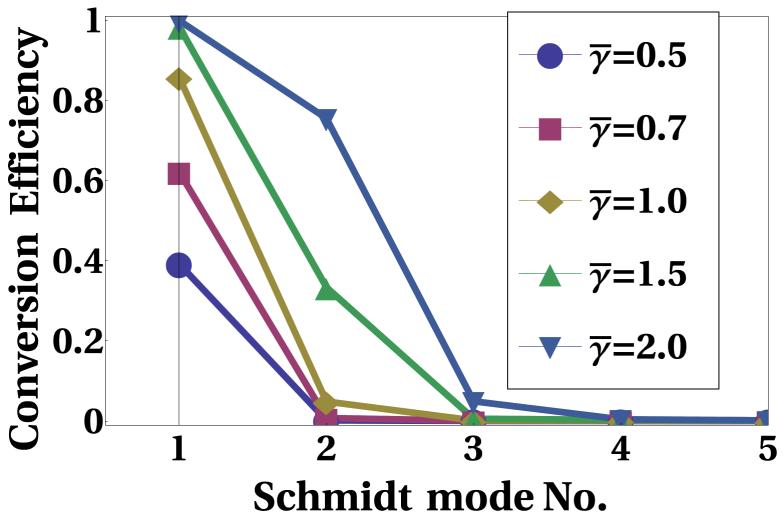

FIGURE 32. The first five dominant conversion efficiencies for the parameters in Fig. 18(b) and 43, for various $\overline{\gamma}$, GVM regime. Derived via SVD of the exact Green function $G_{rs}(t,t')$ (Eq. (4.48)). Reproduced from [40].

Increasing $\overline{\gamma}$ improves the CE of the first Schmidt mode by scaling the peak of the GF, but via the Bessel function, decreases the separability (Fig. 33). Hence, selectivity, being a product of the two, attains a maximum value at around $\overline{\gamma} \approx 1.15$. While decreasing pump width (τ_p) improves selectivity, the maximum asymptotically approaches a limiting value of approximately 0.85 (Fig. 34). This Bessel function induced distortion in GF shape is reflected in the shape of the Schmidt modes.

The statements made thus far hold true for arbitrary pump shapes, as long as $\beta'_{rs}L/\tau_p$ remains sufficiently large. Figure 35 shows the first two dominant s-band input Schmidt modes and r-band output Schmidt modes for two orthogonal

pump-pulse shapes (zeroth- and first-order Hermite-Gaussian pulses) in the GVM regime.

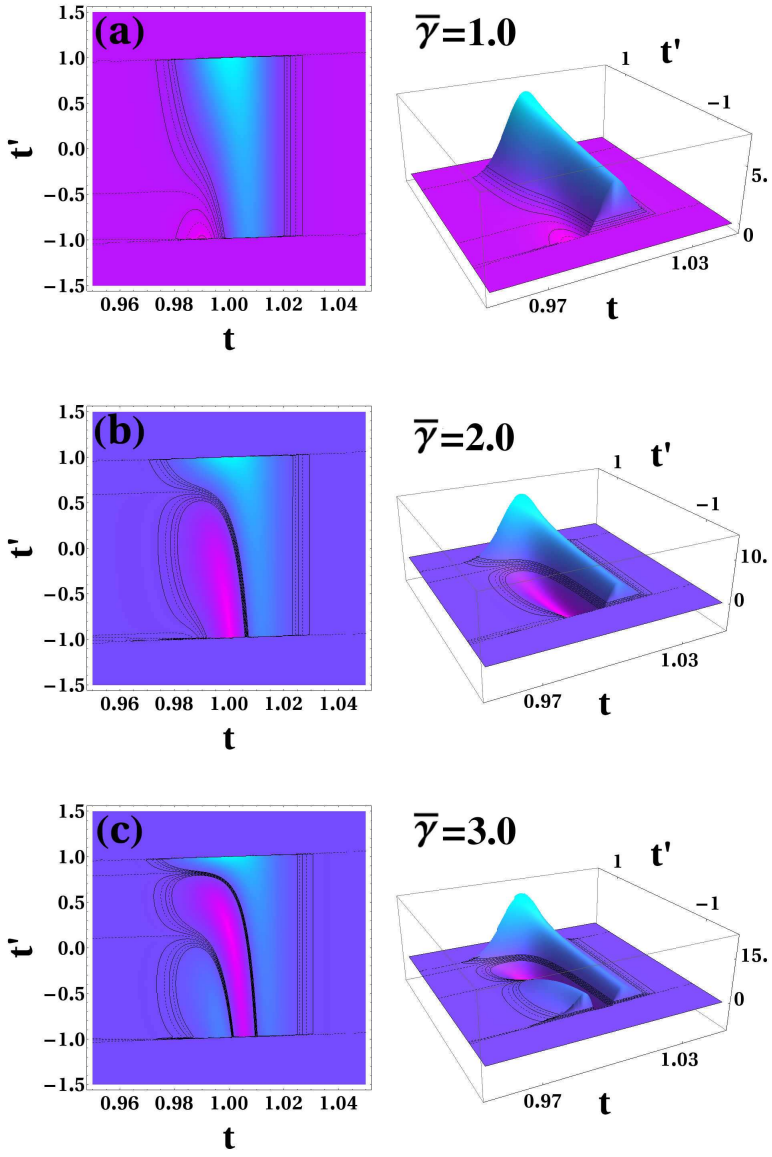

FIGURE 33. Green function for parameters in Fig. 18(a), $\tau_p = 0.01$, top and perspective-views, for **(a)** $\overline{\gamma} = 1.0$, **(b)** $\overline{\gamma} = 2.0$, **(c)** $\overline{\gamma} = 3.0$. Reproduced from [40].

Note the effect the pump shape has on the dominant s-band input Schmidt mode. Also note that the Schmidt coefficients are near identical.

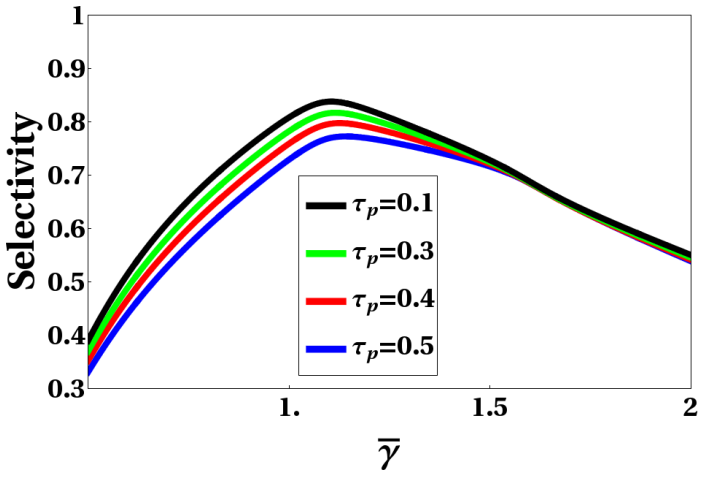

FIGURE 34. Selectivity vs. $\overline{\gamma}$ for parameters from Fig. 18(b) and 43, for various pump widths (τ_p), using $G_{rs}(t,t')$ in Eq. (4.48). Reproduced from [40].

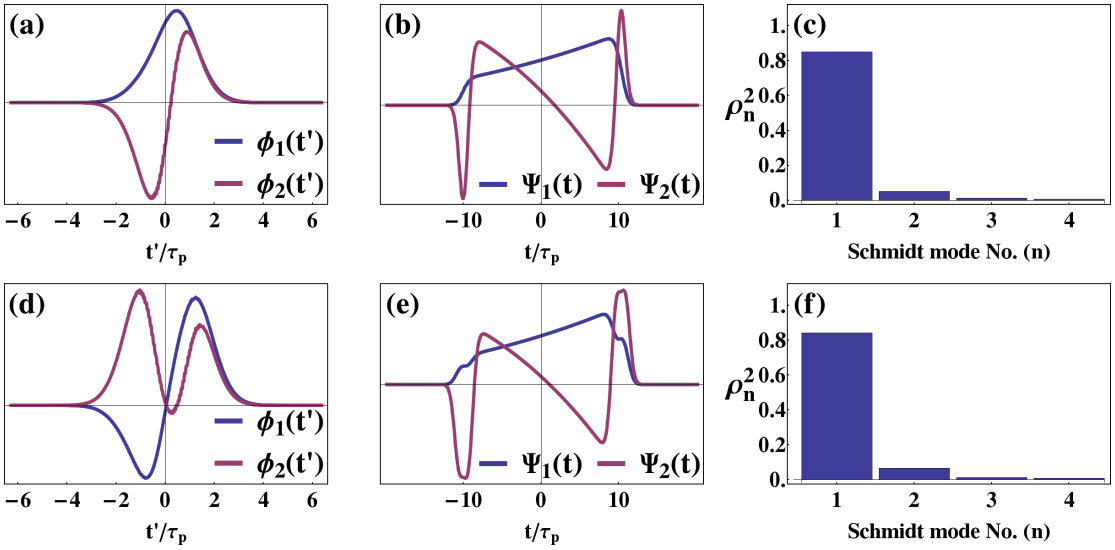

FIGURE 35. Numerically simulated, dominant Schmidt modes and conversion efficiencies for $\bar{\gamma}\sqrt{\beta'_{rs}L} = 0.707$, $\beta'_{rs}L/\tau_p = 20$ (GVM regime) with Gaussian (a, b, c) and first-order Hermite-Gaussian (d, e, f) pump pulses. Due to the lack of any complex phase structure in the pumps, the Schmidt modes end up being real valued (up to overall phase). Note that the first ($n = 1$) s-band input Schmidt modes (a, d) resemble the group-velocity matched, pump-pulse shapes up to temporal skewing, whereas the first r-band output Schmidt modes (b, e) get stretched relative to pump width by factor $\beta'_{rs}L/\tau_p = 20$. Also note the independence of the dominant Schmidt coefficients (c, f) from pump-pulse shape. Here, selectivity $S = 0.77$. Reproduced from [44].

One might suspect that including a frequency chirp in the pump field could improve the selectivity. I prove here that for the GVM regime this is not the case. The pump-squared integral $\eta(t,t')$, and consequently the Bessel function, is independent of any pump-chirp. To demostrate this, I rewrite Eqs. (4.1) and (4.2) in the pump's moving frame:

$$(\partial_z + \beta'_{rp}\partial_t)A_r(z,t) = i\gamma A_p(t)A_s(z,t), \tag{4.50}$$

$$(\partial_z + \beta'_{sp}\partial_t)A_s(z,t) = i\gamma^* A_p^*(t)A_r(z,t). \tag{4.51}$$

Replacing the pump envelope-function by its real-amplitude and phase ($A_p(t) := P(t)\exp[i\theta(t)]$) and setting $\beta'_{sp} = 0$ for the GVM constraint, we get:

$$(\partial_z + \beta'_{rp}\partial_t)A_r(z,t) = i\gamma P(t)\exp[i\theta(t)]A_s(z,t), \tag{4.52}$$

$$\partial_z A_s(z,t) = i\gamma^* P(t)\exp[-i\theta(t)]A_r(z,t). \tag{4.53}$$

By redefining the s-band envelope function as $\overline{A}_s(z,t) = A_s(z,t)\exp[i\theta(t)]$, we can recover Eqs. (4.1) and (4.2) with a real-pump envelope in the GVM regime. Any time dependent complex phase in the pump gets absorbed into the Schmidt modes, without affecting the CE's or GF selectivity. Nevertheless, for any given $\overline{\gamma}$, the shape of the pump gives us some control over the shapes of the Schmidt modes, and this may be used to tune the QPG to accept easy-to-produce pulse shapes as input Schmidt modes.

The parameter $(\beta'_{rs}L)$ is responsible for the Schmidt mode width for the band with velocity mismatched with that of the pump. This parameter has units of time, and is a measure of the duration of "interaction." Increasing $\beta'_{rs}L$ in the GVM regime will make higher CE's attainable at higher pump powers but lower $\overline{\gamma}$. The

selectivity maximum also follows a similar trend until $\beta'_{rs}L$ becomes comparable to pump width τ_p (at which point the slope of the Heaviside-step functions reduces overall GF separability), as shown in Fig. 36.

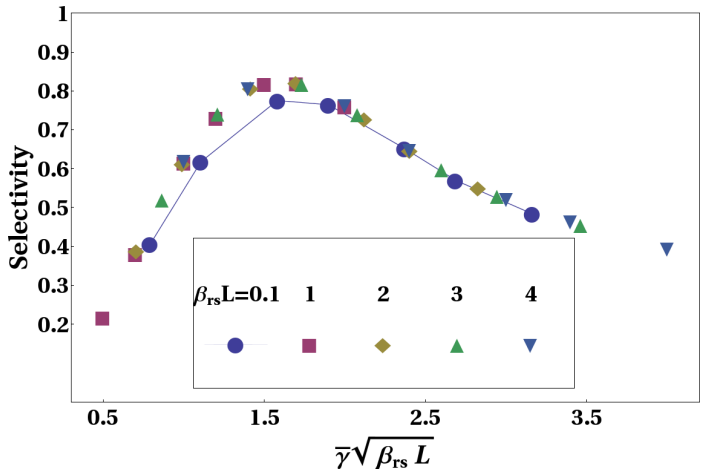

FIGURE 36. Selectivity vs. $\overline{\gamma}\sqrt{\beta'_{rs}L}$ for parameters from Fig. 18(b), with various $\beta'_{rs}L$. The joined plot for $\beta'_{rs}L = 0.1 = \tau_p$ has a lower maximum than all other plots. Reproduced from [40].

The universality curve in Fig. 36 indicates that the selectivity barrier is fundamental to single-stage, constant dispersion systems. Arbitrary sets of parameter values can all be scaled into dimensionless ones that will be fit well by this curve (for GVM with large $\beta'_{rs}L/\tau_p$) or remain below it.

The GVM regime ($\beta'_s = \beta'_p$), under the $\beta'_{rs} \to 0$ limit also converges to Eqs. (4.26) and (4.27). Taking the limit whilst still enforcing GVM conditions will cause $\beta_p \to 0$ as well. I now verify that the exact GVM analytical solution consistently reduces to the expected sinusoidal form expressed in section 4.5. Consider $G_{rs}(t,t')$ from Eq. (4.48) for the input condition $A_r(0,t') = 0$:

$$A_r(L,t) = i\overline{\gamma}\int_{t-\beta_r L}^{t-\beta_s L} dt' A_p(t') J_0\{2\overline{\gamma}\sqrt{\eta\xi}\} A_s(0,t') \tag{4.54}$$

$$= i\frac{\gamma}{\beta_{rs}} \int_0^{\beta_{rs}L} dt'' A_p(t''+t-\beta_r L) A_s(0, t''+t-\beta_r L) J_0 \left[\frac{2\gamma}{\beta_{rs}} \left(t'' \int_{t''+t-\beta_r L}^{t-\beta_r L+\beta_{rs}L} |A_p(x)|^2 dx \right)^{1/2} \right]. \tag{4.55}$$

Since t'' is being integrated from 0 to $\beta_{rs}L$, $\beta_{rs} \to 0 \Rightarrow t'' \to 0$. Then the integral inside the bessel argument reduces to $(\beta_{rs}L - t'')|A_p(t - \beta_r L)|^2$.

I then use

$$\frac{g}{y} \int_0^y dt'' J_0 \left[|g| \frac{\sqrt{t''(y-t'')}}{y} \right] = 2 \sin\left(\frac{g}{2}\right) \tag{4.56}$$

$$\Rightarrow A_r(L,t) = i A_s(t-\beta_r L) \sin\left[\gamma L A_p(t-\beta_r L)\right], \tag{4.57}$$

which is identical to Eq. (4.26) for $\beta_r = 0$ and $A_r(0,t) = 0$.

The non-separability arising from the Bessel function in the GF can be traced to the oscillations shown in Fig. 33. These are similar to those in Burnham-Chiao ringing [88] seen in fluorescence induced by short-pulse excitations by the propagation of short, weak pulses through a resonant atomic medium. To model an analogy, the phase- and energy-matched wave-mixing process may be represented by a 2-level pseudo-atomic-medium with a ground-state energy at ω_p and an excited state at ω_s. Any finite-width input pulse in r band with energy resonant with the atomic-medium ($\omega_r = \omega_s - \omega_p$) will have a non-zero bandwidth in the frequency domain. As it interacts with the medium, its spectral-components detuned above resonance will acquire a different phase shift than the spectral components below resonance. These two spectral components will beat to produce the ringing effect, resulting in the oscillations seen in Fig. 33. The Bessel function factor is a fundamental barrier that restricts selectivity in the GVM regime (which is thought to be the optimal one). Some groups [30, 78] have sought to make the

waveguide properties non-uniform [$\gamma \rightarrow \gamma(z)$] in an attempt to overcome this limitation, with limited success.

Temporal-Mode Interferometry

Thus far I have extensively analyzed the general model for three-wave mixing with pulsed modes convecting at arbitrary but fixed group velocities in a nonlinear medium. In the quest for a QPG however, we appear to have hit an impasse. While we could trivially find parameters for which frequency conversion of an input temporal mode occurs with high separability at low conversion efficiencies, I have shown that the separability will have to be sacrificed to gain efficiency. Figure 37 summarizes this by illustrating the temporal skewing of the dominant Schmidt mode relative to the pump shape with increasing pump power for two different pump shapes. Also shown are the top four Schmidt mode CEs.

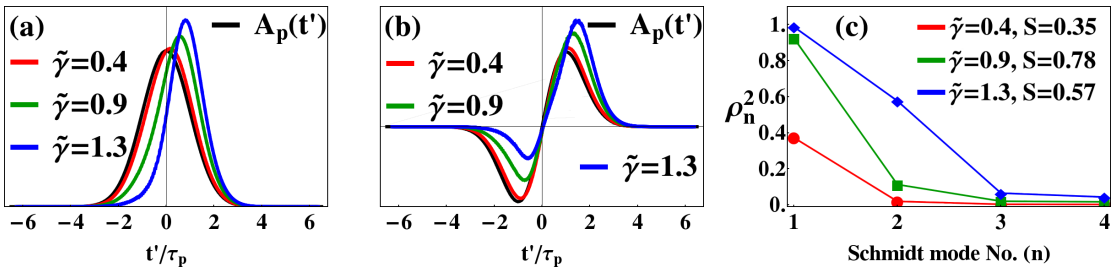

FIGURE 37. Numerically simulated, first ($n = 1$) s-band input Schmidt modes ($\phi_1(t')$) for $\zeta = 20$, $\xi = \infty$, and various $\widetilde{\gamma}$ with (a) Gaussian pump pulses, and (b) first-order Hermite-Gaussian pump pulses. These plots demonstrate the $\widetilde{\gamma}$-dependent temporal skewing effect. (c) The conversion efficiencies for the first four dominant Schmidt modes. Plot (c) is identical for both pump-pulse shapes. The selectivities are given in the legend. Reproduced from [44].

Figure 38 schematically depicts the operation of an ideal QPG. If the system parameters controlling the forms of the Green-function kernels are set right, then the device should frequency convert the desired s-input TM (say, $\phi_1(t')$) into the

r-band with unity efficiency, whilst completely retain full power/amplitude of any orthogonal s-input TM (say, $\psi_2(t')$) within the s-band, as shown. But in reality, the device we end up with is the one shown in Fig. 39, which partially converts the input TM $\phi_n(t)$ with efficiency/probability ρ_n^2. This is true not just of frequency conversion in three-wave mixing, but all systems involving stagnant dispersive media and convecting pulses that interact.

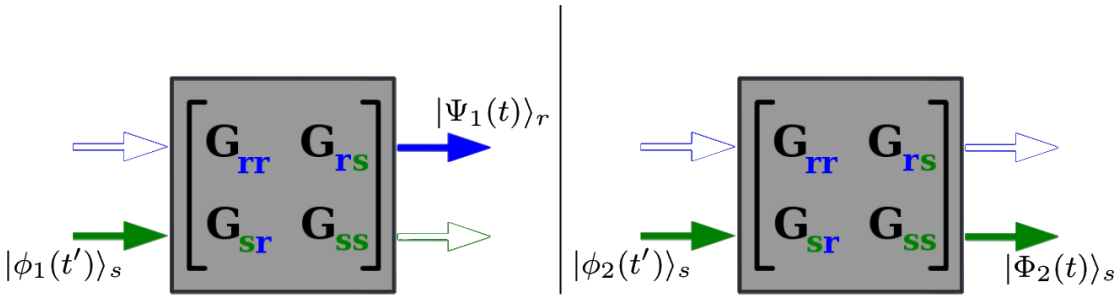

FIGURE 38. Schematic depicting the ideal QPG that selectively frequency shifts the desired TM $\phi_1(t')$, whilst retaining all orthogonal TMs within the same band.

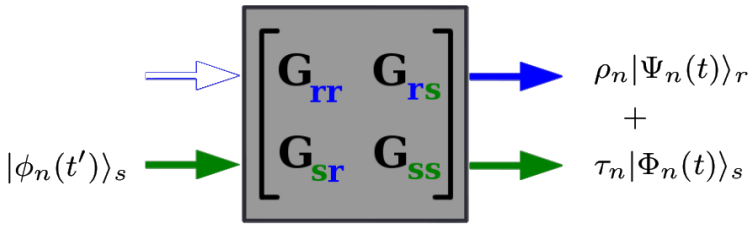

FIGURE 39. The more accurate single-stage frequency conversion device, which takes any TM input and generates a color-superposition at the output.

I now note that the device depicted in Fig. 39 is governed by physical Maxwell's equations, and therefore obeys time-reversal symmetry. Meaning that while a single-photon within a frequency-band state gets converted into a superposition of two frequency-band states, i.e. a color-superposition state, the same device when run backwards will accept the color-superposition state as an input, and generate a single frequency-band state, the precise color being dictated

by the relative phase between the two colors. It is now a straightforward exercise to cascade two FC devices, with the color-superposition state of the first serving as the input for the second, as shown in Fig. 40. If we were to operate both the stages at the pump powers required for 50% conversion of the dominant Schmidt mode, then we would have constructed a Mach-Zehnder interferometer, where the two intermediate paths correspond to two different frequency bands. Note (Fig. 37) that the GVM regime affords us good separability even up to 50% CE. Meaning that all TMs orthogonal to the dominant Schmidt mode would see the two beam splitters as transparent. Thus, we will have interferometrically enhanced CE of a single mode selectively more than other orthogonal modes.

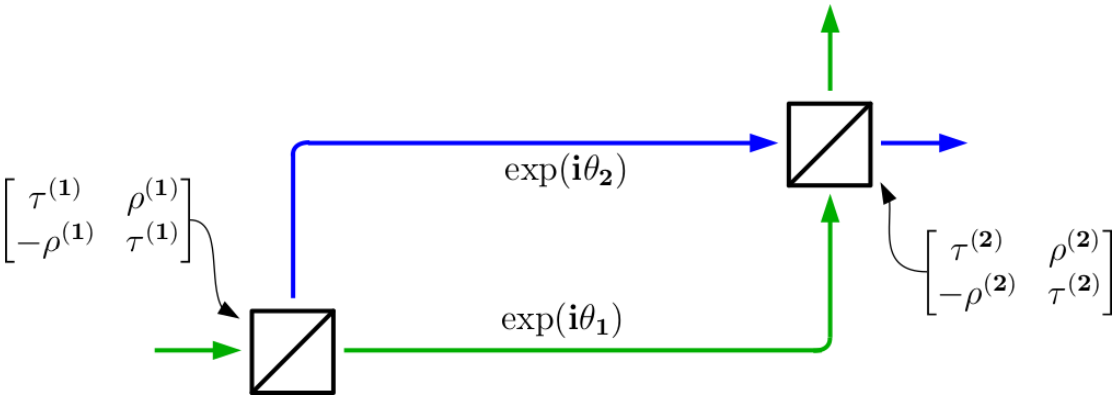

FIGURE 40. Mach-Zehnder interferometer with Doppler-shifting beam splitters. The beam splitter coefficients are now dependent on the input TM state.

This scheme, which we call temporal-mode interferometry (TMI), uses cascaded stages of QFC, as shown in Fig. 41. The method theoretically provides close to 100% TM selectivity, opening the door for manipulation of TM qubits or multi-level qudits, and may also be used for TM band multiplexing in classical optical telecommunications. In the figure I color code the participating frequency bands s in green, and r in blue for the signal photons, as well as p the strong pump field in red. Our method exploits the fact that using single-stage QFC,

it is possible to discriminate orthogonal TMs nearly perfectly up to a conversion efficiency (CE) of about 50% [40, 83]. This motivates a two-stage interferometric scheme, in which each stage is configured for 50% CE for the target TM, and functions as a 50/50 beam splitter with the r- and s-frequency bands representing its two input and output arms. An s-input photon in the target TM will be 50% frequency converted in the first stage into the r band with a phase picked up from the pump field. If all fields are allowed to participate in QFC in the second stage with the right relative phases, the two effective beam splitters will function as a frequency-shifting Mach-Zehnder (or Ramsey) interferometer, allowing for complete forward or backward conversion of the state of the photon, depending on the value of the additional relative phase θ introduced between the stages. Between the two stages, the target TM component of the signal photon is in a multicolor superposition of the signal-idler frequency bands (*i.e.* a color qubit)[81, 82, 89, 90]. This interferometric scheme was first published by us [41]. Phase coherence between frequency-converted and unconverted components of light has since been experimentally demonstrated for weak-coherent states by Clemmen *et al.* [81, 91], who independently arrived at the frequency-conversion interferometry idea, and later by Kobayashi et. al. [82]. However, both their implementations used continuous pumps and so are not TM selective. In our case, the interferometric frequency-conversion effect operates only on the target TM, as the orthogonal modes have negligible CE in both stages.

There are two configurations of interest: 1) 'reversed collision' (RC), in which the dispersion in the second-stage is inverted relative to that in the first stage, such that the relative group velocities of the pulses are reversed, and 2) 'double collision' (DC), in which the dispersion in the second-stage is identical to that in

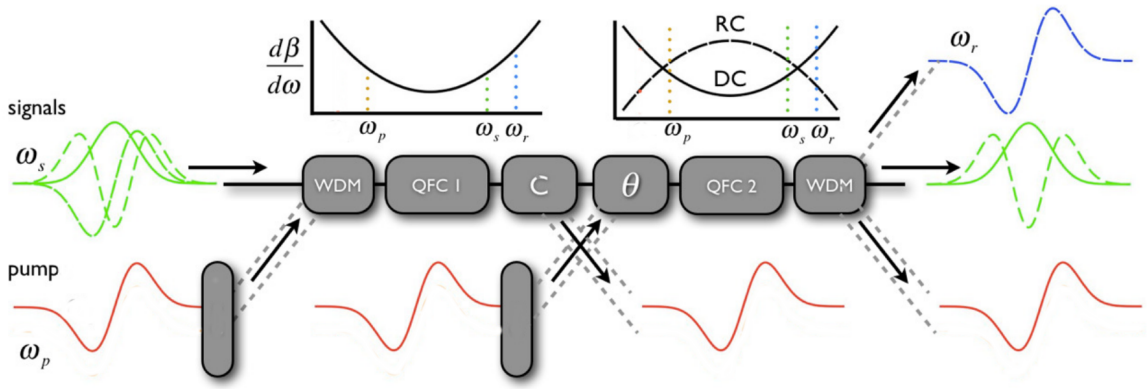

FIGURE 41. Temporal-mode interferometer using two nonlinear media (QFC 1 and QFC 2) with identical (DC) or opposite-sign (RC) dispersion. Appropriate choices for pump-pulse shapes, pump powers and the phase shift θ will selectively frequency convert a specific s (green, ω_s) TM into an r (blue, ω_r) TM at a different central frequency, whilst not affecting temporally-orthogonal s-input TMs. WDM stands for wavelength-division multiplexer. The coupler C contains frequency dependent delays for the DC case. Reproduced from [41].

the first. In the DC case, the fast pulses must be time delayed relative to the slow pulses in between the stages so that they walk through each other again in the second stage. The inset in Fig. 41 shows the inverse group velocity vs. frequency for the two configurations. The necessary time delays for the DC case are implemented in the 'coupler' labeled C in the figure. After the target TM is frequency converted, it would be separated from the main beam using a standard wavelength-division multiplexer (WDM). As shown below, for TWM I predict in the RC case a TM selectivity of 0.9846, and in the DC case the selectivity is 0.9805, far higher than can be achieved with single-stage systems. High TM selectivity can also be achieved using FWM, but will require chirp pre-compensation of the pump pulses to be implemented in modules labeled PC, as will be discussed in the next section.

For the two-stage temporal-mode interferometry, the combined Green function kernel $G_{rs}(t, t')$ is given by the interferometric equation [40]

$$G_{rs}(t,t') = \int_{-\infty}^{\infty} \mathrm{d}t'' \left[G_{rs}^{(2)}(t,t'') G_{ss}^{(1)}(t'',t') + e^{i\theta} G_{rr}^{(2)}(t,t'') G_{rs}^{(1)}(t'',t') \right], \qquad (4.58)$$

where the superscripts indicate the FC process in stages 1 and 2. Functions and parameters lacking a superscript stage number characterize the combined two-stage process as a whole. For each stage separately, the 'transmission' (no frequency change) coefficient $\tau_n^{(\xi)}$ and the 'reflection' (frequency change) coefficient $\rho_n^{(\xi)}$, both taken to be real without loss of generality, independently obey relations analogous to beam-splitter relations, $\tau_n^{(\xi)2} + \rho_n^{(\xi)2} = 1$. The stage-labeled input modes are represented by lower-case functions $(\psi^{(\xi)}, \phi^{(\xi)})$ and output modes by upper case $(\Psi^{(\xi)}, \Phi^{(\xi)})$.

For TWM described by Eqs. 4.1-4.2, the Schmidt coefficients are independent of pump-pulse shape, and are determined by the value of γ. In contrast, the Schmidt mode shapes are determined by the pump-pulse shape and the value of γ [83]. In TWM, which uses of a single pump, one can influence the Schmidt mode shapes of the group-velocity-matched signal band to be roughly identical to the pump shape.

To recap, the unitarity of the single-stage transformation imposes a pairing between the Schmidt modes across the r and s bands for that stage [92]. If the input fields for a given stage are represented as

$$A_r^{(\xi)}(t')\big|_{\mathrm{in}} = \sum_n a_n \psi_n^{(\xi)}(t'), \qquad (4.59)$$

$$A_s^{(\xi)}(t')\big|_{\mathrm{in}} = \sum_n b_n \phi_n^{(\xi)}(t'), \qquad (4.60)$$

then the output fields are expressed as

$$A_r^{(\xi)}(t)\big|_{\text{out}} = \sum_n (\tau_n^{(\xi)} a_n + \rho_n^{(\xi)} b_n)\Psi_n^{(\xi)}(t), \tag{4.61}$$

$$A_s^{(\xi)}(t)\big|_{\text{out}} = \sum_n (\tau_n^{(\xi)} b_n - \rho_n^{(\xi)} a_n)\Phi_n^{(\xi)}(t). \tag{4.62}$$

The expressions in brackets are equivalent to a beam-splitter transformation, explaining why the QFC process is considered background-free in principle [92].

The operating principle of the TMI can be summarized simply as follows. Consider the case that the input field to stage 1 is a single temporal mode $A_s^{(1)}(t)|_{\text{in}} = b_n \phi_n^{(1)}(t)$, and the r-input field is empty. Then the output fields of stage 1, and thus the input fields of stage 2, are

$$A_s^{(1)}(t)\big|_{\text{out}} = \tau_n^{(1)} b_n \Phi_n^{(1)}(t) = A_s^{(2)}(t)\big|_{\text{in}}, \tag{4.63}$$

$$A_r^{(1)}(t)\big|_{\text{out}} = \rho_n^{(1)} b_n \Psi_n^{(1)}(t) = e^{-i\theta} A_r^{(2)}(t)\big|_{\text{in}}, \tag{4.64}$$

where a phase shift θ of the r field has been introduced intentionally by the experimenter before the fields enter stage 2. Then the output of stage 2 will be

$$A_s^{(2)}(t)\big|_{\text{out}} = b_n \sum_{m=1}^{\infty} \left(\tau_m^{(2)} \tau_n^{(1)} \mu_{m,n} - e^{i\theta} \rho_m^{(2)} \rho_n^{(1)} \eta_{m,n}\right) \Phi_m^{(2)}(t), \tag{4.65}$$

$$A_r^{(2)}(t)\big|_{\text{out}} = b_n \sum_{m=1}^{\infty} \left(\rho_m^{(2)} \tau_n^{(1)} \mu_{m,n} + e^{i\theta} \tau_m^{(2)} \rho_n^{(1)} \eta_{m,n}\right) \Psi_m^{(2)}(t), \tag{4.66}$$

where the 'inter-stage mode overlaps' are defined as

$$\mu_{m,n} = \int dt \phi_m^{(2)*}(t) \Phi_n^{(1)}(t), \tag{4.67}$$

$$\eta_{m,n} = \int dt \psi_m^{(2)*}(t) \Psi_n^{(1)}(t). \tag{4.68}$$

If $|\mu_{n,n}| = |\eta_{n,n}| = 1$, then we say the processes in the two stages are temporally mode matched. This occurs only if the dominant output modes of stage 1 coincide with the corresponding input modes of stage 2 in each frequency band, that is $\Phi_n^{(1)}(t) = \phi_n^{(2)}(t)$, and $\Psi_n^{(1)}(t) = \psi_n^{(2)}(t)$.

For the target mode $n = 1$, we wish to have $A_s^{(2)}(t)\big|_{\text{out}} = 0$ and $A_r^{(2)}(t)\big|_{\text{out}} = b_1 \Psi_1^{(2)}(t)$. This can only occur if several conditions are met: **1)** the non-dominant Schmidt coefficients $\rho_{n\neq 1}^{(\xi)}$ are nearly zero; **2)** the dominant processes in the two stages are temporally mode matched; and **3)** the dominant Schmidt coefficients are $\rho_1^{(\xi)} = \tau_1^{(\xi)} = \sqrt{1/2}$. Then the phase θ needs to be adjusted to zero (or some other value if the mode overlaps are complex). This gives $(\tau_1^{(2)}\tau_1^{(1)}\mu_{1,1} - e^{i\theta}\rho_1^{(2)}\rho_1^{(1)}\eta_{1,1}) = 0$ and $(\rho_1^{(2)}\tau_1^{(1)}\mu_{1,1} + e^{i\theta}\tau_1^{(2)}\rho_1^{(1)}\eta_{1,1}) = 1$. If these conditions are met, then by varying the phase of the r signal field between the stages, either frequency band in mode N can be 100% populated at the output of stage 2.

Since the remaining (non-target) modes ($n \neq 1$) have $\rho_n^{(\xi)} \approx 0, \tau_n^{(\xi)} \approx 1$. So, light in any one of these modes is not significantly frequency converted in either stage, although there would be a change of temporal mode shape if $\Phi_n^{(2)}(t) \neq \phi_n^{(1)}(t)$, creating temporal mode distortion.

For many applications, especially those involving cascaded TM operations, it would be highly beneficial to implement TMI without temporal mode distortion of the non-converted signals. This is achieved if the output Schmidt modes of stage 2

match the input Schmidt modes of stage 1, that is $\Phi_n^{(2)}(t) = \phi_n^{(1)}(t)$, and $\Psi_n^{(2)}(t) = \psi_n^{(1)}(t)$ for every n. The RC configuration satisfies this requirement along with the conditions $\Phi_n^{(1)}(t) = \phi_n^{(2)}(t) = \Phi_n(t) = \phi_n(t)$ and $\Psi_n^{(1)}(t) = \psi_n^{(2)}(t) = \Psi_n(t) = \psi_n(t)$ (*i.e.* the output Schmidt modes are identical to the input Schmidt modes for both signal bands), leading to the elimination of temporal distortion if the non-converted input modes are identical to the input Schmidt modes of the system.

Consider the case in which the target mode is 50% converted in each stage individually while orthogonal modes remain almost completely unconverted. Then, using Eqs. (4.4) in Eq. (4.58) shows the need for inter-stage temporal mode matching between the output Schmidt modes of the first stage and the input Schmidt modes of the second stage for the scheme to work. Figure 42 shows the plots for the input and output Schmidt modes of both stages for both RC and DC configuration TMI, with a Gaussian pump, and the parameter $\zeta = |\beta'_{rs}|l/\tau_p = 200$, where l is the per stage medium length and τ_p is the Gaussian pump width. The Schmidt modes of a single band for a given stage are found to be temporally symmetrically skewed in opposite directions between the input and the output, the direction being dependent on the sign of (β'_{rs}). Consequently, the inter-stage mode matching will be exact for the RC configuration, and inferior for the DC configuration. For $\zeta = 200$, the RC $\mu_{1,1}^{TWM} = \eta_{1,1}^{TWM} = 1$. But for DC, $\mu_{1,1}^{TWM} = 0.983$ and $\eta_{1,1}^{TWM} = 0.901$.

Figures 43(a-d) Schmidt modes for the RC configuration TWM-TMI for $\zeta = 200$ and a Gaussian pump. The selectivity S was computed to be 0.9846 ($|\rho_1|^2 = 0.9975$, $|\rho_2|^2 = 0.0110$). ζ is also the ratio of time-widths of the r- and s-Schmidt modes. The CE of the first four Schmidt modes (*i.e.* $|\rho_n|^2$) are plotted in green in Fig. 44(a), along with the CE of the same Schmidt modes when using a custom

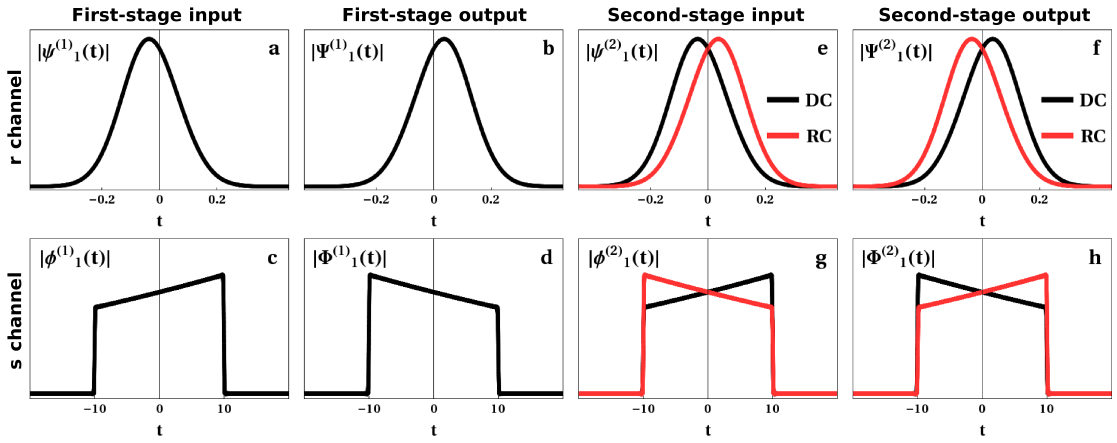

FIGURE 42. The dominant input (a, c, e, g) and output (b, d, f, h) Schmidt modes for the first-(a, b, c, d) and second-(e, f, g, h) stages for both s (a, b, e, f) and r (c, d, g, h) bands for both RC (red, lighter shade) and DC (black) configurations of TWM-TMI for a Gaussian-shaped pump, and $\zeta = |\beta_r' - \beta_s'|l/\tau_p = 200$. The values of t are relative to a $|\beta_r' - \beta_s'|l$ of 20. Due to the nature of temporal skewing, the inter-stage mode-matching between the first-stage output Schmidt modes (b, d) and the second-stage input Schmidt modes (e, g) is larger for the RC than the DC configuration, thus yielding better selectivity. The complete two-stage composite system Schmidt modes for TWM-TMI in the RC configuration are plotted in Fig. 43. Reproduced from [42].

pump shape (magenta) tailored to 'drop' the second s-input Schmidt mode. Since the TWM pump can influence only the shape of the s-band Schmidt modes, the tailored pump in Fig. 44(b) will frequency convert the second s-input Schmidt mode from Fig. 43(a) into an r-band TM identical to the first r-output Schmidt mode from Fig. 43(d).

As an example, with a Gaussian pump, a signal photon in the s-band with shape $\psi_1(t)$ [Fig. 43(a)] will be frequency converted into an r-band photon with shape $\Phi_1(t)$ [Fig. 43(d)], with an efficiency of $|\rho_1|^2 = 0.9975$. In contrast, a photon in the s-band with shape $\psi_2(t)$ will be frequency converted into an r-band photon with shape $\Phi_2(t)$, with a very small efficiency of $|\rho_2|^2 = 0.0110$. In other words, an s-band photon stays in the s band with probability 0.9890, and will exit the

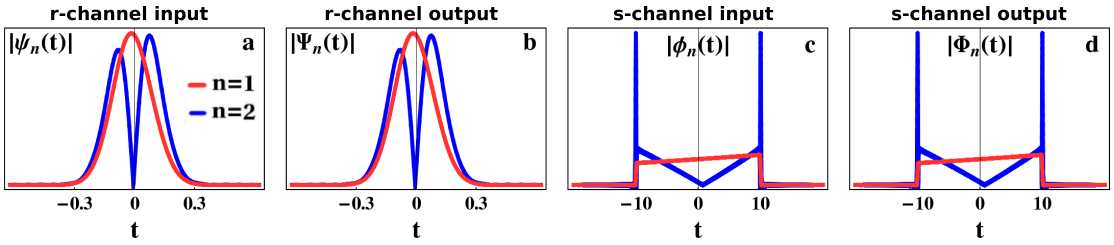

FIGURE 43. Schmidt modes for TWM-TMI in the RC configuration with Gaussian pump, and $\zeta = |\beta'_r - \beta'_s|l/\tau_p = 200$, yielding a selectivity of 0.9846. The magnitudes of the first two Schmidt modes are shown for s-input (a), s-output (b), r-input (c), and r-output (d). Values of t are relative to a $|\beta'_{rs}|l$ of 20. Fig. 44 shows the conversion efficiencies of the first four Schmidt modes for two different pump shapes. Reproduced from [42].

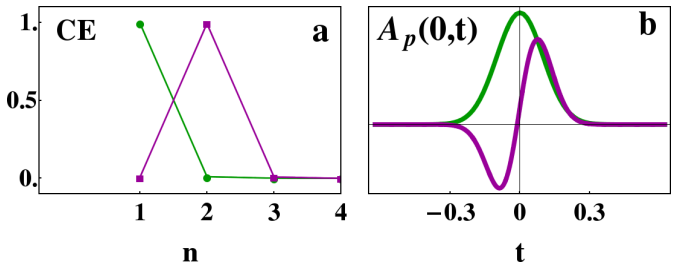

FIGURE 44. (a) Conversion efficiencies for Gaussian-pumped-TWM-TMI Schmidt modes in the RC configuration. The CE for a Gaussian pump are shown in green (darker shade), and those for a custom pump shape tailored to drop the second Schmidt mode are shown in magenta (lighter shade). (b) The corresponding pump shapes shown with matching colors. Values of t are relative to a $|\beta'_{rs}|l$ of 20. Reproduced from [42].

device with shape $\Psi_2(t)$ (Fig. 43(b)). Figure 43(c) comes into play only if the input photon is in the r-band.

For the DC configuration with $\zeta = 200$, I computed a selectivity of 0.9805 (with $|\rho_1|^2 = 0.9957$, $|\rho_2|^2 = 0.0134$). This is slightly lower than the RC configuration due to relatively inferior inter-stage mode-matching.

Both single-stage Green function separability, and inter-stage mode matching improve asymptotically with increasing ζ, providing for corresponding gains in selectivity (Fig. 45). Larger ζ also implies a decrease in temporal skewness of the Schmidt modes relative to the pump shapes. The exact mode matching in

RC configuration results in matching skewness directions for input and output Schmidt modes of a single band, a feature that is not present for DC configuration (Fig. 46). Therefore, unconverted higher-order Schmidt modes of the RC process undergo no temporal distortion upon passing through the TMI transformation. This allows TWM-TMI devices operating in the RC configuration to be used in a chained sequence to implement multiple operations on the temporal-mode basis.

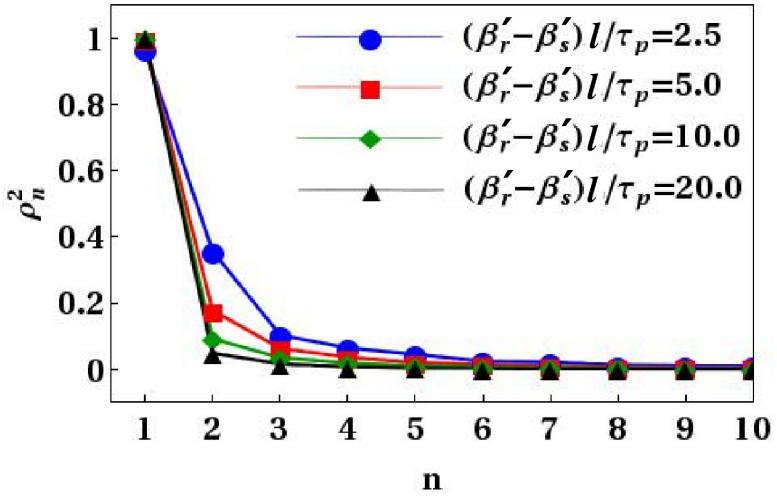

FIGURE 45. Dominant Schmidt mode conversion efficiencies for TWM-TMI in the RC configuration, illustrating asymptotic improvement in selectivity with decreasing pump-pulse width τ_p relative to interaction time $|\beta_{rs}'|l$. Reproduced from [42].

TMI can also be extended to arbitrarily large number of stages in both RC and DC configurations. Since the single-stage Green functions are more separable at lower conversion efficiencies, increasing the number of stages can increase selectivity. Multistage implementations will use lower pump powers due to the increase in the number of inter-pulse interactions. For optimal selectivity when using an N-stage process, the conversion efficiency for the first stage should be approximately $0.5[1 - \cos(\pi/N)]$. The expression is the exact splitting ratio necessary for a sequence of N nonpolarizing beam splitters to interferometrically

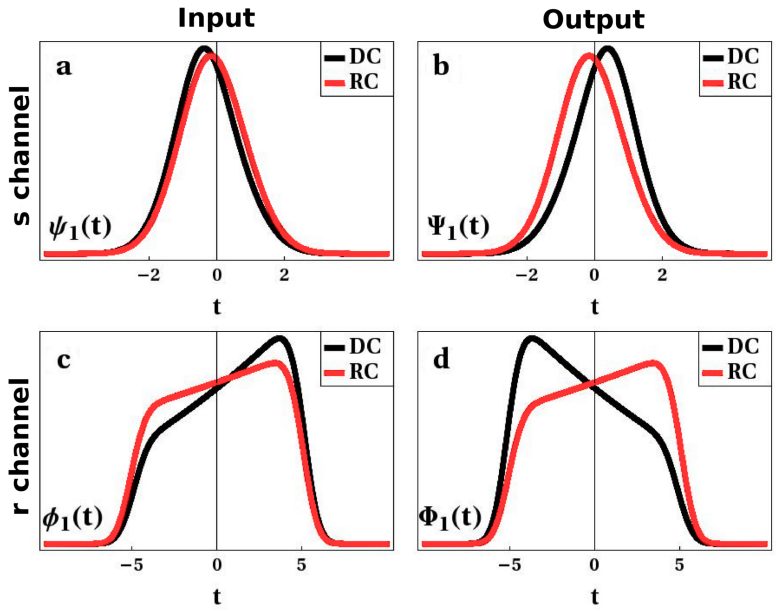

FIGURE 46. (a) s-input, (b) s-output, (c) r-input, and (d) r-output bands for both DC (black) and RC (red, lighter shade) configurations of a two-stage TMI implemented using TWM with a single Gaussian pump, and $|\beta'_{rs}|l/\tau_p = 10$. Values of t are relative to a $|\beta'_{rs}|l$ of 10. Reproduced from [42].

change the propagation direction of an incident beam of coherent light, and becomes more accurate for TMI for larger N. Figure 47 shows the ratio of converted-to-total energy of the first Schmidt mode versus propagation distance for various number of stages. The plots tend to asymptotically converge to a sinusoidal curve. A four-stage scheme yielded DC and RC selectivities of 0.9977 and 0.9978 respectively. The corresponding ten-stage selectivities are 0.99996 and 0.99997. Increasing the number of stages also decreases the temporal skewness of the first Schmidt mode relative to the corresponding pump-shape. The directionality of skewness for N-stage TWM-TMI in the DC configuration is independent of N. However, for N-stage TWM-TMI in the RC configuration, one can choose between distortionless FC and distortionless unconverted transmission of pulses by choosing odd or even N respectively.

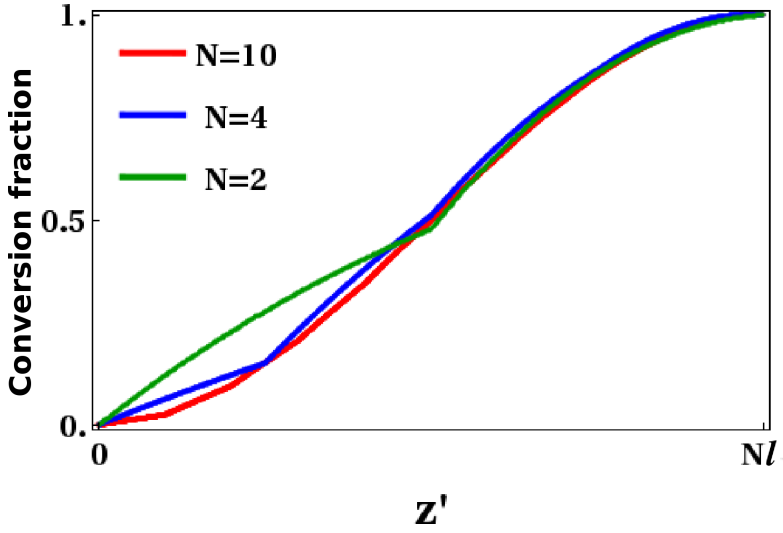

FIGURE 47. Multistage TWM implementation of TMI, showing the ratio of converted to total energy of the first Schmidt mode versus z' (propagation distance). N is the number of stages and l is the medium length for each stage. Reproduced from [42].

Quesada *et al.* [93] have formalized this argument in terms of a Magnus expansion of the frequency-converision unitary operator. The interaction Hamiltonian for three-wave mixing with a strong pump field can be expressed as

$$\hat{H}_I(t) \propto \gamma \int d\omega_p d\omega_s d\omega_r e^{i\Delta\omega t} \Lambda(L, \omega_r, \omega_r, \omega_p) \tilde{A}_p(\omega_p) \hat{a}_s(\omega_s) \hat{a}_r^\dagger(\omega_r) + \text{H.c.} \quad (4.69)$$

where $\Lambda(L, \omega_r, \omega_r, \omega_p)$ is the phase-matching function, and $\Delta\omega = \omega_r - \omega_s - \omega_p$. The chief barrier for achieving high selectivity in single-stage schemes is a time-ordering effect: $[\hat{H}_I(t), \hat{H}_I(t')] \neq 0$. The net unitary transformation $(\hat{U}_{\text{FC}}(\gamma))$ however, may be subject to a Magnus expansion

$$\hat{U}_{\mathrm{FC}}(\gamma) = \mathcal{T} \exp\left[-\frac{i}{\hbar}\int_{-\infty}^{\infty} dt \hat{H}_I(t)\right] = \exp[\hat{\Omega}_1 + \hat{\Omega}_2 + \hat{\Omega}_3 + ...], \tag{4.70}$$

where $\mathcal{T}$ is the time-ordering operator. The Magnus expansion is unitary at all truncation orders. The n^{th} Magnus term $\hat{\Omega}_n$ scales as γ^n. If we were to perform FC in N steps, we would use a pump pulse with energy that is smaller by a factor $1/N^2$ (i.e. $\gamma \to \gamma/N$), since the pulses reinteract N times. The effective unitary operator becomes

$$\left(\hat{U}_{textFC}\left(\frac{\gamma}{N}\right)\right)^N = \exp\left[\hat{\Omega}_1 + \frac{\hat{\Omega}_2}{N} + \frac{\hat{\Omega}_3}{N^2} + ...\right]. \tag{4.71}$$

Quesada *et al.* [93] have shown that the lowest-order term $\hat{\Omega}_1$ lacks the time-ordering corrections, and hence gets enhanced relative to the others in multistage schemes. Therefore, if the GF started in a separable perturbative form at low conversion (meaning a good parameter regime), then multistage schemes can retain that feature by suppressing time-ordering effects.

Four-Wave Mixing

As mentioned in Chapter III, third-order ($\chi^{(3)}$) nonlinearity has also been used to perform quantum frequency conversion [68, 79]. This involves four optical fields, and is typically performed in silica fibers and Si_3N_4 waveguides. Figure 48 shows a schematic representation of QFC via four-wave mixing (FWM). There are two strong pump fields, which together form a traveling refractive-index Bragg grating in the medium, which the weak signal-idler fields then interact with. Hence, this method is also known as Bragg scattering (BS). This method has

proven highly useful for performing FC over small, tunable frequency shifts relative to what is typical of TWM.

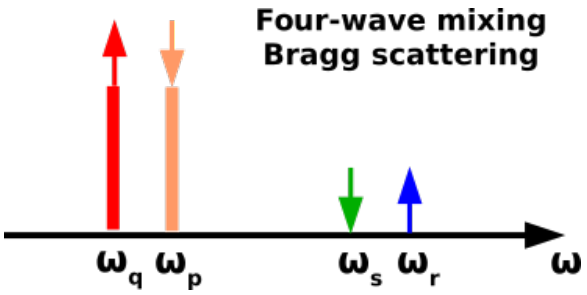

FIGURE 48. Schematic of Bragg-scattering via four-wave mixing on the frequency axis. The pumps centered at ω_p and ω_q are considered strong and nondepleting.

The energy and phase-matching conditions for BS are $\omega_p - \omega_q = \omega_r - \omega_s$, and $k_p - k_q = k_r - k_s$. No quasi-phase matching or periodic poling of any sort is required (or even possible) for $\chi^{(3)}$-nonlinear processes. The equations of motion are slightly more complex than those for TWM, due to self-phase and cross-phase modulation from the strong pump fields,

$$(\partial_z + \beta_p'\partial_t)A_p(z,t) = i(\gamma/2)\left[|A_p(z,t)|^2 + 2\,|A_q(z,t)|^2\right]A_p(z,t), \tag{4.72}$$

$$(\partial_z + \beta_q'\partial_t)A_q(z,t) = i(\gamma/2)\left[2\,|A_p(z,t)|^2 + |A_q(z,t)|^2\right]A_q(z,t), \tag{4.73}$$

$$\begin{aligned}(\partial_z + \beta_r'\partial_t)A_r(z,t) &= i\gamma A_p(z,t)A_q^*(z,t)A_s(z,t)\\ &\quad + i\gamma\left[|A_p(z,t)|^2 + |A_q(z,t)|^2\right]A_r(z,t),\end{aligned} \tag{4.74}$$

$$\begin{aligned}(\partial_z + \beta_s'\partial_t)A_s(z,t) &= i\gamma A_p^*(z,t)A_q(z,t)A_r(z,t)\\ &\quad + i\gamma\left[|A_p(z,t)|^2 + |A_q(z,t)|^2\right]A_s(z,t),\end{aligned} \tag{4.75}$$

where the coupling coefficient γ is proportional to the $\chi^{(3)}$-nonlinearity, as well as the square-root of the product of the pump pulse energies. For good TM

selectivity, we additionally require that each pump is group-velocity matched to its BS partner field, i.e. $\beta'_p = \beta'_s$ and $\beta'_q = \beta'_r$.

For TMI using FWM, the $\chi^{(3)}$ medium being used in each stage must be long enough for complete inter-pump-pulse collision to occur. This is straightforward to satisfy with the use of highly-nonlinear optical fibers (Fig. 49). For Gaussian pumps of temporal widths of the order of 10 ps, and wavelengths at 800 nm and 850 nm, a typical highly-nonlinear photonic crystal fiber will need to be about 20 m long for complete collision ($|\beta'_r - \beta'_s|l/(\tau_p + \tau_q) = 5$).

The presence of two pumps enables independent shaping of the Schmidt modes of both bands in FWM-TMI (see Fig. 50). However, nonlinear phase modulation severely affects the Schmidt-mode phase-profiles, and restricts FWM-TMI to the RC configuration. This is a result of the well-known cross- and self-phase modulation present in any $\chi^{(3)}$ medium. To overcome this impairment, the pumps must be pre-chirped with specific phase-profiles [94] for each stage to enhance inter-stage mode-matching. The starting phase profiles of the pumps p and q in stage-ξ need to be

$$\begin{aligned}
\alpha_p^{(\xi)}(t) &= -2\overline{\gamma}^{(\xi)} \int_{-\infty}^{t} ds \left[|\overline{A_q}(s)|^2 - |\overline{A_p}(s)|^2 \right] \\
&\quad - \frac{3}{2}\overline{\gamma}^{(\xi)} |\overline{A_p}(t)|^2 t + \frac{3}{2}\overline{\gamma}^{(\xi)} |\overline{A_q}(0)|^2 t + (\epsilon_p - \delta_{\xi,2})\gamma l |\overline{A_p}(t)|^2, \qquad (4.76) \\
\alpha_q^{(\xi)}(t) &= -2\overline{\gamma}^{(\xi)} \int_{-\infty}^{t} ds \left[|\overline{A_q}(s)|^2 - |\overline{A_p}(s)|^2 \right] \\
&\quad + \frac{3}{2}\overline{\gamma}^{(\xi)} |\overline{A_q}(t)|^2 t - \frac{3}{2}\overline{\gamma}^{(\xi)} |\overline{A_p}(0)|^2 t + (\epsilon_q - \delta_{\xi,2})\gamma l |\overline{A_q}(t)|^2, \qquad (4.77)
\end{aligned}$$

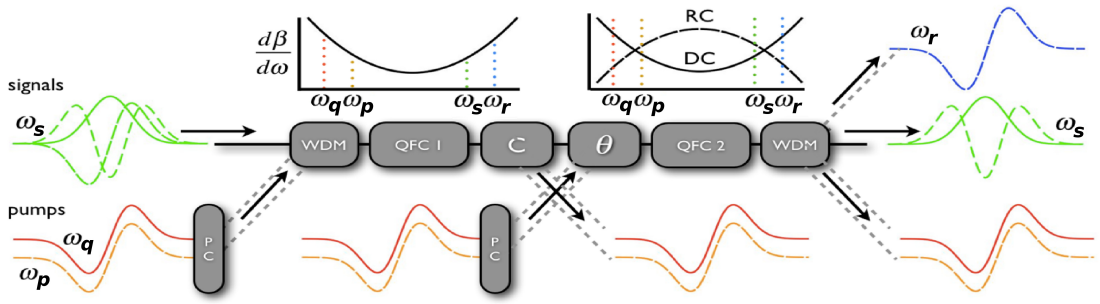

FIGURE 49. Temporal-mode interferometer using two nonlinear media (QFC 1 and QFC 2) with identical (DC) or opposite-sign (RC) dispersion. Appropriate choices for pump-pulse shapes, pump powers and the phase shift θ will selectively frequency convert a specific s (green, ω_s) TM into an r (blue, ω_r) TM at a different central frequency, whilst not affecting temporally-orthogonal s-input TMs. WDM stands for wavelength-division multiplexer. PC stands for pre-chirp modules, which are necessary for $\chi^{(3)}$ implementations. The coupler C contains frequency dependent delays for the DC case. Reproduced from [42].

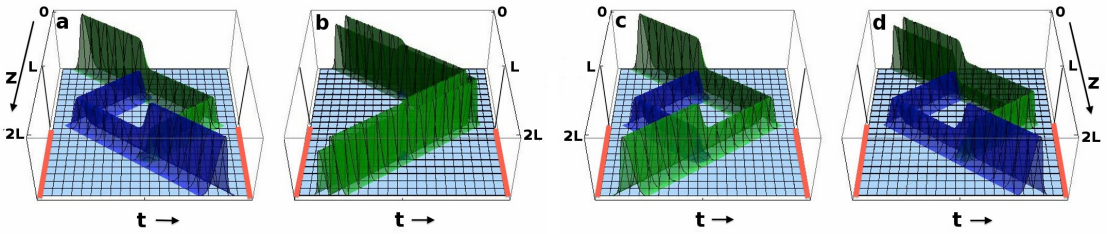

FIGURE 50. Temporal-mode interferometery with the two interferometer 'arms' being the frequency bands s (green, lighter shade) and r (blue, darker shade), undergoing two complete collisions in the two fibers and exchanging energy. This visualization plots the color-coded signal-field intensities in the average velocity frame with populated green input and empty blue input at $z = 0$, for the RC configuration found by numerical solution of the equations of motion. (a) Both pumps are Gaussian, and the first Schmidt-mode green-to-blue conversion is nearly 100% at phase-shift $\theta = 0$. (b) Both pumps are Gaussian, and the second Schmidt-mode conversion is nearly 0%. (c) Both pumps are Gaussian, and the first Schmidt-mode conversion efficiency is suppressed to zero at phase-shift $\theta = \pi$. (d) Pump q is Gaussian, and the shape of pump p is tailored to convert the green input mode from (b) into a Gaussian-like blue output with nearly 100% efficiency at $\theta = 0$. Reproduced from [42].

where $\overline{\gamma}^{(\xi)} = \gamma/(\beta_r'^{(\xi)} - \beta_s'^{(\xi)})$, and $\overline{A_j}(t) \equiv A_j(0,t)$. The limits of the integration terms are valid only for complete pump collisions. It must be noted that the pump phase profiles contain a term each that is fully linear in time, which are equivalent

to frequency shifts. These are an approximate compensation for a non-separable part of the phase profile of the GF kernels [94] which only attains significant magnitude away from the centroids of the GF-kernel amplitude functions. The slope of this term for each pump is proportional to the magnitude-square of the amplitude of the other pump's envelope. The slope is also proportional to $\overline{\gamma}^{(\xi)}$, whose denominator changes sign between the two stages. For a given set of chirp parameters, a pump will require frequency shifts of opposite signs in the two stages. Figure 51 shows the plots of the pump phase profiles from Eqs. 4.76 and 4.77 for three sets of chirp parameter values. Figure 53 shows the amplitudes and phase profiles of the first input and first output Schmidt modes for both stages of FWM-TMI in the RC configuration for the same three sets of chirp parameter values.

The chirp parameters ϵ_p and ϵ_q can be any real values. However, for FWM-TMI in the RC configuration to be useful, one will have to pick specific values to make the desired band input/output Schmidt mode have a flat phase profile. For example, Fig. 52 shows the Schmidt-mode amplitudes, and phases corresponding to FWM-TMI with selectivity 0.9873 ($|\rho_1|^2 = 0.9973$, $|\rho_2|^2 = 0.0082$). The pump pre-chirps (Fig. 51(c, d)) were specifically chosen to yield flat phase profiles for the r-output (Fig. 52(f)) and s-input (Fig. 52(g)) Schmidt modes. Namely, $\epsilon_p = 2$ and $\epsilon_q = 0$. The results were computed for $|\beta'_r - \beta'_s|l/(\tau_p + \tau_q) = 5$.

FWM-TMI can in principle be extended to multiple stages, provided that every stage-interface is in the RC configuration. The pump frequency shift will alternate in sign for every stage in sequence. The pump chirp profile functions in Eq. 4.77 will likewise need to be generalized for arbitrary number of stages. The

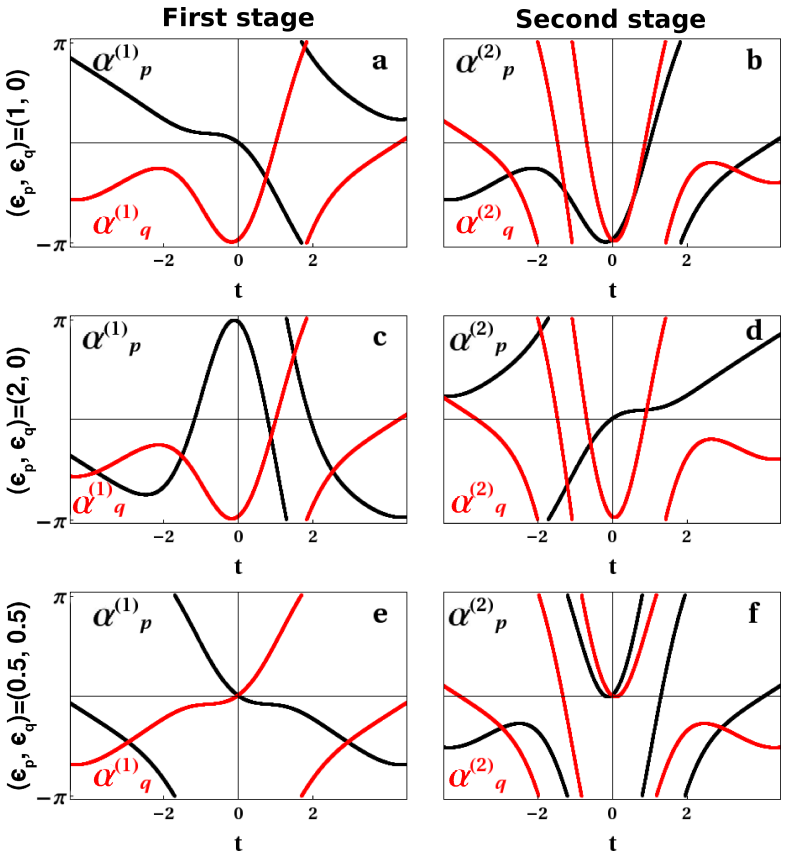

FIGURE 51. The first-stage (a, c, e) and second-stage (b, d, f) pump chirps used to derive the three inter-stage mode-matched Schmid-mode phase profiles shown in Fig. 53. The chirp-parameters $\{\epsilon_p, \epsilon_q\}$ are $\{1, 0\}$ in (a, b) , $\{2, 0\}$ in (c, d) , and $\{0.5, 0.5\}$ in (e, f). Values of t are relative to a $|\beta'_r - \beta'_s|l$ of 10. Reproduced from [42].

Kronecker-$\delta_{\xi,2}$ term will pick up a factor inversely proportional to the number of stages.

The need for pump-phase chirps in FWM-TMI can be circumvented if one resorts to asymmetrically-pumped Bragg scattering [43, 95], in which one of the pumps (say pump-p) is made very long or quasi-continuous wave (CW), and the shorter pump power is relatively weak. The equations of motion (with spatio-temporal arguments suppressed) reduce to

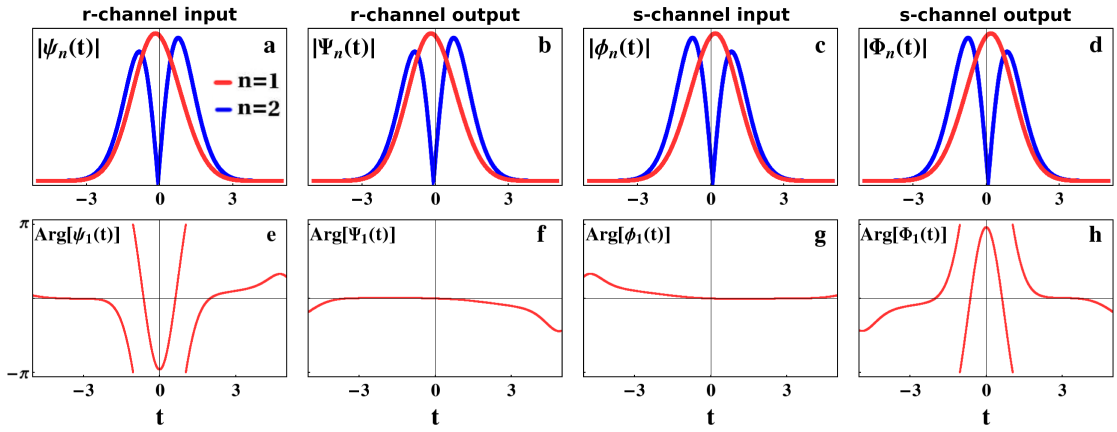

FIGURE 52. The first two Schmidt modes (a, b, c, d), and first Schmidt-mode phase profiles (e, f, g, h) for FWM-TMI in the RC configuration with Gaussian pumps. The first two Schmidt modes are shown for r-input (a), r-output (b), s-input (c), and s-output (d). Pump pre-chirp parameters used were $\epsilon_p = 2$, $\epsilon_q = 0$. The selectivity was 0.9873. Values of t are relative to a $|\beta_r' - \beta_s'|l$ of 10. Reproduced from [42].

$$\partial_z A_p = i\gamma |A_p|^2 A_p/2, \quad (\partial_z + \beta_q' \partial_t) A_q = i\gamma |A_p|^2 A_q, \tag{4.78}$$

$$(\partial_z + \beta_s' \partial_t) A_s = i\gamma |A_p|^2 A_s + i\gamma A_p^* A_q A_r, \tag{4.79}$$

$$(\partial_z + \beta_r' \partial_t) A_r = i\gamma |A_p|^2 A_r + i\gamma A_p A_q^* A_s. \tag{4.80}$$

The pump solutions are $A_p(z) = P_p \exp(i\gamma P_p z/2)$ and $A_q(z,t) = a_q(t - \beta_q' z) \exp(i\gamma P_p z)$. All self- and cross-phase modulation effects occur only due to the long CW pump, which is equivalent to pump-power-dependent frequency and wavenumber shifts of the signals. This method can simulate TWM-like dynamics in a $\chi^{(3)}$ medium, and by extension, can be used to implement TWM-TMI using FWM. The choice of which pump is to be made CW does not affect the selectivity, making asymmetrically pumped Bragg scattering a valuable option [43].

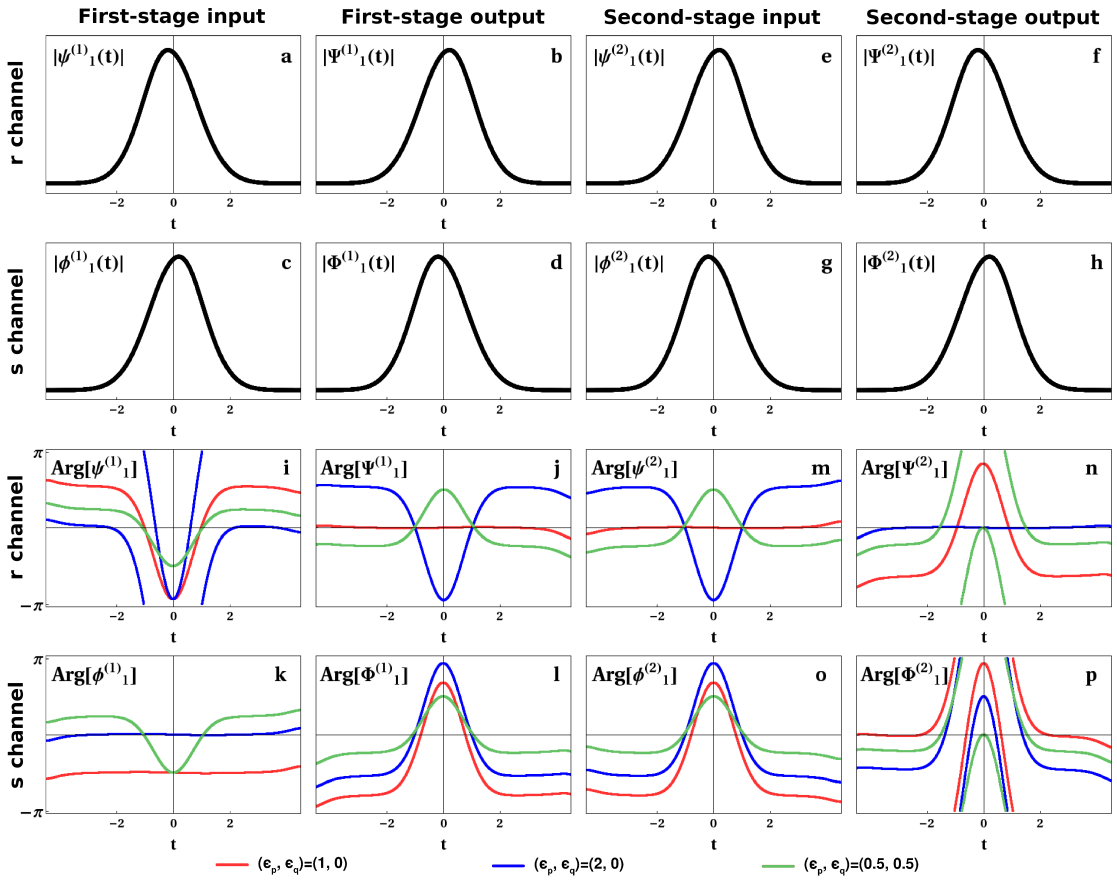

FIGURE 53. The dominant input (a, c, e, g) and output (b, d, f, h) Schmidt modes for the first-(a, b, c, d) and second-(e, f, g, h) stages for both r (a, b, e, f) and s (c, d, g, h) bands for RC configuration of FWM-TMI for a Gaussian-shaped pumps, and complete pump collisions ($|\beta'_r - \beta'_s|l/(\tau_p + \tau_q) = 5$). Also shown are the corresponding Schmidt mode phase profiles (i-p) for three seperate choices of pump chirps for the two stages. Due to pump-induced self- and cross-phase modulation, the second-stage pump chirps have to be related to the first-stage pump chirps in the manner specified in Eq. 4.77 for good inter-stage mode-matching between (b, d, j, l) and (e, g, m, o) respectively. The complete two-stage composite system Schmidt modes for FWM-TMI in the RC configuration are plotted in Fig. 52. Values of t are relative to a $|\beta'_r - \beta'_s|l$ of 10. Reproduced from [42].

CHAPTER V

EXPERIMENT DESIGN AND RESULTS

This chapter contains published co-authored material from [44]. This paper was co-authored by me with my advisor. I was responsible for the design and construction of the experimental setup, the drafting of the paper, the measurements, and the presentation of the data therein. I fully acknowledge the role of my advisor Prof. Michael G. Raymer in this publication.

Waveguide and Wavelength Selection

We can condense all of the system parameters into three dimensionless quantities in order to aid mapping settings and results from diverse FC systems to the model. These are [40]

$$\widetilde{\gamma} = \gamma\sqrt{\frac{L}{\beta'_{rs}}}, \quad \zeta = \frac{\beta'_{rs}L}{\tau_p}, \quad \text{and} \quad \xi = \frac{\beta'_{pr}}{\beta'_{ps}}, \tag{5.1}$$

where τ_p is the temporal-width of the pump pulse, and $\beta'_{jk} = \beta'_j - \beta'_k$. $\widetilde{\gamma}$ is an interband coupling strength. ζ is the signal-idler inter-pulse walk-off relative to pump width, and ξ is the group-velocity mismatch contrast.

Through an exhaustive numerical exploration presented in Chapter IV [40], I have previously determined that for good GF separability for single-stage FC at low pump energies, as well as the best selectivity (~ 0.83) at higher pump energies, the best parameter regime is $\xi \gg \zeta \gg 1$ (see universality curve in Fig. 36). By designing the system such that the group-velocity of the pump pulse is identical to that of one of the other bands (the s-band, for the definitions in Eq. (5.1)),

and highly different from that of the remaining (r) band, we can have $\xi \to \infty$. I have called this condition the group-velocity matched (GVM) regime [30]. The magnitude of ζ is limited by the maximum fabricable length of the nonlinear waveguide, and the requirement that the pump pulse be reasonably narrowband (giving a lower bound on temporal width) to avoid higher-order dispersion.

The GVM or near-GVM condition ($\xi \gg \zeta \gg 1$) must constrain the selection of waveguide material, length, band central frequencies, and TM bandwidths. At the time of this writing, only two other groups [71, 72, 80, 96] have addressed experimental frequency conversion in a TM-selective context. The Silberhorn group [71, 72, 96] use homebuilt, periodically-poled lithium niobate (PPLN) waveguides with a poling period of about 4.4 μm. Such a period gives the optimum phase-matching for sum frequency generation (SFG) from bands centered near 1550 nm and 860 nm, into the band around 550 nm. They engineer their waveguide dispersion to achieve perfect GVM ($\xi \to \infty$) at these wavelengths, and compensate for fabrication errors by tuning the waveguide temperature in the $150 - 200$°C range. They can thus afford to use longer waveguides ($\sim 17 - 27$ mm) and short pulse lengths (~ 200 fs) and obtain large ζ values without having to worry about signal-pump inter-pulse walkoff within the medium during propagation.

Although exact GVM is optimum for TM-selectivity, one can deviate from perfect signal-pump GVM and still retain most of its advantages, as long as $\xi \gg \zeta \gg 1$ is satistied. The Kumar/Kanter group [80] hit upon an interesting solution that allows for minor deviation from GVM. This exploits the narrow phasematching bandwidth of the upconverted field in most second-harmonic generation waveguides, which has been used to attempt highly separable (but not highly "selective") non-pumped field-orthognal CDMA style TM sorter around

2001 [97, 98]. The Kumar/Kanter group used a 52 mm long, custom PPLN waveguide designed for second-harmonic generation (SHG) from 1544 nm into 772 nm at 73.4°C, and situated their pump (1556.6 nm) and signal (1532.1 nm) bands symmetrically on either side of the SHG wavelength, yielding $\xi \approx 215$. Their pump/signal sources and pulse shapers restricted their temporal widths to around 5 ps, implying $\zeta \approx 3$. The theory predicts [40, 43] that their selectivity would improve significantly with larger pump/signal bandwidths, as I have used here.

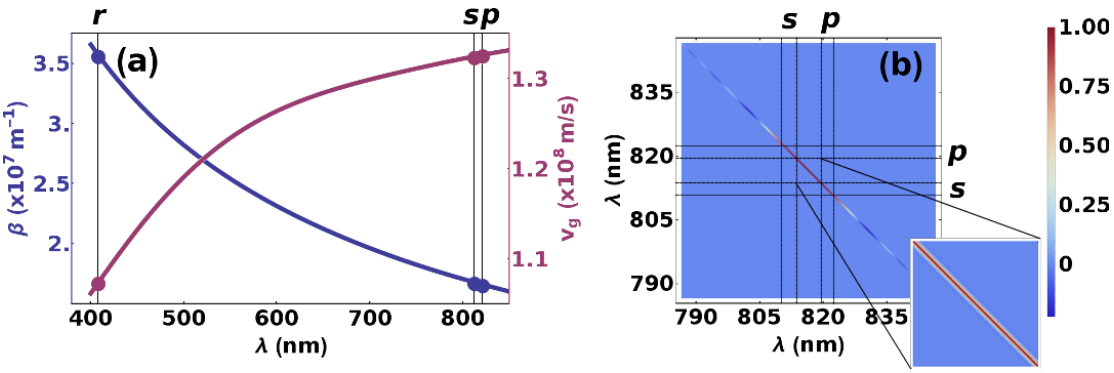

FIGURE 54. (a) The wavenumber (β) and the group velocity ($v_g = d\omega/d\beta$) vs. wavelength (λ) for a typical 5 μm wide, periodically-poled, MgO:LN waveguide. Also shown are the r-, s-, and $p-$ bands that I utilize for SFG. (b) Numerically computed, peak normalized joint-spectral amplitude of the degenerate, Type-0 SPDC photon pairs that would be generated in 5 mm of such a waveguide when pumped with 0.1 nm wide blue light in the r-band. Also shown are the signal (s) and pump (p) bands for the SFG process, which are situated symmetrically on either side of the red second-harmonic generation pump wavelength at 816.6 nm. Due to the frequency anti-correlatedness of the SPDC joint-spectral amplitude, both s- and p-bands need to contain non-zero optical energies for SFG to occur into the r-band. Reproduced from [44].

I also employ an SHG waveguide (816.6 nm to 408.3 nm at 24.25°C) for FC by situating the signal and pump bands on either side of the red SHG pump band. Typical SHG acceptance bandwidths are very narrow. As long as the FC-pump band is sufficiently detuned from the SHG-pump wavelength,

so as to avoid pump-only spurious blue-light generation, the relative spectral flatness of normal dispersion ensures near-GVM conditions [see Fig. 54(a)]. One must choose a temporal width that is small enough to ensure $\zeta \gg 1$ (for large idler-pump walkoff), but wide enough to ensure that the pump-signal inter-pulse walkoff within the medium remains a small fraction of the total pulse widths ($\xi \gg \zeta$). SHG waveguides, when pumped at the sum frequency can generate degenerate photon-pairs via spontaneous parametric down conversion (SPDC). The joint-spectral amplitude of the pairs are tightly anticorrelated in [Fig. 54(b)], reflecting the narrowness of the SHG red-pump acceptance band [99]. But the individual photons of the pair would be wideband, allowing for sum frequency generation from two highly detuned frequency bands on either side of the SHG-pump wavelength. Here, SFG is really a band-restricted inverse of SPDC. This behavior makes off-the-shelf waveguides suitable for TM-selective FC experiments.

Our group acquired a 24 mm MgO-doped PPLN wafer from the company AdvR, which was poled to perform Type-0 SHG (all fields co-polarized) from NIR to blue wavelengths. The wafer was composed of 4 identical groups of 6 waveguides each, with increasing transverse widths 3, 4, 5, 6, 7, and 8 μm in each group. The waveguides were etched on the top surface, and their effective depth was 5 μm. I chose to work with the 5 μm wide waveguide within the wafer as I found its phasematching wavelength at near-room temperature to be optimal. I had the wafer cut down in length to 5 mm to better satisfy the near-GVM conditions, as the pump-signal walkoff would have otherwise been too large for our pulse widths. I used a waveguide oven and a PID temperature control circuit, that were designed and built at the University of Oregon Machine shop by Cliff Dax and Jeffrey Garman. The temperature controller had an accuracy of ± 0.01 °C.

Ultrafast Laser

Once the waveguide had been selected, I required shape-manipulable pump and signal pulses at close by wavelengths (separated by 10-15 nm) that are synchronized in time. I decided to build an in-house ultrafast, Kerr-modelocked titanium-sapphire (Ti:sapph) laser with a wide bandwidth, and then carve out the pump and signal spectra from the laser spectrum.

Ti:sapph lasers consist of a Brewster-cut Ti:sapph crystal mounted in a cooling element (in our case, it was water cooled). A CW pump laser at a green color of 532 nm is focused onto the interior of the crystal. In our case, I used a 5 W Verdi diode-pumped Nd:YAG laser from the company named Coherent. This causes the crystal to flouresce in a wide range of near-IR wavelengths. Curved and flat, low-group-delay dispersion (GDD) mirrors are then mounted around the crystal to form a linear cavity for the near-IR flourescence. When the cavity is aligned to be resonant at one of the flourescence wavelengths, spontaneous emission at that wavelength will populate the cavity mode, which in turn causes further stimulated emission into the same cavity mode. The cavity builds up a substantial amount of power within it, and the laser is then said to be lasing. One of the end-mirrors of the linear cavity will have a small partial transmittance, allowing some coherent light to leak out in a beam. This is the laser beam that is used.

The setup described above would produce a CW Ti:sapph laser. In our laser, I used a pair of highly dispersive prisms to provide dispersion compensation for traversal through the crystal and reflection off of the mirrors. The net effect is to ensure that every wavelength travels through a slightly different path inside the

cavity, such that a wide range of wavelengths can be resonant with the cavity at once.

The Kerr ($\chi^{(3)}$) nonlinearity of the Ti:sapph crystal causes its effective refractive index to change depending on the intensity of the electric field of the mode traversing through it. At large enough intensities, this can result in a self-focusing effect, as the intense beam would create a lense within the crystal medium. This, in combination with the dispersion compensation prisms, can allow for a cavity configuration where ultrawide-band pulses with very large peak intensities can stably lase. Then, a small physical, perturbative shock applied to the body of the cavity (typically on the translation mounts of one of the prisms) will cause a CW laser to lase in pulsed mode, and is then said to be modelocked. The pulse rate is dictated by the round-trip time of the linear cavity, which in our case was 76 MHz. The pulse bandwidth can be tuned by placing two razor blades inside the cavity to form an acceptance slit. Moving the blades closer or farther apart can change the bandwidth, and translating them together tunes the central frequency. Figure 55 shows the spectrum of our ultrafast laser, as well as an energy transition diagram showcasing how different parts of the spectrum combine to produce SFG in the waveguide.

Pulse Shaper

The laser was made to lase with a bandwidth of 10-12 nm and centered at 821 nm. I then carved out our pump (centered at 821 nm) and signal (centered at 812.2 nm) from the laser spectrum using a Fourier-domain pulse shaper. The basic principle of Fourier-domain shaping is illustrated in the Treacy-grating pair [100] $4f$ system in Fig. 56. Ultrafast pulses are difficult to shape in the time

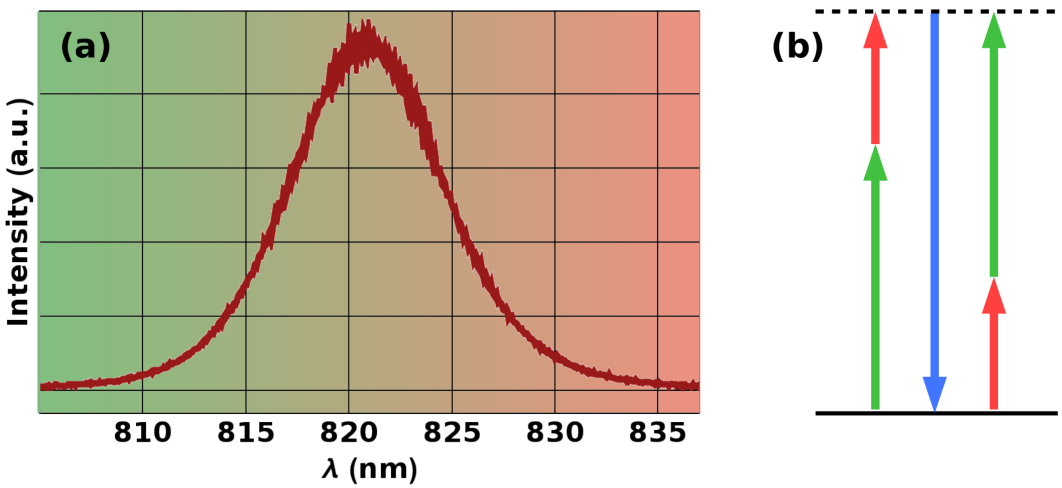

FIGURE 55. (a) Power spectrum of the in-house ultrafast, Kerr-lens modelocked Ti:Sapphire laser. The pulse repetition rate is 76 MHz. The color gradient in the background differentiates the long-wavelength "red" part of the spectrum from the shorter wavelength "green" part. (b) The energy transition diagram, showcasing how different parts of the laser spectrum combine to generate the narrowband SHG blue wavelength in the waveguide.

domain using electrically driven optical modulators. Therefore, it is simpler to spatially disperse their spectral components and modulate them individually and independently, before recombining them. The schematic shown in Fig. 56 consists of two identical diffraction gratings working in Littrow configuration. One of them disperses the frequency components of an incoming pulse, mapping them to different angles. This is governed by the standard blazed-grating equation,

$$d(\sin\alpha + \sin\beta) = \lambda, \tag{5.2}$$

where d is the line-spacing of the grating, α is the incident angle of the incoming beam, and β is the first-order diffraction angle. λ is the wavelength of the spectral component being considered. The Littrow condition is when $\alpha = \beta$. These are configured to work as close to Littrow mode as possible.

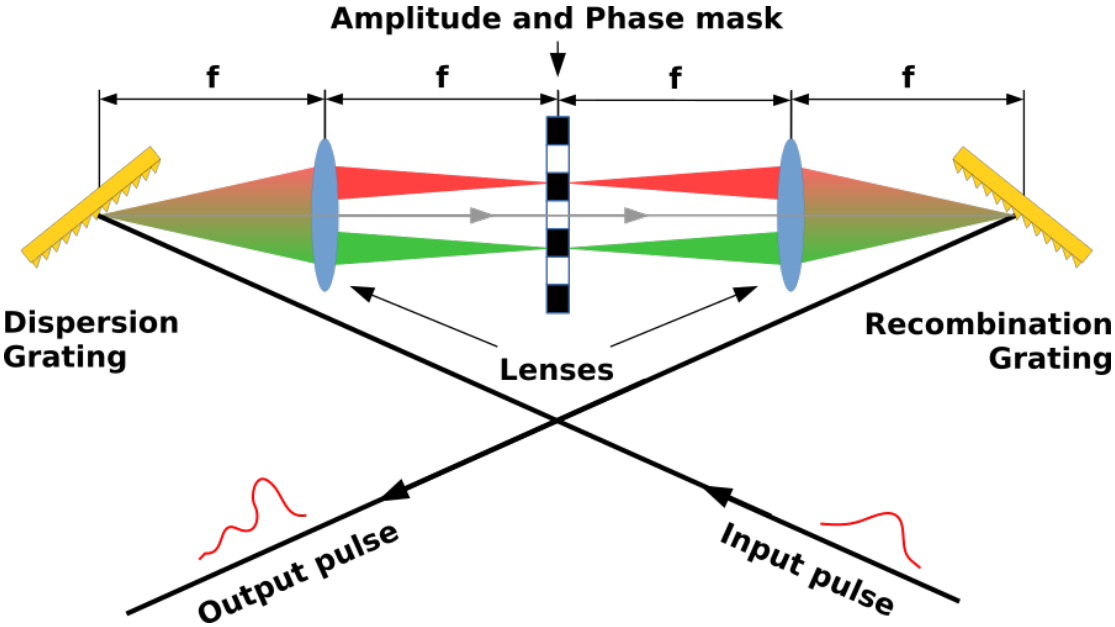

FIGURE 56. Treacy-grating-pair $4f$-configuration pulse shaper. f is the focal length of the lenses shown. The frequency components are color coded as a gradient from green-to-red, going from shorter to longer wavelengths. Only two disjoint frequency components are shown being focused onto the amplitude and phase masks at the Fourier plane of the lenses for the sake of clarity.

A lens placed at a focal distance away from the dispersive grating will then focus different frequencies to different spatial locations (determined by the angles of incidence onto the lens) on its Fourier plane. A combination of amplitude and phase modulation can be applied to the various frequency components at the Fourier plane before the entire setup is mirrored on the other side to recombine the spectrum into a temporal pulse.

If the spot size of a collimated wavelet at the grating were w_0, then the focused spot size at the Fourier plane would be $w_f = \lambda f/(\pi w_0)$. Therefore, even though the seperation between the focused spots of two given frequency components would increase linearly with the chosen focal length, so would the sizes of the spots. The focal length is chosen to make the spot size in the Fourier plane comparable (but not smaller than) the spatial resolution or pixel size of

the modulators. The incoming beam waist must also be large so as to apply the plane-wave approximation in calculating the grating's behavior, as hitting more lines of the grating is also beneficial for resolution.

Our ultrafast laser beam was spatially expanded to a transverse width of ~ 10 mm and sent into a folded, $4f$-configured Treacy-grating-pair [100] pulse shaper, which uses a reflective spatial-light modulator (SLM) in its Fourier plane (Fig. 57). The pulse shaper utilized a 1800 lines/mm holographic grating in near-Littrow mode, and a cylindrical lens of focal length 250 mm to focus the wavelets onto the SLM. The lens is cylindrical in order to spread the beam intensity vertically so as to avoid damaging the SLM. This gave us a horizontal spot size of ~ 30 μm for a given wavelength. I used a custom-made biprism to change the height of the forward and reflected light to keep the paths symmetric, whilst sacrificing exact normal incidence on the SLM pixels, whose specifications apply best for normal incidence.

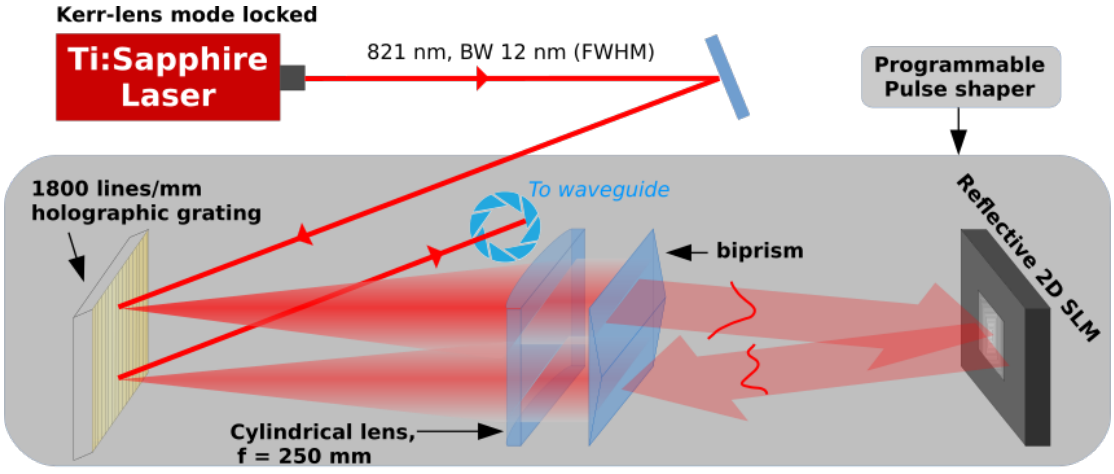

FIGURE 57. Folded Treacy-grating-pair pulse shaper. The holographic grating was used in near-Littrow mode for both incoming and outgoing beams. The $m = 1$ order reflection from two separated vertical blazed gratings rendered on the SLM was recombined on the holographic grating.

For the SLM, I used a Meadowlark 8-bit, 2D, phase-only liquid-crystal spatial light modulator of 1920 $\times$ 1152 pixel resolution and array size of 17.6 mm $\times$10.7 mm. The pixels were squares of size 9.2 μm and the fill factor was 95.7%. The spatial dispersion of the shaper at the SLM was 0.011 nm/pixel, although, the actual shaper resolution is limited by the spot size. In order to modulate both amplitude and phase, I used Silberberg group's [101] first-order approach, where I form a vertical blazed grating pattern on the SLM and pick off its $m = 1$ reflection as the output. Different phase ramps may be applied to different wavelengths (at different horizontal positions) to affect the amount of power in the $m = 1$ reflection, and the phases can be manipulated by vertically shifting the blazed grating upwards/downwards. I used a vertical period of 48 pixels in the pump band, and 50 pixels in the signal band, as shown in Fig. 58.

I therefore had a means of producing both pump and signal pulses from a common ultrafast laser pulse. These two frequency bands can be independently shaped, and can even be temporally delayed relative to each other by application of a linear phase ramp to their frequency spectra using the pulse shaper. This allows us to verify theoretical/model predictions for the FC process.

Single-Stage Setup and Measurements

Figure 59 shows the experimental setup for the single-stage measurements. I coupled light into and out of the waveguide using $f = 11$ mm aspheric lenses, which after some post-pulse-shaper beam resizing gave us a red-light coupling efficiency of about 30%. The blue and red beams were separated at the output by a Thorlabs DMLP650 longpass dichroic mirror, and the pump and signal bands

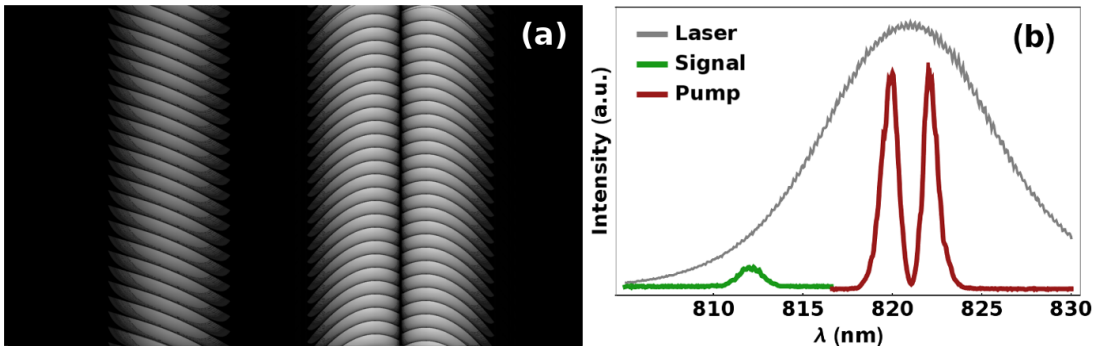

FIGURE 58. (a) Typical 8-bit grayscale phase mask applied to the SLM to generate a Gaussian shaped signal pulse (left band) and a first-order Hermite-Gaussian pump pulse (right band). Here, the horizontal coordinate maps to different wavelengths. The phase-contrast of the vertical gratings determines amplitude. Vertically shifting the gratings can affect phase (note relative shift between the two grating patterns generating the two frequency lobes of the pump). The curved pattern is for chirp compensation (measured using a commercial FROG/GRENOUILLE 8-50-USB), and the linear spectral phase on the signal (showing up as a horizontal tilt in the mask) shifts it in time relative to the pump. (b) Spectra of original Ti:Sapph laser, the signal, and the pump (first-order Hermite Gaussian, for example) generated by the SLM phase mask in (a). The three different spectra were captured under different conditions and hence, the relative heights are not to scale. Reproduced from [44].

in the red beam were split by angle-tuning two Semrock FF01-810/10 bandpass filters.

Although the SHG/SFG process for the phase-matched frequencies dominates when controlled for input powers, imperfections in the waveguide resulted in spurious SHG blue light at all "red" wavelengths. Figure 60 shows the blue light generated when Gaussian pump and signal pulses produced at the right central wavelengths were coupled into the chosen waveguide. There were two prominant blue peaks. The one at 408.3 nm, labeled "SFG peak" was narrower than the resolution of our UV spectrometer (0.1 nm), and was only present when both pump and signal pulses were present (and temporally overlapping). A second, broader blue peak at slightly longer wavelength could also be detected (labeled

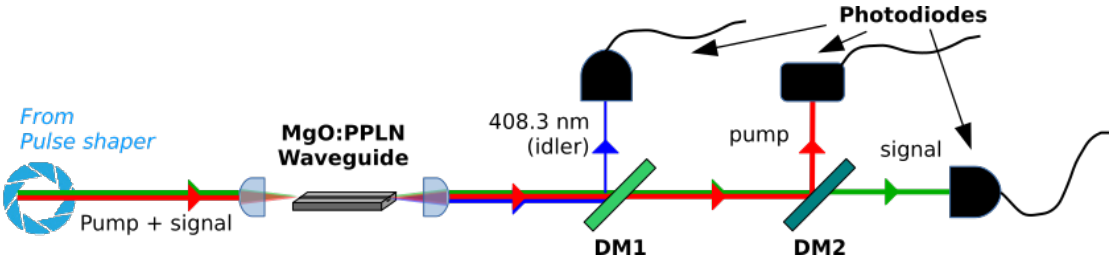

FIGURE 59. Single-stage experimental setup. Both the input and output couplers of the 5 μm wide, 5 mm long MgO:PPLN waveguide were single-element aspheric lenses of focal length $f = 11$ mm. DM stands for dichroic mirror. DM1 was a Thorlabs DMLP650 longpass dichroic mirror operating at 45° angle of incidence. DM2 was a Semrock FF01-810/10 bandpass filter operating at angle of incidence 12°. Some frequency filters are not shown.

"pump-only SHG" in the figure). This peak was independent of the signal pulse's presence. This spurious SHG peak was not strong enough to significantly deplete the pump, and was separated from the main peak using a Semrock TBP01-400/16 tunable bandpass filter at angle of incidence 14°. There was a spurious signal-only SHG peak to the shorter wavelength side, that could only be produced at large signal-band powers. I operated with very weak signals. As SHG scales with the square of its pump power, I could safely disregard the signal-only SHG process.

The choice of central wavelengths for the pump (821 nm) and the signal (812.2 nm) bands afforded us $\xi > 200$. The pump-pulse width was set by the pulse shaper to be ~ 530 fs, yielding $\zeta \approx 20$, landing us well within the near-GVM regime. The pulse shaper allowed us a sufficient range for time shifting the pump and signal pulses independently of each other. The average signal powers were chosen around $20 - 40$ μW (measured at waveguide output), which for a laser pulse rate of 76 MHz, translates to $0.26 - 0.53$ pJ per pulse. The pump power coupled into the waveguide was varied from 0 to ~ 3.5 mW (46 nJ per pulse), which was sufficient for significant CE [102] without much pump depletion via spurious SHG. In order to compare theoretical predictions with experimental data, I needed to map the

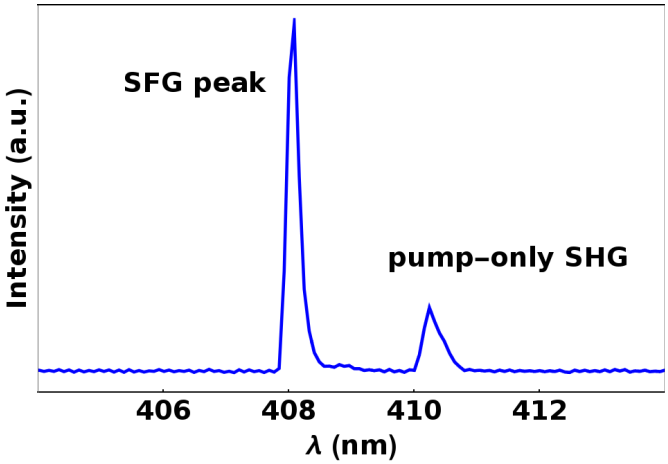

FIGURE 60. Blue light spectra generated from the waveguide in a typical run. The SFG peak requires both the pump and signal to be present at the input, whereas the pump-only SHG peak remains even without the signal, and occurs due to imperfections in poling. The latter peak can compete with the former at higher pump powers. To use very weak signals (say sub-single-photon level), very tight spectral filtering will be needed at the blue output arm. Reproduced from [44].

square-root of the pump power to $\widetilde{\gamma}$ through a proportionality factor σ. I fit all the diverse data for different input pulse-shape combinations and inter-pulse delays to a single σ value of $\sim 18\ /\sqrt{\mathrm{W}}$.

A quick means of verifying the model is to keep the signal input pulse shapes static, but delay them with respect to the pump pulse and chart the CE. For Gaussian and first-order Hermite-Gaussian pump and signal shapes, four surface plots of CE for various input inter-pump-signal delays (denoted by τ_d) and pump energies have been numerically generated and plotted in Fig. 61. The s-band Schmidt mode distortions show up as temporal shifts and lobe-peak asymmetries at higher $\widetilde{\gamma}$.

Figure 62 shows the conversion efficiencies recorded for Gaussian- and (first-order) Hermite-Gaussian-shaped pump and signal input pulses for various pump powers and initial pump-signal time delays (τ_d). The pump powers were changed

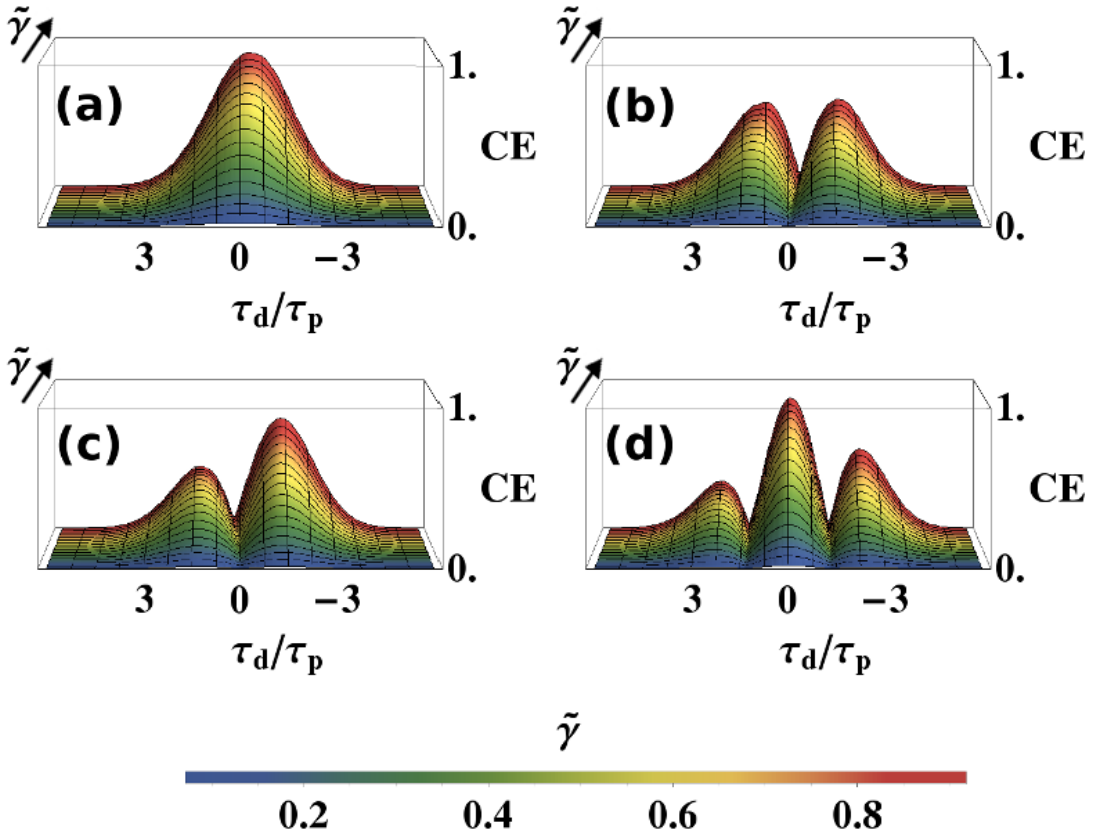

FIGURE 61. Numerically simulated, 3D surface plots of conversion efficiencies (CE) vs. input pump-signal time delay by pump width (τ_d/τ_p) for various $\tilde{\gamma}$ ($\propto \sqrt{P_{\text{pump}}}$) for (a) Gaussian pump and signal, (b) Gaussian pump and first-order Hermite-Gaussian signal, (c) first-order Hermite-Gaussian pump and Gaussian signal, and (d) first-order Hermite-Gaussian pump and signal pulse shapes. Note the temporal skewness at higher $\tilde{\gamma}$, reflected in shift of CE maxima with respect to mesh grid, as well as asymmetry in lobe peak heights. Reproduced from [44].

by changing the phase-contrast of the vertical gratings in the pump band on the SLM. The pump-signal time delay was scanned in steps of ~ 18.3 fs by applying a linear spectral phase ramp to the signal band on the SLM and changing its slope. The data reproduces the broad features predicted by theory in Fig. 61, namely, the temporal-shift (both extent and direction) of the peaks and troughs for the various shape combinations, as well as the numbers and relative heights of the peaks. This scan ensures that I wasn't seeing an artificial contrast in

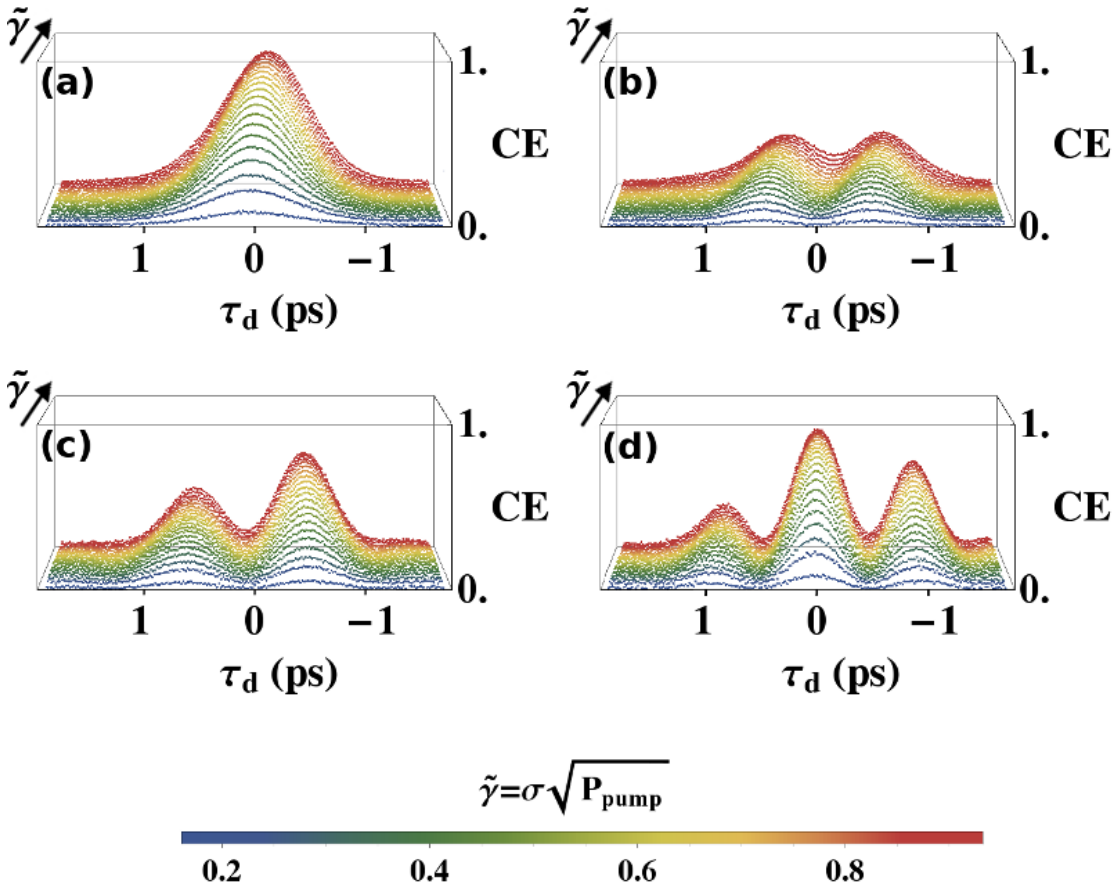

FIGURE 62. Experimental data: 3D point plots of conversion efficiencies (CE) vs. input pump-signal time delay (τ_d) for various $\widetilde{\gamma} = \sigma\sqrt{P_{\text{pump}}}$ (where $\sigma = 18$ $/\sqrt{W}$, and P_{pump} is average pump power) for (a) Gaussian pump and signal, (b) Gaussian pump and first-order Hermite-Gaussian signal, (c) first-order Hermite-Gaussian pump and Gaussian signal, and (d) first-order Hermite-Gaussian pump and signal pulse shapes. Note the temporal skewness at higher $\widetilde{\gamma}$, as well as asymmetry in lobe peak heights, matching the theoretically predicted trends from Fig. 61. Vertical error bars are all of order 10^{-3}, not shown. Reproduced from [44].

CE between pump-signal shape-matched vs. shape-mismatched cases owing to a setting dependent, systemically applied, extreme time delay between the pump and signal input pulses. The vertical error bars are all of order 10^{-3}, and are not shown for the sake of clarity.

For closer comparison, I take a $\tau_d = 0$ slice of the theoretical graphs and the measured data from Figs. 61 and 62 respectively, and plot them in Fig. 63. Note that the four possible input shape configurations follow the expected contrasts in CE. The data points for the first-order Hermite-Gaussian-shaped pumps are shifted horizontally forward relative to those for the Gaussian-shaped pumps. This is because for a given temporal-width scale, the first-order Hermite Gaussian spectrum has a slightly larger bandwidth, giving us more available power to be syphoned off from the ultrafast seed laser. Also note that for a given pump shape, the signal-shape matched points are shifted horizontally slightly backward relative to the signal-shape mismatched points, and the shift is larger at higher CE. This is because, due to energy conservation, some amount of power from the pump pulse is lost along with depletion of signal power during FC. The effect, a violation of the undepleting pump approximation, is negligible for weak signals, as demonstrated by the close match of the data with theory.

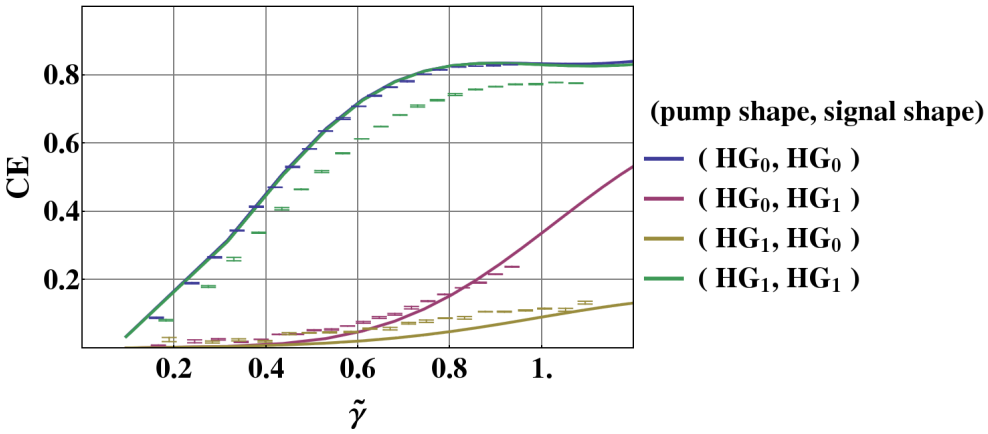

FIGURE 63. CE (conversion efficiency) vs. $\tilde{\gamma}$ ($\propto \sqrt{P_{\text{pump}}}$) for various pump and signal input pulse shapes at "zero" delay (defined as delay that maximizes CE at low pump power). The legend label (HG$_j$, HG$_k$) denotes j-th order Hermite-Gaussian pump pulse, and k-th order Hermite-Gaussian signal pulse. The solid lines are theory and the markers are measurements. Reproduced from [44].

In Fig. 64 I show the CE vs. $\widetilde{\gamma}$ for our attempt to match the exact, first input Schmidt mode at every $\widetilde{\gamma}$ via numerically computed TM shapes. The plotted points are for Gaussian, and first-order Hermite-Gaussian pump pulses. The solid lines are the theoretical prediction. The CE with matched (appropriate to pump shape) Schmidt mode inputs exceeds those of the pure Hermite-Gaussian-shaped signal inputs from Fig. 63. The measured data falls short of theory at larger pump powers. I suspect this is due to pump pulse reshaping within the waveguide due to spurious pump-only second-harmonic generation (see Fig. 60). Despite this, I achieved a CE contrast of 4.7 to 1 (85% vs. 18%) between the two pump shapes and their corresponding, first Schmidt modes. The error bars are of order 10^{-3}, and are not shown.

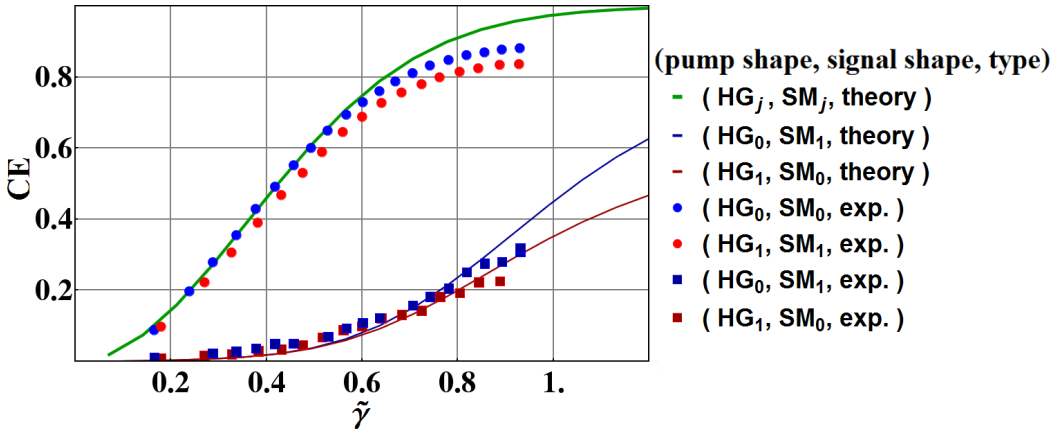

FIGURE 64. CE (conversion efficiency) vs. $\widetilde{\gamma}$ ($\propto \sqrt{P_{\text{pump}}}$) for j-th order Hermite-Gaussian pump pulses (HG_j) and the corresponding first input Schmidt modes (SM_j). Also shown are CE with the pump shapes swapped for $j \in \{0, 1\}$. Solid lines are theory, and markers are experiment (type: "exp."). Error bars (not shown) are of order 10^{-3}. Reproduced from [44].

Dual-Stage Setup and Measurements

In order to implement the two-stage scheme, we will not only need two nonlinear waveguides with precisely identical phasematching curves (identical dispersions, length, and poling period), but we also require phase coherence between the two pump pulses used. Figure 65 consists of a schematic diagram for two-color interferometry [81, 82]. In the experiment, all three are collinear and copolarized within the waveguide for both stages. The two stages are pumped by pulses derived from a single beam split using some beam splitter or equivalent, ensuring phase coherence across the entire device. If the phases acquired by the three bands inbetween the stages are denoted by $\Delta\phi_j$, where $j \in \{r, s, p\}$, then the net interferometric fringe phase is

$$\Delta\phi_{\text{net}} = \Delta\phi_p + \Delta\phi_s - \Delta\phi_r. \tag{5.3}$$

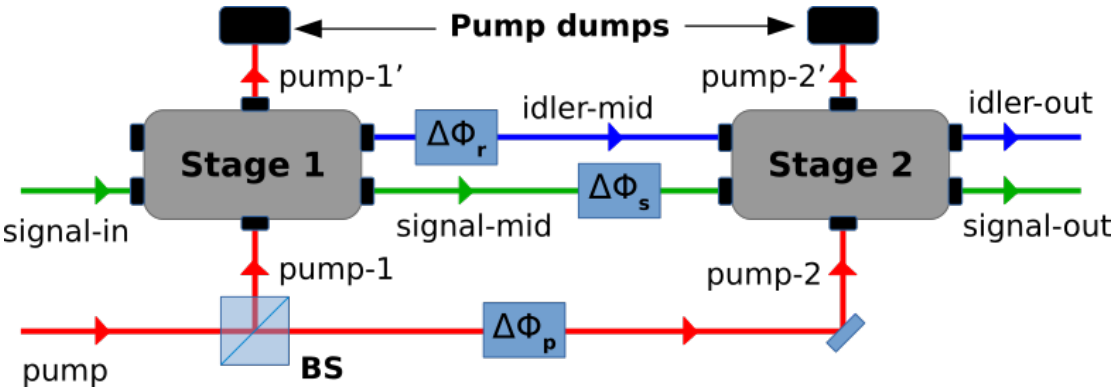

FIGURE 65. Schematic of two-color interferometry. The three frequency beams are spatially disjoint for the sake of clarity. The inter-stage phases of the three frequency bands are also shown. The beam labels (signal-in, idler-mid, etc.) are utilized again in Fig. 66.

In my setup, I will be varying this phase and measuring the interferometric fringe visibility by monitoring the conversion efficiency. But the coupling of beams

into both the stages is lossy (hence the need for two separate pump pulses, as I cannot reuse the full power of the pump pulse that exits stage one). One needs to balance the loss in both the colored arms of the interferometer to maximize visiblity. Harkening back to Eq. 2.47 from Chapter II, we can use $\{R_1, R_2\}$ to denote the conversion efficiencies of the individual stages (and define $T_j = 1 - R_j$, $j \in \{1, 2\}$). We can then model all of the coupling and transmission losses by placing virtual loss media on either side of idealized waveguides in all beams, as in [82]. Let x_1 and x_2 denote the ratios of the waveguide transmittances for the idler to that of the signal in stages 1 and 2 respectively. Also, let T_r, T_s be the transmittances of the idler and the signal from the exit of stage-1 waveguide all the way to the exit of the unpumped stage-2 waveguide (this includes propagation loss inbetween stages). Then the fringe visibility for the signal [82] would be

$$V_{signal} = \frac{2\sqrt{R_1 T_1 R_2 T_2}\sqrt{(T_r x_1)(T_s x_2)}}{R_1 R_2 (T_r x_1) + T_1 T_2 (T_s x_2)}. \tag{5.4}$$

The condition for maximum visibility with 50% CE in each stage is simply $T_r x_1 = T_s x_2$. Thus, for any configurational state, we can tweak the inter-stage coupling efficiency of the better-coupled beam to balance the loss on both arms and recover full visiblity.

In order to ensure that the waveguide used in the two stages were identical, I decided to double pass our pulses through the same waveguide, once in the "forward" direction, and once again in the "backwards" direction. This makes our scheme similar to a Michelson interferometer. In order to separate the final second-stage exit pump and signal beams from the input pump and signal beams, I used a Newport ISO-50-800-BB broadband Faraday optical isolator. Figure 66 shows the essential two-stage setup. Both pump and signal beams from the

shaper transmit through the Faraday isolator in the forward direction and hit the polarizing beam splitter (PBS), which splits them into two beams. Pump-1 pulse for the first stage transmits through the PBS to beam-A and goes through the waveguide in the "forward" direction, exits in beam-C, reflects off of the Thorlabs FF01-810/10 bandpass filter (DM2) and travels in the "backwards" direction along beam-B, then ultimately returning to the PBS, being reflected back to the isolator, and exiting it from the escape/reject port. The Pump-2 pulse for the second stage reflects at the PBS and travels in beam-B in the "forward" direction, then gets coupled into the waveguide in the "backwards" direction, and eventually makes it all the way back to the escape port. Thus, the two pump pulses (split from the shaper output at the PBS) travel through the waveguide in different directions at different times, forming the two FC stages.

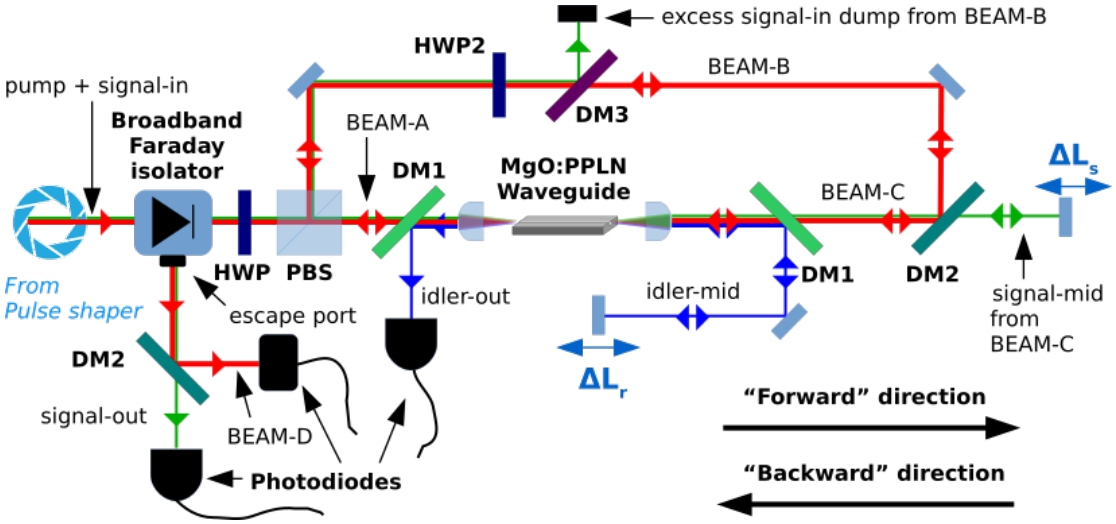

FIGURE 66. Dual-stage setup. Pump-1 loops around in the counter-clockwise direction starting from the polarizing beam splitter (PBS), while pump-2 loops around clockwise. Signal traverses left-to-right, reflects off of its end mirror, then tranverses right-to-left. Idler does the same. The two end mirrors are mounted on high-precision translation stages for phase control. HWP stands for half-wave plate. DM are dichroic mirrors. Some filters and optical elements are not shown.

The part of the signal that gets diverted to beam-A is discarded using a Thorlabs NF03-808E notch filter (DM3) and never participates in either stage. Signal-in, however, transmits through the PBS into beam-A, travels through the waveguide in the "forward" direction, travels all the way straight to its end-mirror and gets reflected back through the waveguide towards the isolator, to be eventually detected at the escape port. The idler is generated within the waveguide in stage-1 in the "forward" direction, then gets reflected by the Thorlabs DMLP650 longpass dichroic mirror (DM1) onto its end mirror, which reflects it back through the waveguide in the backwards direction, to be picked-off by another DM1 and directed towards a detector.

Both the signal-mid and the idler-mid end mirrors were mounted on Physik Instruments Q-545.140 piezo controlled linear translation servo stages. These have a movement range of 13 mm and a resolution of 5 nm, allowing for second-stage pulse overlap via course adjust, and idler/signal arm phase scan via fine adjust. Not shown in Fig. 66 are two microcontroller controlled servo-motor beam blocks in beam-B and beam-C. These can be used to programmatically cutoff pumping the second-stage alone, or block all second-stage beams. Since I worked at near room temperature and my waveguide's faces were not angle-cut to avoid backreflection, I had to time gate our desired signal pulse using a sample-and-hold circuit. While these can be easily and reliably employed to sample TTL pulses (such as those of avalanche photodiodes, used to measure subphoton power levels), dynamic control of beam blocks provided for another effective way to tease out the desired signal from the backreflection background whilst still using slow-integration detectors.

Since the pump and signal bands are very close in wavelength and co-polarized in the entire setup, I have had to rely on dichroic mirrors and similar elements with sharp edges in transmission versus wavelength to separate or combine them. Such optical elements tend to be dispersive near the transmission edge. To ensure that our frequency spectra are a good distance away from said edge, I have chosen to work with modified Hermite-Gaussian functions with comparable bandwidths for the two-stage experiment. The three mode shapes for bandwidth parameter $\Delta\omega$ are defined as follows (with normalization constants N_j):

$$HG0(\omega) = \frac{1}{\sqrt{N_0}} \exp\left(-\frac{(\omega-\omega_0)^2}{2\Delta\omega^2}\right), \tag{5.5}$$

$$HG1(\omega) = \frac{1}{\sqrt{N_1}} \left(\frac{\omega}{0.8\Delta\omega}\right) \exp\left(-\frac{(\omega-\omega_0)^2}{2(0.8\Delta\omega)^2}\right), \tag{5.6}$$

$$HG2(\omega) = \frac{1}{\sqrt{N_2}} \left[2\left(\frac{\omega}{0.89\Delta\omega}\right)^2 - 1\right] \exp\left(-\frac{(\omega-\omega_0)^2}{2(0.8078\Delta\omega)^2}\right). \tag{5.7}$$

The width modifications ensure mutual orthogonality whilst restricting total bandwidth of all three modes to the same neighborhood. I will numerically refer to them as modes 0, 1, and 2. Figure 67 shows the frequency spectra and the time-domain amplitudes for these functions.

Figure 68 plots the single-stage CE for all nine possible signal-pump shape combinations versus $\tilde{\gamma}$, analogous with Fig. 63. The behavior up to 50% CE is entirely along expected lines. Theoretical curves are not shown for the sake of clarity. In addition, Figs. 69-70 show the single-stage CE versus pump-signal delay for pump powers set for 50% CE at zero delay. The zero-delay value for $HG0$ had to be set to center the maxima, to compensate for temporal skewness observed in Fig. 62(a).

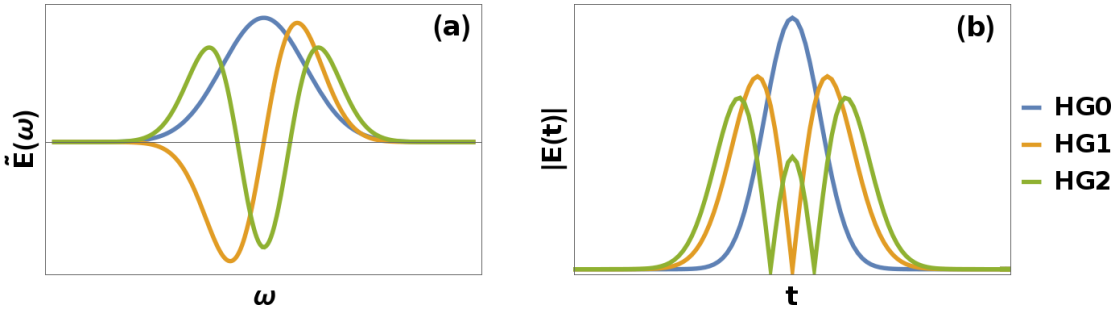

FIGURE 67. (a) Frequency spectra and (b) corresponding temporal-mode amplitudes for the modified Hermite-Gaussian functions defined in Eqs. 5.5-5.7. Note that the bandwidths of the spectra are nearly equal.

The smallest reliable step size for both the "red mirror" (s-band) and "blue mirror" (r-band) linear translation stages was 10 nm. I used this to verify the temporal extent of the generated blue TM by using the second stage to backconvert it to red. Figure 72 was generated by scanning the blue mirror and using the second-stage pump to FC the idler back into the signal band. The unconverted first-stage signal has been discarded.

The expected profile in Fig. 72 is a triangle (square pulse convolved with a square pulse). This is because the first-stage-generated idler pulse is roughly a long, square pulse, and the second-stage pump convects through it due to group-velocity mismatch. The back-CE will be optimum when the mirror position allows the pump to convect through the entire blue idler pulse within the waveguide. The spatial FWHM width of the triangular profile centered at around mirror position 3.2 mm is 0.8 mm. Since this is a back-reflection setup, the pulse spatial width is 1.6 mm. This implies that our ζ is roughly 10, as opposed to the expected 20. I suspect that this is due to imprecise modeling of the waveguide dispersion.

Also of note in Fig. 72 is the secondary peak at mirror position 4 mm. This is the double-back-reflection of the blue light from both the first-stage output face, and the first-stage input face of the waveguide in sequence. This is due to

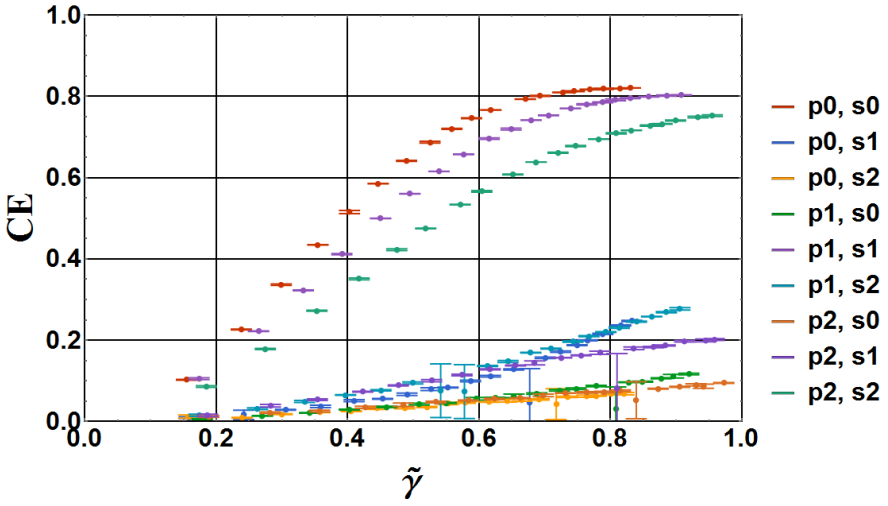

FIGURE 68. Single-stage conversion efficiencies versus $\tilde{\gamma}$ ($\propto$ square-root of pump power) for the nine pump-signal mode combinations. The legend label pj, sk designates pump in mode j and signal in mode k, where the modes are defined in Eqs. 5.5-5.7.

photorefractive effect, and can be eliminated by working at a higher waveguide temperature. This would change the waveguide phase matching condition. In my experiment, I treat this as a loss in the blue idler arm of the interferometer.

When all fields are allowed to participate in both stages, scanning the mirrors by fine amounts revealed interference fringes in the total CE. Tweaking the coupling efficiencies inbetween the stages to match across both colors would affect the visiblity of the fringes. Through manual adjustment alone, I measured a fringe visibility exceeding 0.8. Figure 73 shows the interference fringes for $HG0$ pump and signal shapes for the two-stage setup with both red-mirror and blue-mirror scanning. This reveals that $\Delta\phi_r$ advances about twice as fast as $\Delta\phi_s$ for the same corresponding mirror displacement, due to the ratio of their wavelengths.

I sought to confirm the relative signs of the $\Delta\phi_s$ and $\Delta\phi_r$ terms in Eq. 5.3 by moving both mirrors at once. Figure 74 shows the result of combined red-mirror blue-mirror steps, where the red-mirror step size was 20 nm, and the blue-

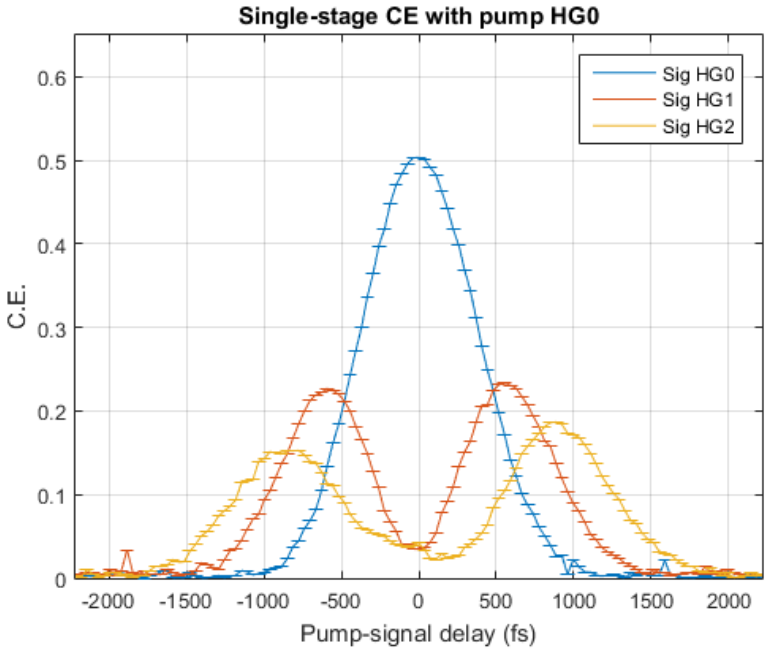

FIGURE 69. Single-stage conversion efficiency versus pump-signal input delay (applied using SLM) for HG0-shaped pump. Signal shapes are given in legend.

mirror step size was 10 nm. As can be seen, the phase rapidly varies when their displacements are in the opposite directions. There is a slow variation when they are displaced in the same direction due to the fact that their wavelengths are not exact harmonics, and the interferometer has native instability due to lab temperature fluctuations.

And finally, Figs. 75, 76, and 77 show the interference fringes for all nine pump-signal shape combinations. The fringe visibility and peak CE are maximized when both pump and signal shapes are matched, and suppressed when they are mismatched. I achieved CEs of up to 94% for the matched TM whilst suppressing a mismatched TM to 8% (Fig. 75), which is a contrast ratio of 11.75. The performance for all three pump shapes has exceeded that which was experimentally realizable in Fig. 64 with net lower total pump powers used. The peak CE hitting nearly 90% across all three shapes indicates that the optimum Schmidt modes

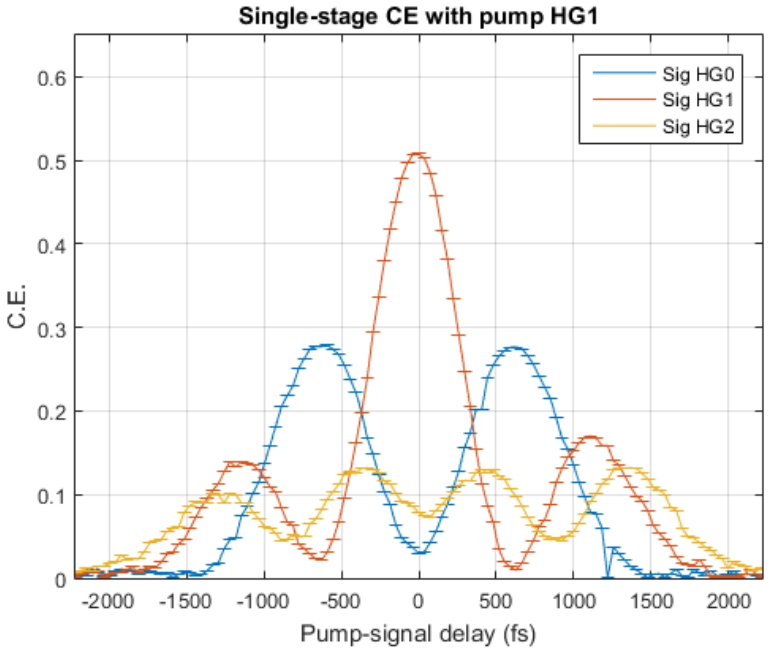

FIGURE 70. Single-stage conversion efficiency versus pump-signal input delay (applied using SLM) for HG1-shaped pump. Signal shapes are given in legend.

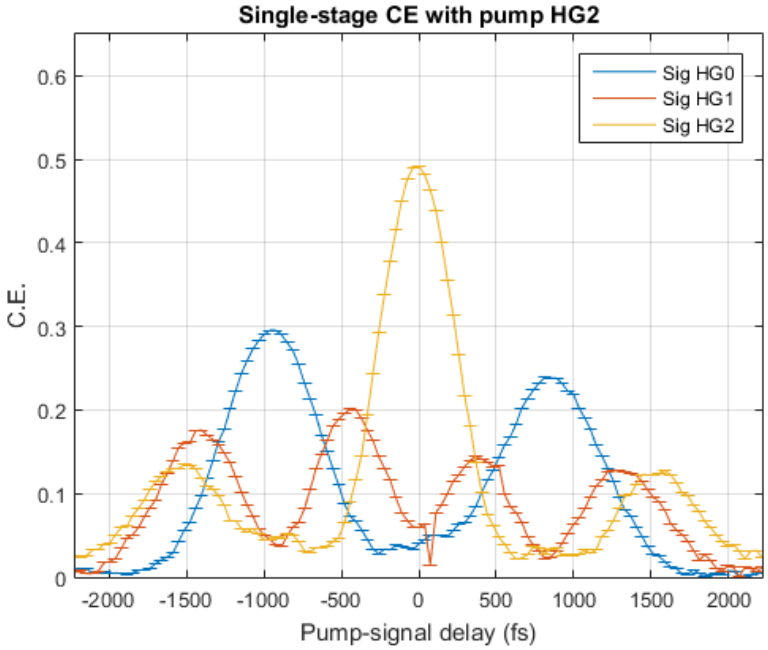

FIGURE 71. Single-stage conversion efficiency versus pump-signal input delay (applied using SLM) for HG2-shaped pump. Signal shapes are given in legend.

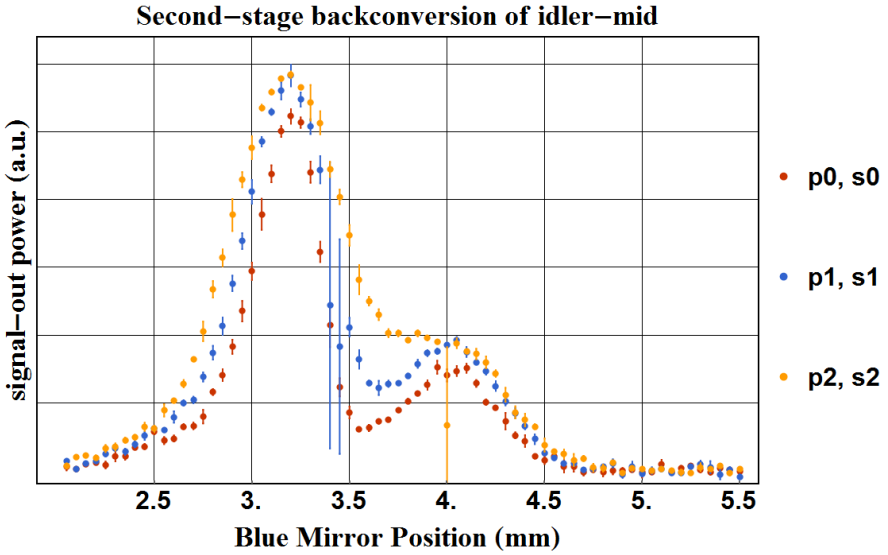

FIGURE 72. Second-stage back-conversion of idler generated in the first stage, showcasing the increased temporal width of idler, and the photorefractive secondary reflection peak centered at mirror position 4 mm. End mirror position is positive towards the waveguide. Legend label Pj, Sj implies pump and signal in mode j.

of the process are very close to the pump shapes, which was not true for the single-stage case at high CE (Fig. 64).

To conclude, Fig. 78 shows the bar graph of three-mode CEs for the two-stage TMI. The values are comparable to expected CEs for $\zeta = 10$, $\xi \to \infty$ from Fig. 45. A major caveat is that the signal coupling efficiencies into the waveguide in both directions were of the order of 30%. So even though the two-stage device is able to demonstrate selectivity enhancement, it has a native transmission efficiency of 10%. This, however, is not an insurmountable problem. At the time of this writing, efforts are on to improve the visibility, and study the device for input signal powers at subphoton levels.

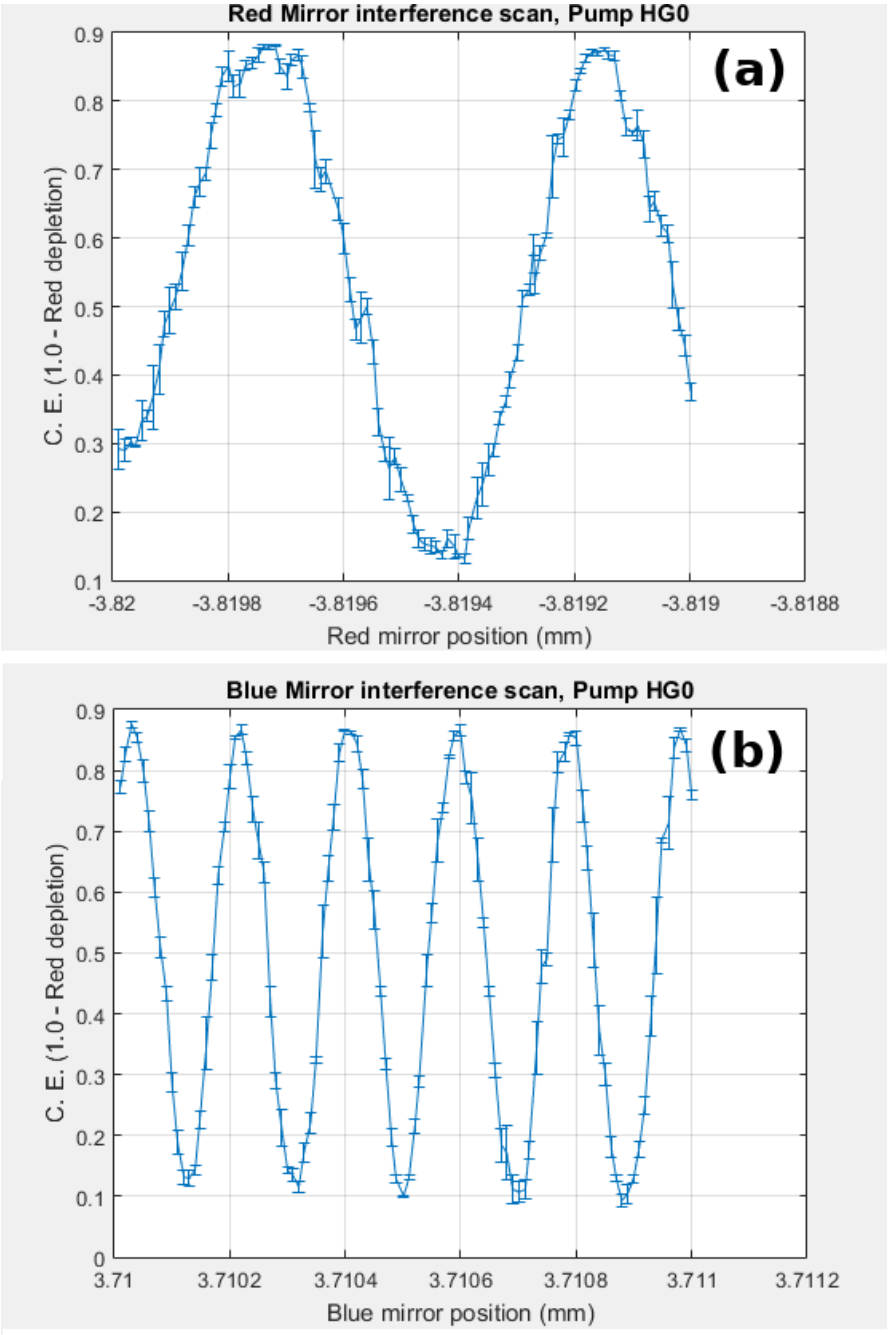

FIGURE 73. Interference fringes for $HG0$ pump and $HG0$ signal in two-stage setup. (a) Red mirror scan. (b) Blue mirror scan. Note that the phase accumulates about twice as fast for the blue mirror, due to its shorter wavelength. "Positive" mirror displacement is towards the waveguide.

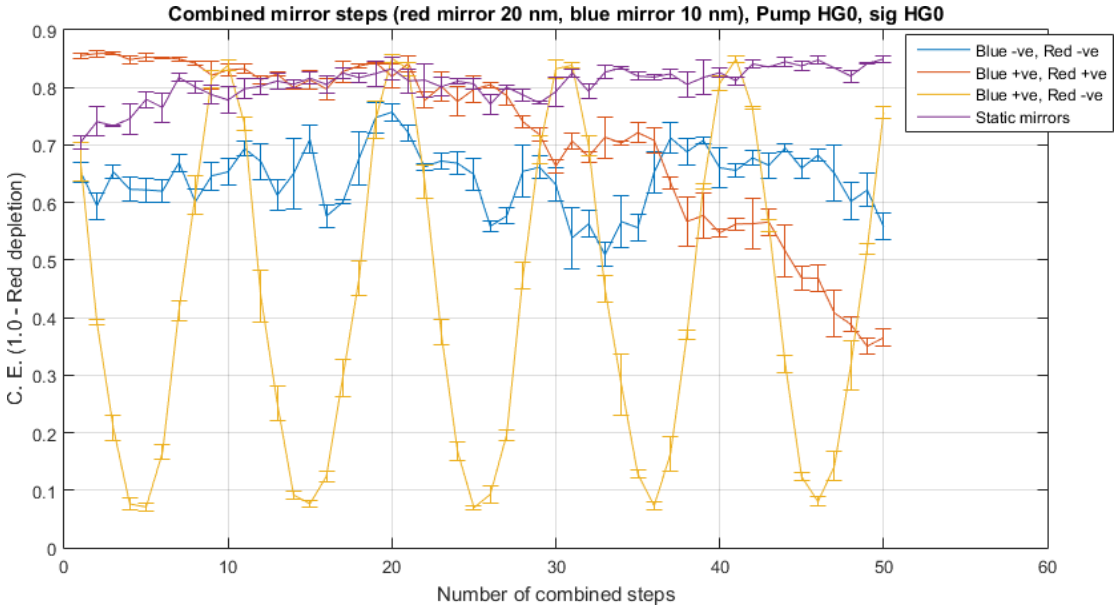

FIGURE 74. Combined mirror move, confirming the signs in Eq. 5.3. Positive mirror displacement is towards the waveguide for both mirrors.

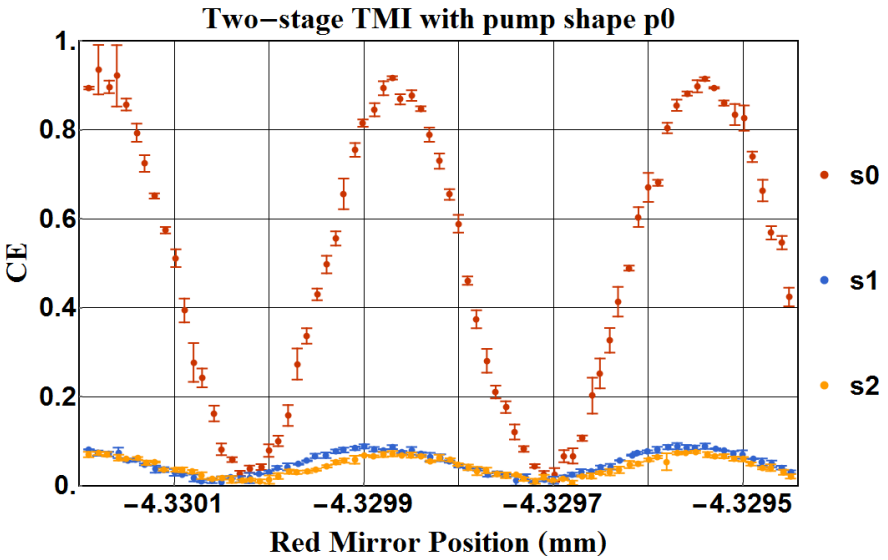

FIGURE 75. Two-stage TMI fringes for $HG0$ pump shape and three signal shapes. Red mirror position is positive towards the waveguide.

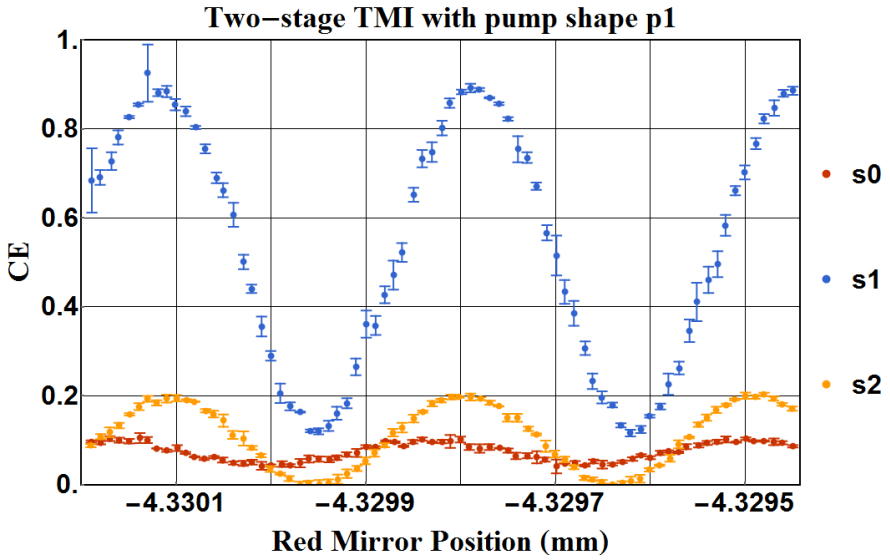

FIGURE 76. Two-stage TMI fringes for $HG0$ pump shape and three signal shapes. Red mirror position is positive towards the waveguide.

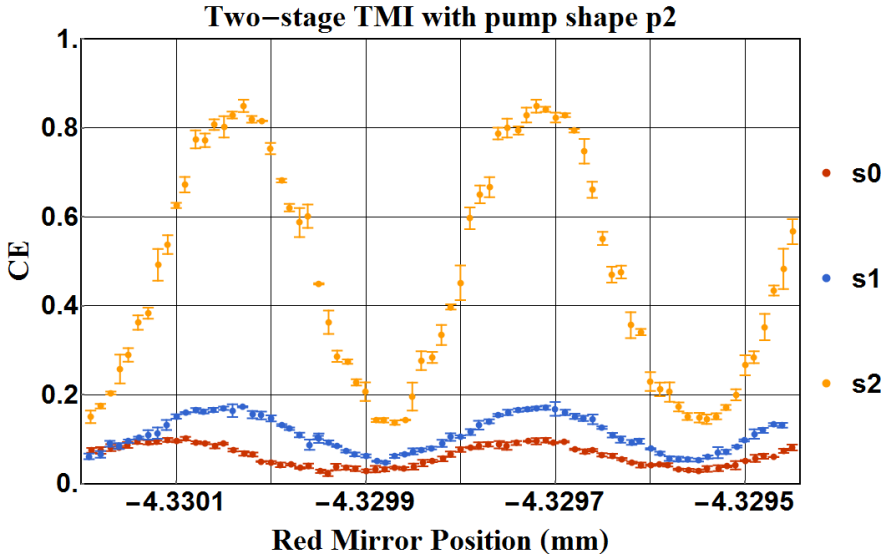

FIGURE 77. Two-stage TMI fringes for $HG0$ pump shape and three signal shapes. Red mirror position is positive towards the waveguide.

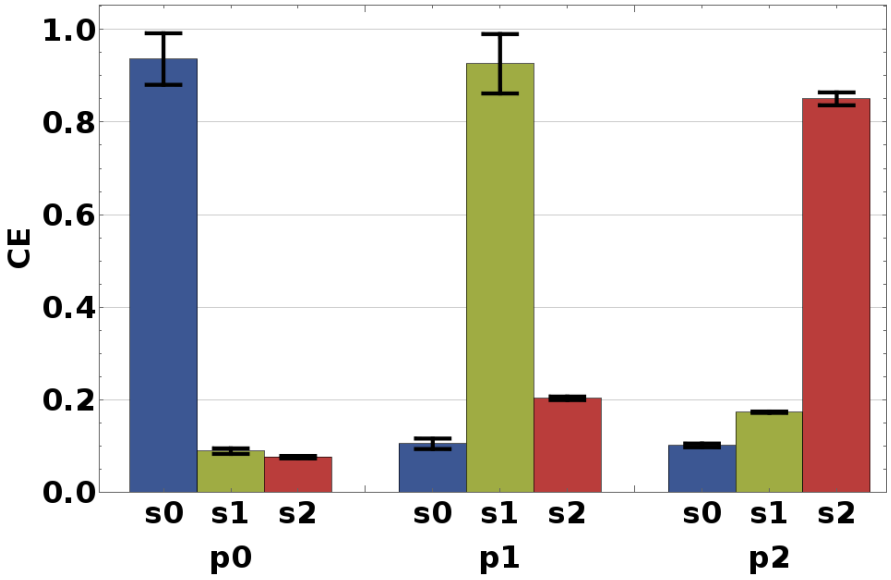

FIGURE 78. Maximum conversion efficiencies for various pump-signal mode combinations in a two-stage temporal-mode interferometer.

CHAPTER VI

IMPROVEMENTS AND FUTURE IMPLICATIONS

This chapter contains published co-authored material from [28], as well as a concept from [45]. The material from [28] was my contribution to the work, and I made the original derivation of the concept from [45]. I fully acknowledge all of my co-authors Dr. Benjamin Brecht, Prof. Christine Silberhorn, and Prof. Michael G. Raymer for their role in these publications.

Design Constraints and Limitations

Experimental pitfalls

The experiment presented in Chapter V was designed under constraints of financial feasibility, and availability of materials and fabrication facilities. For this document to serve as a guide for replication, or further iterations of similar setups, I think it prudent to list some pitfalls and stumbling blocks that I encountered that the reader should be aware of.

In order to dynamically tune and divert the beam power into various paths, I have employed combinations of polarizing beam splitters (PBS) and half-wave plates (HWP) on rotation mounts. Since all of our beams are linearly polarized, the HWP will ideally rotate the linear polarization angle, and the PBS would then project different powers onto the horizontal and the vertical polarization output ports. In practice, however, most HWPs have a phase-retardation that is dependent on the wavelength. While the effect of a linearly varying phase retardation on a spectrum is equivalent to a simple time delay, the

differential projection onto the PBS output ports amounts to a spectral amplitude modulation. This limited the dynamic setting of HWPs during an experiment, as the amplitude masks on the pulse shaper needed to be recalculated for every HWP orientation. I recommend that the experimenter invest in achromatic half-wave plates that are specifically designed for flat phase retardation across a wide band of wavelengths.

Another major source of errors can be the use of dielectric mirrors. Even though they have superior flat reflectance, they are multilayer interferometric devices, and as such will introduce significant dispersion onto even pulses that are 2 nm wide. I recommend using metallic mirrors. Even silver mirrors with thin, protective P01 coating served really well for observation of interference fringes.

Since I opted to use a Type-0 second-harmonic generation waveguide to perform SFG, all of our fields were co-polarized. This meant that I had to rely on dichroic mirrors and filters to separate and combine different bands into beams. While this is not an issue for the blue 408 nm idler verses the red pump and signal, the pump and signal were really close in frequency. This required us to use angle-tunable bandpass and notch filters with sharp transmission edges shown in Fig. 79.

Due to the Kramers-Kronig relations between the real and the imaginary parts of refractive index, sharp edges in transmission will necessarily introduce dispersion. Figures 80 and 81 show the calculated approximate dispersion curves for the two filters listed in Fig. 79. Even though these are small, care must be taken when double-passing through them to increase extinction ratios. Stacking multiples of them in front of detector fiber couplers should not be an issue.

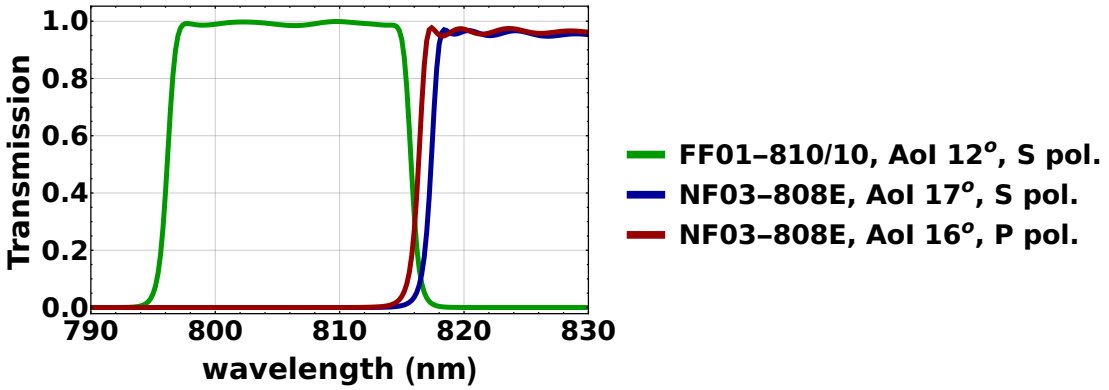

FIGURE 79. Transmission vs wavelength profiles at polarizations and angles of incidence (AoI) for optical filters from Semrock.

The first-order blazed grating method for utilization of 2D-phase-only spatial light modulators to perform both amplitude and phase modulation has a fundamental problem. This is that different wavelengths have different exit angles for the same vertical grating period. This introduces a transverse spatial chirp on the beam. Bands as narrow as 2 nm do not suffer hugely from this, but if extending to bigger bandwidths, the experimenter has to be aware that this will introduce another amplitude modulation due to frequency-dependent coupling efficiency into single-mode waveguides.

And finally, it is very important to prevent backreflections from both faces of the waveguide in both directions. Waveguides manufactured to length specifications are usually cut at an angle to divert backreflections to different angles. They also sometimes come with antireflection coating for some range of wavelengths. Operating nonlinear waveguides at high temperatures not only controls for phasematching wavelengths but also mitigates photorefractive effect, which can be responsible for significant backreflections, particularly for shorter wavelengths. I feel that this is not emphasized enough in modern nonlinear frequency conversion literature.

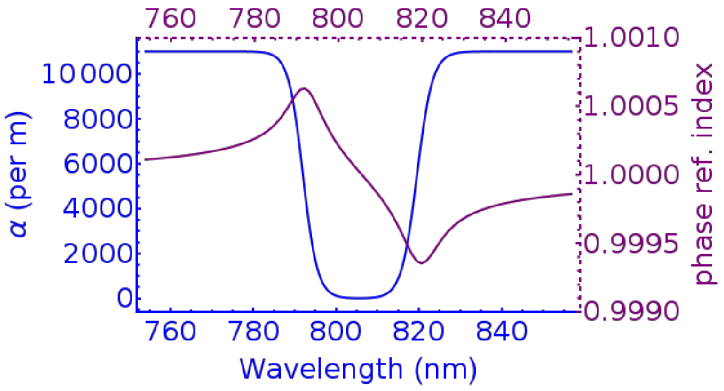

FIGURE 80. Approximate absorption coefficient and refractive index (indicating dispersion) for the Semrock FF01-810/10 bandpass filter for S-polarization at angle of incidence 12°. Calculated using Kramers-Kronig algorithm developed by Dr. Kyle Klarup.

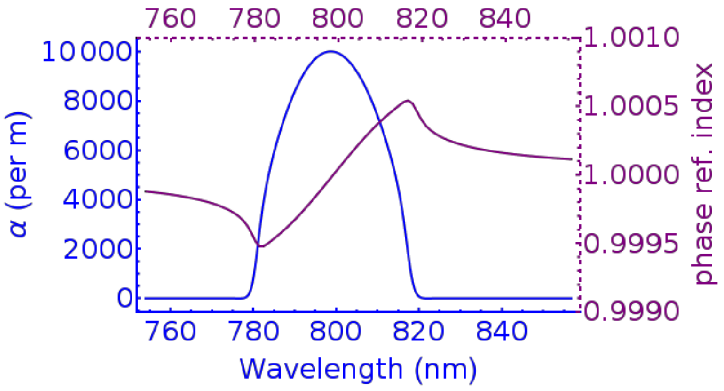

FIGURE 81. Approximate absorption coefficient and refractive index (indicating dispersion) for the Semrock NF03-808E notch filter for S-polarization at angle of incidence 17°. Calculated using Kramers-Kronig algorithm developed by Dr. Kyle Klarup.

Fundamental TMI deficiencies

Temporal-mode interferometry solved the uniform-velocity coherent pulse-interaction problem, but imposed certain restrictions on how desired high TM-selectivity can be achieved. The technique relies on drastic differences in the

group velocities of the signal-idler pair. Realistic dispersion curves for bulk nonlinear crystals put severe limits on how large this difference can be. Waveguide geometries are also limited in how much they can modify the dispersion. Therefore, one has to operate in longer waveguides to compensate for the small group-velocity mismatch. This presents problems for miniaturization.

A related constraint is on the widths of the temporal modes that we can operate on. My implementation utilized a 5 mm long, PPLN waveguide and used sub-picosecond pulses to ensure good signal-idler walkoff. Most quantum memories operate in the tens of nanoseconds regime (some even in microseconds), and long-distance fibers require very narrow bandwidths for dispersion-free propagation. One could perform TMI in long fibers using two pumps and FWM (with appropriate chirp control) and ensure full pulse collision, but the lengths required start to get unfeasible for microsecond pulses.

There is the unavoidable issue of coupling loss into discrete optical modules. This becomes burdensome for any multistage scheme. Designing TMI in a fully integrated system would resolve this, but comes with its own challenges. I next propose a new scheme for quantum pulse gating using cavities that can overcome some of these deficiencies. I consider this a natural extension of infinite-stage TMI.

Dichroic-Finesse Cavity-Based Approach

Cavities around nonlinear processes have long been a subject of scrutiny [31]. Their employment in atomic-ensemble or solid-state quantum memories is known to bare TM selective qualities for optical storage [103, 104]. They are also known to suppress spurious and undesirable terms in the governing equations [104]. They

have been used in purely nonresonant optical nonlinear processes like photon-pair generation to innovatively shape the joint-spectral amplitudes [105, 106], or create multi-partite entanglement across several bands of a frequency comb [107, 108]. Here I propose a means of using cavities with a deliberate and drastic difference in optical finesse for two frequency bands participating in nonlinear frequency conversion, to mimic the TM selective behavior seen in quantum memories. This provides a simple, integrable way to perform effectively infinite-stage TMI for a wide, tunable range of signal bandwidths without the added complications of maintaining cold-atom traps, or any inhomogeneous broadening.

Conceptual design

The solutions to the coupled-mode equations of motion with the typical nonlinear structure can always be expressed as an integral scattering relation between input and output temporal modes using the Green function formalism. Subkernels of said Green function are functions of both an input-mode time argument and an output-mode time argument. For the process to be mode discriminatory, the subkernels should be separable in its variable arguments, which is impossible for time-stationary processes (where the entire Green function reduces to that of a single argument, that being a difference in the two times). This is the reason that the control fields (laser pumps for example) have to necessarily be pulsed (i.e. time-varying, on the time-scale of the TMs in question) for any TM selective features to manifest.

Another, but related, key requirement for selectivity has been a drastic difference in the group velocities between the various frequency bands [40–42, 44]. Orthogonal TMs can share very similar (even identical) mode features in local time

slices, as shown in Fig. 82. For the QPG to perform different transformations on these two TMs, the full global mode structure will need to be sampled by the device, as the effect (depletion/enhancement/phase-shift) on any given time slice should depend on features in all other time slices across multiple frequency bands. Differing group velocities will cause pulsed modes from different bands to convect through each other as they interact. This is an effective means of carrying local mode information across different time slices by imprinting them into different bands. A bad choice of group velocities (like perfect copropagation) can result in highly TM agnostic process [40].

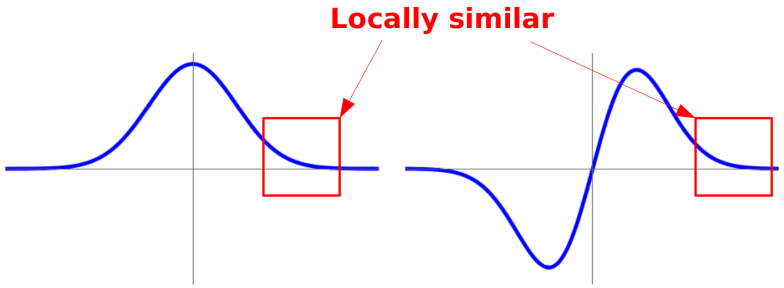

FIGURE 82. Two orthogonal temporal modes, with locally similar time slices highlighted.

TMI causes convecting pulses to overlap in spacetime over multiple stages, with the interaction being semi-perturbative in each stage. This avoids Burnham-Chaio ringing effects [88] induced by cascaded second-order nonlinearity [97, 98] and ensures Green function separability at high pump powers [93]. This full pulse sampling (or full collision) requirement constraints the minimum possible waveguide lengths of QPGs based on nonlinear frequency conversion (this length being determined by group-velocity differences and the desired TM widths [40, 44]). Another way to force inter-pulse convection is to confine the modes of one of the bands in physical space as the other modes pass through it. An obvious means of such long-term confinement is via circulation in a high-finesse cavity. And the

cavity mode amplitude can be amplified from within the confines of such a cavity, obviating the need for an means of optimum input coupling.

Figure 83 shows a schematic diagram of the system I propose. $S(t)$ and $C(t)$ are the resonant cavity modes of the two frequency bands that will interact via the nonlinearity of the medium. The control field $\Omega(t)$ can be a single laser pulse if the ring cavity is utilizing three-wave mixing. The temporal widths of the control field and the signal input $S_{\text{in}}(t)$ have to be much longer than the cavity round-trip time, but much shorter than the $C(t)$ cavity life time. This allows us to ignore the slow leakage of $C(t)$ amplitude out of the cavity during the process. It then becomes analogous to a coherent spin wave (for example) in an ultracold atomic ensemble. The cavity-coupling coefficients have to put $S_{\text{in}}(t)$ in the bad-cavity limit for the scheme to work. This finesse differential across the bands is the Yin-Yang necessary to break the interaction symmetry. This design works for pumps and signals with arbitrary relative group velocities, which is a major advantage over more straight-forward TMI implementations. The temporal width of the input mode is therefore tunable, and constrainted from both ends, which is very similar to the inequalities regarding the dimensionless parameters in [44].

Mathematical derivation

The basic idea combines the cavity input-output theory presented in [105], along with a means of combining that with the bad-cavity limit, as presented in [104]. I use a nonlinear waveguide shaped like a ring cavity, and frequencies that are phasematched for the control/pump field $\Omega(t)$, signal $S_{in}(t)$, and idler $C(t)$. The key to make the device work is to have the cavity coupling be frequency dependent, i.e. with transmission/reflection coefficients $\{t_s, r_s\}$ for

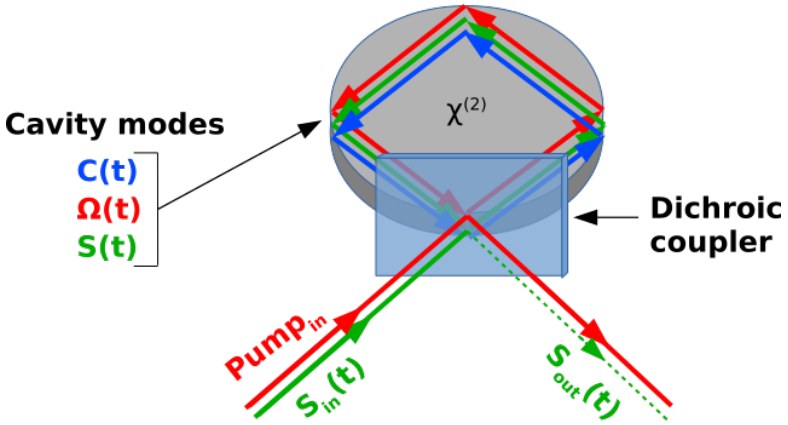

FIGURE 83. A second-order nonlinear ring cavity with a dichroic coupler (coupling coefficents are different for s-band and c-band. The input $S_{in}(t)$ gets frequency converted into the long-lived c-band cavity mode $C(t)$, mediated by the pump field.

carrier frequency ω_s, and $\{t_c, r_c\}$ for carrier frequency ω_c. This will allow us to apply the bad-cavity limit only to the S-field, and assume that the cavity has very high finesse for the C-field. Then, we can frequency convert $S_{\text{in}}(t)$ into a long lived, resonant cavity mode at frequency ω_c within the cavity. The process occurs for long, slowly varying pump and signal fields $\Omega(t)$ and $S_{\text{in}}(t)$, but has to finish before any of the created $C(t)$ has naturally leaked out of the cavity. The created $C(t)$ can be allowed to leak out slowly at a later time, or can be reconverted using a second pump pulse back into the S-band, with potential for reshaping as well. This process can be shown to be temporal-mode selective, and, in the absence of losses, can approach unit efficiency.

Let the cavity length be L, and the signal and idler modes (annihilation operators) within the cavity be $S(z,t)$ and $C(z,t)$ respectively, where $z \in [0, L]$. If we absorb the square-root of pump energy into parameter γ such that the control-field shape $\Omega(t)$ is square normalized, then the equations of motion within the cavity turn out to be:

$$(\partial_z + \beta_c'\partial_t)C(z,t) = i\gamma\Omega(t)S(z,t) - \kappa_c C(z,t), \tag{6.1}$$

$$(\partial_z + \beta_s'\partial_t)S(z,t) = i\gamma\Omega^*(t)C(z,t) - \kappa_s S(z,t), \tag{6.2}$$

where β_c' and β_s' are the group-slownesses (inverse group velocities) of the S- and C-bands respectively. κ_s and κ_c are complex decay rates that account for dispersion and loss. As in [104], I omit the Langevin noise operators that are required to maintain bosonic commutation relations as they do not contribute to the signal intensities.

In the weak-interaction-per-single-round-trip limit, we get

$$C(L,t) = e^{-\kappa_c L}C(0,t) + i\gamma L\Omega(t)S(0,t) - L\beta_c'\partial_t C(0,t), \tag{6.3}$$

$$S(L,t) = e^{-\kappa_s L}S(0,t) + i\gamma L\Omega^*(t)C(0,t) - L\beta_s'\partial_t S(0,t), \tag{6.4}$$

where $\{\tau_c, \tau_s\}$ are the cavity round-trip times. The cavity boundary conditions are:

$$S(0,t) = r_s e^{ik_s L}S(L,t) + t_s S_{\text{in}}(t), \tag{6.5}$$

$$C(0,t) = r_c e^{ik_c L}C(L,t) + t_c C_{\text{in}}(t). \tag{6.6}$$

Substituting the cavity boundary conditions into the weak-interaction equations gives us

$$\partial_t C(0,t) = \frac{i\gamma}{\beta_c'}\Omega(t)S(0,t) + \frac{1}{L\beta_c'}\left[e^{-\kappa_c L} - \frac{1}{r_c e^{ik_c L}}\right]C(0,t) + \frac{t_c}{L\beta_c' r_c e^{ik_c L}}C_{\text{in}}(t), \tag{6.7}$$

$$\partial_t S(0,t) = \frac{i\gamma}{\beta_s'}\Omega^*(t)C(0,t) + \frac{1}{L\beta_s'}\left[e^{-\kappa_s L} - \frac{1}{r_s e^{ik_s L}}\right]S(0,t) + \frac{t_s}{L\beta_s' r_s e^{ik_s L}}S_{\text{in}}(t). \tag{6.8}$$

Suppressing the z-argument for cavity modes (small cavity limit), consolidating the square-bracketed terms and prefactors into $\{\overline{\gamma}_c, \overline{\gamma}_s\}$ by defining $\overline{\gamma}_j = (\exp[-ik_j L]/r_j - \exp[-\kappa_j L])/(L\beta_j')$, and rewriting with $C_{\text{in}}(t) \to 0$, we have

$$\partial_t S(t) = i\frac{\gamma}{\beta_s'}\Omega^*(t)C(t) - \overline{\gamma}_s S(t) + \frac{t_s e^{-ik_s L}}{L\beta_s' r_s}S_{\text{in}}(t), \tag{6.9}$$

$$\partial_t C(t) = i\frac{\gamma}{\beta_c'}\Omega(t)S(t) - \overline{\gamma}_c C(t). \tag{6.10}$$

Note that the losses ($\Re[\kappa_j]$) are included in the $\overline{\gamma}_j$ parameters. Now, applying the bad-cavity limit to $S(t)$, *i.e.* setting $\partial_t S(t) \to 0$, we get

$$S(t) = i\frac{\gamma}{\beta_s'\overline{\gamma}_s}\Omega^*(t)C(t) + \frac{t_s e^{-ik_s L}}{L\beta_s' r_s \overline{\gamma}_s}S_{\text{in}}(t), \tag{6.11}$$

$$\partial_t C(t) = \left[-\frac{\gamma^2|\Omega(t)|^2}{\beta_c'\beta_s'\overline{\gamma}_s} - \overline{\gamma}_c\right]C(t) + \frac{i\gamma t_s e^{-ik_s L}}{L\beta_c'\beta_s'\overline{\gamma}_s r_s}\Omega(t)S_{\text{in}}(t). \tag{6.12}$$

Here, I make the second crucial assumption, that is that the cavity has very high finesse for C-band ($\overline{\gamma}_c \approx 0$), and the entire process takes place well before

any amplitude from $C(t)$ has leaked out of the cavity. Introducing variables as stand-ins for coefficients, we can write:

$$\partial_t C(t) = f|\Omega(t)|^2 C(t) + g_s \Omega(t) S_{\text{in}}(t). \tag{6.13}$$

Now I perform the variable transformation: $t \to \epsilon(t) = \int_{-\infty}^{t} |\Omega(t')|^2 dt'$. The end of the "read-in" process occurs at $\epsilon(\infty) = 1$. And $\partial_t \to |\Omega(t)|^2 \partial_\epsilon$. I also define $c(\epsilon) = C(t)$, $\sigma(\epsilon) = S(t)/\Omega^*(t)$, and $\sigma_{\text{in}}(\epsilon) = S_{\text{in}}(t)/\Omega^*(t)$. We then have:

$$\partial_\epsilon c = fc + g_s \sigma_{\text{in}}, \quad \sigma = b_s c + p_s \sigma_{\text{in}}. \tag{6.14}$$

The solution is

$$c(\epsilon) = c(0)e^{f\epsilon} + g_s \int_0^1 d\epsilon' \theta(\epsilon - \epsilon') e^{f(\epsilon - \epsilon')} \sigma_{\text{in}}(\epsilon'), \tag{6.15}$$

where $\theta(\epsilon)$ is the Heaviside step function. Setting $c(0) = 0$, we get

$$c(\epsilon) = g_s e^{f\epsilon} \int_0^\epsilon d\epsilon' e^{-f\epsilon'} \sigma_{\text{in}}(\epsilon'). \tag{6.16}$$

The idler-cavity mode amplitude at the end of the process is $c(1) = 0$ if, and only if, $\sigma_{\text{in}}(\epsilon)$ is orthogonal to $e^{-f^*\epsilon}$. The function $e^{-f^*\epsilon}$ is thus, the optical TM for storage in this cavity. Hence, the process is temporal-mode selective.

Also, using the cavity boundary condition, we can get the unconverted signal

$$\sigma_{out} = t_s\sigma - r_s\sigma_{\text{in}} = t_s b_s c + (t_s p_s - r_s)\sigma_{\text{in}} \tag{6.17}$$

$$= t_s b_s g_s e^{f\epsilon} \int_0^{\epsilon} d\epsilon' e^{-f\epsilon'} \sigma_{\text{in}}(\epsilon') + (t_s p_s - r_s)\sigma_{\text{in}}(\epsilon). \tag{6.18}$$

Unconverted signal power $\int_0^1 |\sigma_{out}(\epsilon)|^2 d\epsilon$ bottoms out to a flat value asymptotically with increasing γ (pump energy), and approaches $(1 - r_s)^2/4$ for lossless cavities. Alternatively, the quantity $\beta_c' L|c(1)|^2$ saturates to β_s'/β_c' in a lossless cavity, which is another metric for successful frequency conversion. Integrated high finesse microcavities for frequency conversion are still a nascent field [109, 110]. The achievable finesse and loss numbers are within the promising temporal ranges for wider applicability. We are currently exploring this idea as a future direction of research [45].

Integrated Systems and Applications

I now dedicate the last section to exploring some applications of QPGs in both scientific research and technology. Quantum pulse gates operate on the tensor-product of two temporal-mode spanned Hilbert spaces for two distinct sets. In our analysis, the distinction is marked by the central frequency bands, but in general, the distinction could be mapped to any other arbitrary photonic degree-of-freedom that also yields high temporal-mode selectivity. In this section, I shall label the two spaces by the letters *'b'* and *'g'* to divorce them from the subscripts used thus far, and pictorially represent them as blue and green colored beams respectively. For the sake of simplicity, I will restrict myself to TWM implementations of QPG, but all results can be generalized to FWM implementations as well. I also

restrict myself to the RC configuration, as this preserves the temporal shape of the unconverted g-band modes. By convention, I choose the g-band to represent the one group-velocity matched to the pump. This enables us to selectively manipulate specific TM components of a g-photon by shaping the pump pulse appropriately.

By convention, a general guided single photon pure state may be represented by labels:

$$\begin{aligned} |\psi\rangle &= \sum_{i,j} C_{i,j}|g_i, b_j\rangle; & g_i &\in \{0, g_1, g_2, ...\} \\ & & b_j &\in \{0, b_1, b_2, ...\} \\ \langle b_k, g_l|g_i, b_j\rangle &= \delta_{il}\delta_{jk} \end{aligned} \tag{6.19}$$

Note that $|0, 0\rangle$ is the vacuum state. Since I am only considering TWM-QPG, I will effectively only have access to one temporal mode in the b-band. Consequently, the g-band temporal-mode subspace shall be treated as the primary qubit space. Hence, I may resort to the short forms $|0, b_1\rangle \equiv |0, b\rangle \equiv |b\rangle$, and $|g_2, 0\rangle \equiv |g2\rangle$.

To explore the applications of QPG, I represent their action on quantum-states by defining them as operators,

$$\begin{aligned} \widehat{QPG}_{g'} = \mathbb{I} &- |g', 0\rangle\langle g', 0| - |0, b\rangle\langle 0, b| \\ &+ |0, b\rangle\langle g', 0| - |g', 0\rangle\langle 0, b|, \end{aligned} \tag{6.20}$$

where the subscript g' labels the temporal mode being selected for by a pump pulse of shape $g'(t)$. The QPG devices will be pictorially represented by the symbols in

Fig. 84(a). In addition, I will also use $\widehat{FC}_{g'}$ to represent single-stage QFC devices operating at 50% CE for the first Schmidt mode (using pump-shape $g'(t)$) and near-zero for the rest [Fig. 84(b)]:

$$\begin{aligned}\widehat{FC}_{g'} = &\frac{1}{\sqrt{2}}|g',0\rangle\langle g',0| + \frac{1}{\sqrt{2}}|0,b\rangle\langle g',0| \\ &+ \frac{1}{\sqrt{2}}|0,b\rangle\langle 0,b| - \frac{1}{\sqrt{2}}|g',0\rangle\langle 0,b| \\ &+ \mathbb{I} - |g',0\rangle\langle g',0| - |0,b\rangle\langle 0,b|.\end{aligned} \tag{6.21}$$

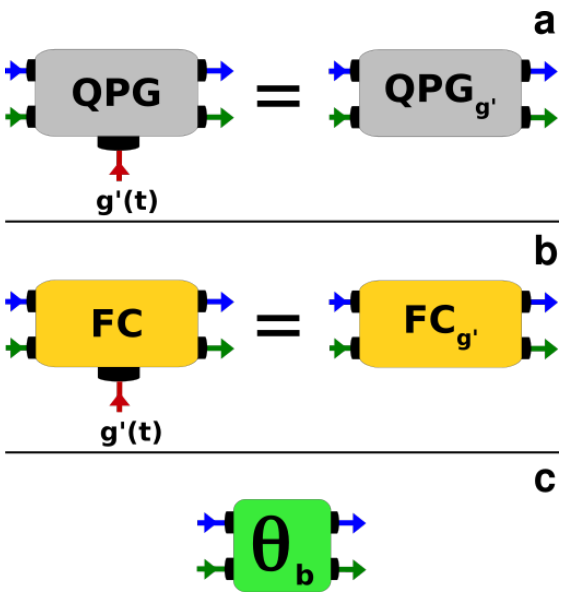

FIGURE 84. Pictorial representations of a TWM-QPG device (a) and a 50%-CE TWM-QFC device (b) being pumped by a pulse shaped $g'(t)$, as well as a band dependent phase-shifting device (c). The blue and green beams represent the b and the g bands, and need not be physically spatially separated paths.

Another useful unitary transformation that may be implemented is the band dependent arbitrary phase-shift operator [Fig. 84(c)]:

$$\widehat{\theta}_b = \sum_{g,b} e^{i\theta\delta_{b,0}} |g,b\rangle\langle g,b|. \tag{6.22}$$

Note that the b and g band beams in Fig. 84 are spatially separated for the sake of clarity, and in practice can be copropagating within the same waveguide.

Purity amplification and mode-shaping of heralded photon sources

Parametric photon-pair generators are used as sources of heralded quantum states of light. These devices are pumped by strong laser fields, and are spontaneous in photon-pair emission, thus requiring the detection of one of the pair to herald the existence of the other. However, for most common accessible operational parameters, the signal-herald photon pair tend to be highly spectrally entangled. Thus the reduced density matrix of a heralded signal-photon will be in a mixed state, limiting its usability in quantum experiments. The traditional workaround is to use narrow frequency bandpass filters and post-select photon pairs, but this approach severly reduces the photon-pair generation rate.

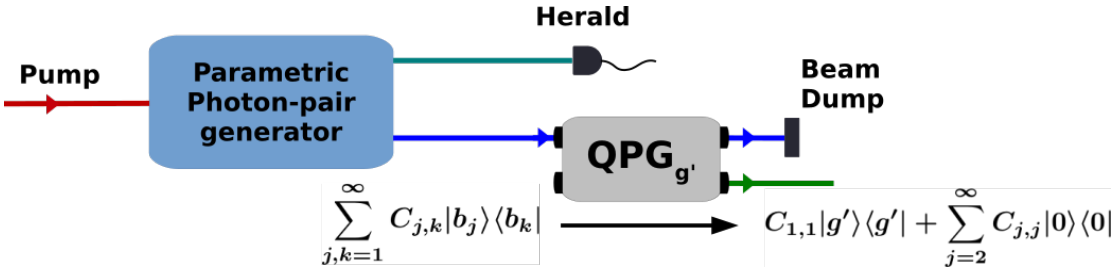

FIGURE 85. Purity amplification of heralded mixed-state signal photons through use of a QPG device. The temporal mode generated in the g-band is controlled by the shape of the QPG pump $g'(t)$.

A QPG device, timed by the heralding detector, can act as a mode-shape sensitive time-gate, or a phase-profile selective bandpass filter, to the mixed-state signal, thus increasing the state purity at a marginal cost to heralding efficiency.

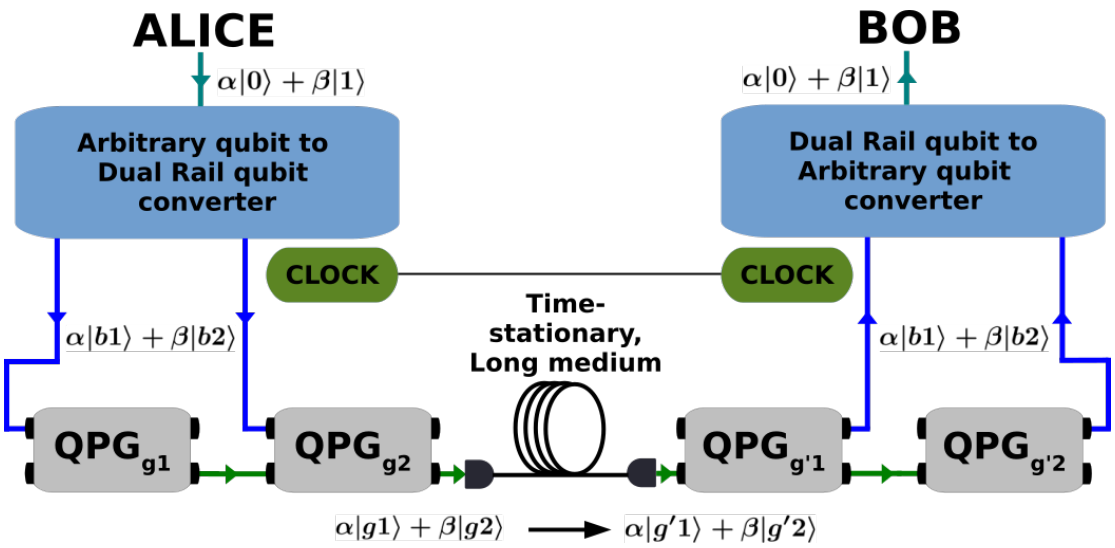

FIGURE 86. A setup for long distance quantum communication in the temporal-mode basis using QPG devices. The time-stationary long medium unitarily maps orthogonal input temporal modes ($|g1\rangle$, $|g2\rangle$) to orthogonal output temporal modes ($|g'1\rangle$, $|g'2\rangle$). This mapping can be pre-computed during the pre-data transfer handshake phase in the communication protocol. The clocks need to be synchronized for the timing of QPG pump pulses.

The mode of operation is illustrated in Fig. 85. The reduced density matrix of a heralded signal photon may be represented in the b-band temporal modes basis as

$$\hat{\rho}_s = \sum_{j,k=1}^{\infty} C_{j,k} |b_j\rangle\langle b_k|, \tag{6.23}$$

with purity $Tr[\hat{\rho_s}^2] = \sum_{j=1}^{\infty} C_{j,j}^2$. Post-selecting on the g-band output of the QPG device configured with pump shape $g'(t)$ will result in a state

$$\hat{\rho}_g = C_{1,1} |g'\rangle\langle g'| + \sum_{j=2}^{\infty} C_{j,j} |0\rangle\langle 0|, \tag{6.24}$$

with purity $Tr[\hat{\rho_g}^2] = C_{1,1}^2 + \left[\sum_{j=2}^{\infty} C_{j,j}\right]^2$. The heralding efficiency decreases by the factor $C_{1,1} \leq 1$.

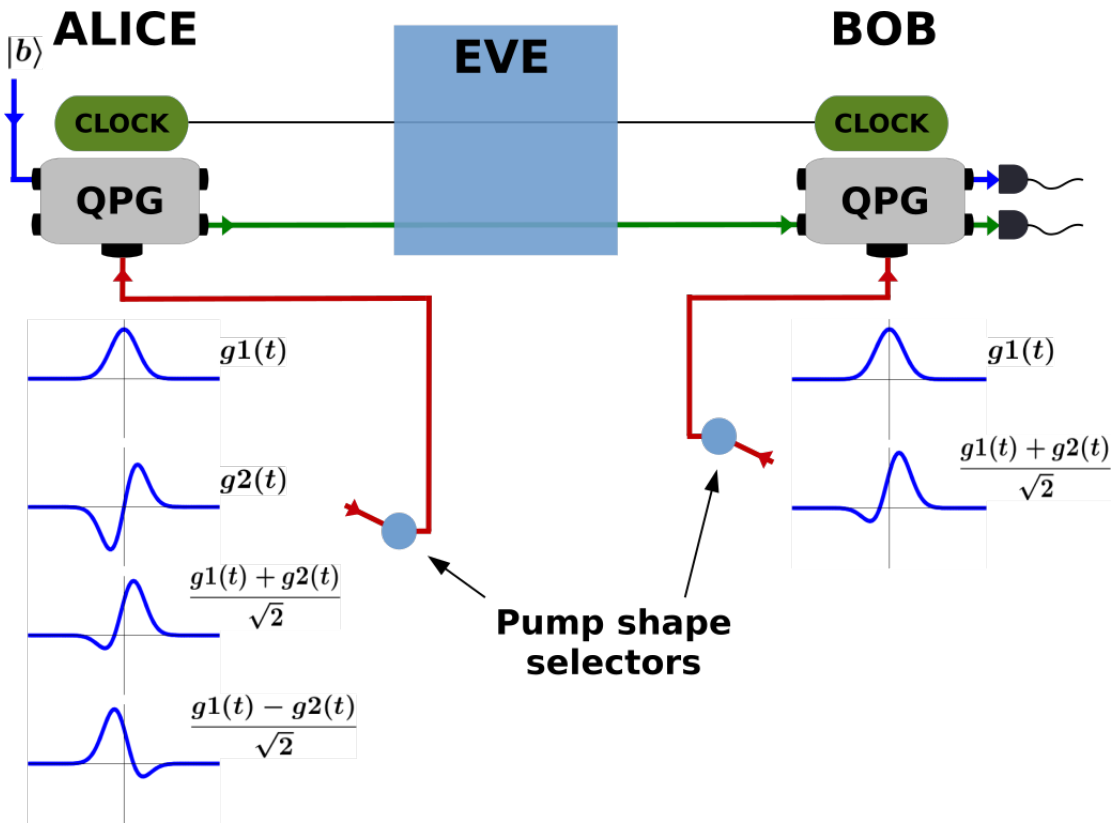

FIGURE 87. The BB84 quantum key distribution being implemented in the temporal mode space using QPG devices. The two mutually unbiased bases are $\{|g_1,0\rangle,\ |g_2,0\rangle\}$ and $\{(|g_1,0\rangle + |g_2,0\rangle)/\sqrt{2},\ (|g_1,0\rangle - |g_2,0\rangle)/\sqrt{2}\}$, and can be selected by appropriately shaped pump pulses.

Any practical long-distance communication of quantum states will rely on orthogonal states of photons. However, typical media (fiber, atmosphere) tend to have drastically different properties for different orthogonal modes (birefringence, group-velocity mismatch). The use of a pair of orthogonal temporal modes at the same frequency, polarization and transverse spatial mode, as a qubit basis can circumvent these issues. For example, Alice could use QPG devices to map an arbitrary qubit state unitarily into the $(|g_1,0\rangle,\ |g_2,0\rangle)$ subspace, as shown in Fig. 86. The photon will then be in a superposition:

$$|\psi\rangle = \alpha|g_1, 0\rangle + \beta|g_2, 0\rangle. \tag{6.25}$$

Even if the central frequency of the g-band is far from the zero-dispersion region of the long medium being utilized, the two separate components will be unitarily mapped to a subspace spanned by a different set of temporal modes ($|g_1', 0\rangle$, $|g_2', 0\rangle$), and may be decoded at Bob's end using QPG devices with appropriate pump shapes. The TM remapping characteristics of the long time-stationary medium can be pre-computed using an adaptive repeated test-signal measurement procedure before the start of data transfer, much like how modems compensate for channel noise during the handshake phase. The sender and recipient parties will need to synchronize their clocks via a classical channel in order to time their QPG pump pulses. Alternatively, a weak coherent pump pulse can be sent over along with the signal and amplified at the receiving end.

Quantum key distribution

A natural extension of the TM quantum communication ability is quantum key distribution (QKD) using the temporal mode basis. Figure 87 illustrates the use of QPG devices and pump-pulse shaping technologies to implement the BB84 QKD protocol.

In the scheme, Alice encodes her key into qubits expressed in either of the mutually unbiased basis sets $\{|g_1, 0\rangle, |g_2, 0\rangle\}$ or $\{(|g_1, 0\rangle + |g_2, 0\rangle)/\sqrt{2}\ , (|g_1, 0\rangle - |g_2, 0\rangle)/\sqrt{2}\}$ at random. Bob then performs a projective measurement on each photon in the same sets in a different random sequence. At the end, Alice and Bob publicly share their basis choice sequences and thus retain only those bits of the key which happened to have been prepared and measured in matching basis

sets. Any projective measurement by an eavesdropper can be detected using the standard protocols. The increased dimensionality available with TMs can also enhance QKD security.

Linear optical quantum computing

Temporal-mode qubits are a possible contender for the preferred photonic basis in quantum computing. QPG and related devices operator on guided photons, and may be integrated into chip-scale devices and utilized sequentially as gates in a quantum Turing machine. Due to the linear nature of the technique, deterministic two-qubit gates are provably impossible. However, arbitrary single-qubit operations can be realized by any combinations of the operators defined in Eqs. (6.20), (6.21) and (6.22).

Figure 88 shows how these three elements may be used sequential with the right pump shapes to implement the following single-qubit operations (up to an overall phase) on the $\{|g_1,0\rangle, |g_2,0\rangle\}$ space:

– Hadamard gate [Fig. 88(a)]:

$$\left[\frac{|g_1,0\rangle + |g_2,0\rangle}{\sqrt{2}}\right]\langle g_1,0| + \left[\frac{|g_1,0\rangle - |g_2,0\rangle}{\sqrt{2}}\right]\langle g_2,0|. \tag{6.26}$$

– Pauli-X gate (type I, II) [Fig. 88(b,c)]:

$$|g_2,0\rangle\langle g_1,0| + |g_1,0\rangle\langle g_2,0|. \tag{6.27}$$

– Pauli-Y gate (type I, II) [Fig. 88(d,e)]:

$$-i|g_2,0\rangle\langle g_1,0| + i|g_1,0\rangle\langle g_2,0|. \tag{6.28}$$

– Pauli-Z gate [Fig. 88(f)]:

$$|g_1,0\rangle\langle g_1,0| - |g_2,0\rangle\langle g_2,0|. \tag{6.29}$$

– Phase-shift gate [Fig. 88(g)]:

$$|g_1,0\rangle\langle g_1,0| + e^{i\theta}|g_2,0\rangle\langle g_2,0|. \tag{6.30}$$

These implementations rely on just two pump shapes. The phase-shift gate can be realized without the need for the band dependent arbitrary phase-shift operator if we can introduce the phase $(\theta + \pi)$ on one of the two pump pulses being used.

The b-band is being used as an auxillary band, as TWM-QPG only allows access to one b-temporal mode. Hoewever, FWM-QPG can expand the available TM-space dimensionality, at the cost of the need for additional pump resources.

Temporal-mode state tomography

QPG can be used as a tunable TM-projective measurement device. This allows for a direct measurement of the complete longitudinal/spectral quantum state of a repeatable photon source.

Figure 89(a) shows how a single-pump TWM-QPG device may be used for TM state tomography of a single photon source. We may express the density

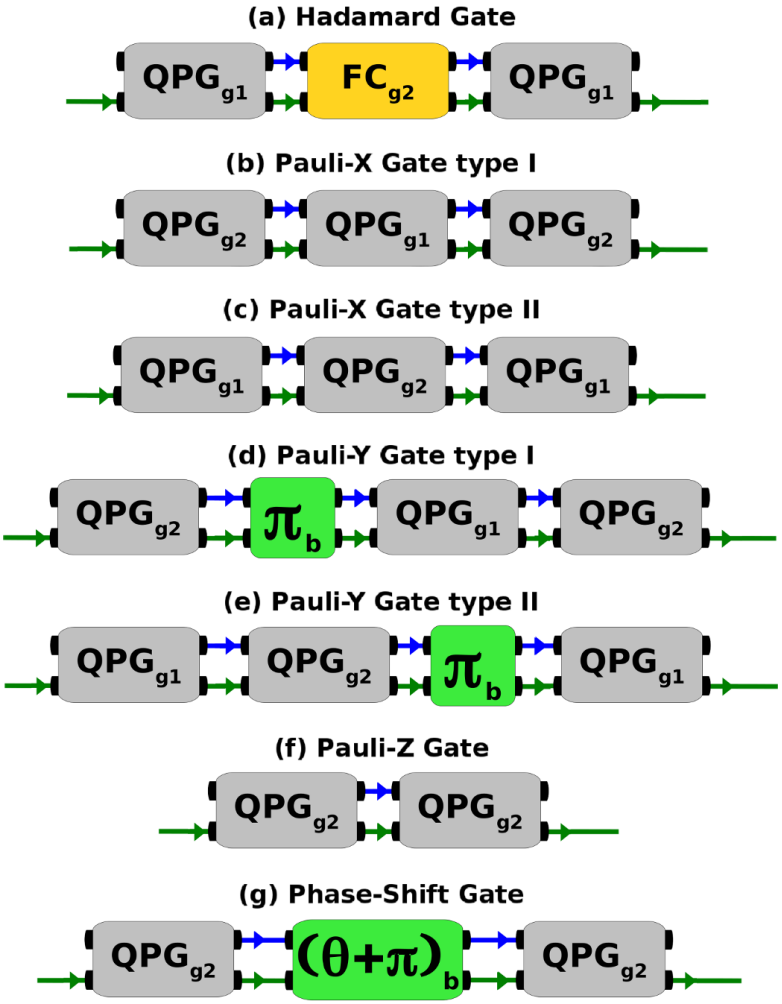

FIGURE 88. Various single-qubit quantum gates implemented (up to overall phase) by sequential use of TWM-QPG and related devices on the temporal-mode qubit.

matrix of the single-photon source in an experimentally convenient TM basis $\{|g_i, 0\rangle\}$:

$$\hat{\rho}_{IN} = \sum_{i,j} C_{i,j} |g_i, 0\rangle\langle g_j, 0|. \tag{6.31}$$

This state is measured by a QPG device pumped with a shape $[\alpha]g_k(t) + [e^{i\theta}\sqrt{1-\alpha}]g_l(t)$, for some θ and real α. Single-photon detectors are used at the b

and g outputs, and average counts N_b and N_g are measured over several iterations. Then,

$$\frac{N_b}{N_b+N_g} = \alpha^2 C_{k,k} + (1-\alpha^2)C_{l,l} + 2\mathfrak{Re}\left[\alpha\sqrt{1-\alpha^2}e^{i\theta}C_{k,l}\right]. \tag{6.32}$$

Cycling through the parameter values $(\alpha,\theta) \in \{(1,-),(0,-),(1/\sqrt{2},0),(1/\sqrt{2},\pi/2)\}$ will reveal the values of $C_{k,k}$, $C_{l,l}$, and the complex coefficient $C_{k,l}$ (and by extension, $C_{l,k}$). One cover either the entire space spanned by the basis $\{|g_i,0\rangle\}$, or any experimentally realizable subspace thereof, by varying indices (k,l).

This method is scalable to multi-photon quantum states. Figure 89(b) shows a mode of operation for two-photon TM state tomography. A general two-photon state (with photon labels A and B) may be expressed in the same TM basis as

$$\hat{\rho}_{IN} = \sum_{j,k,l,m} C_{j,k,l,m}|g_j,0\rangle_A|g_k,0\rangle_B\langle g_l,0|_A\langle g_m,0|. \tag{6.33}$$

The two photons are measured in separate QPG devices with two different pairs of single-photon detectors at their outputs (labelled b_A, g_A, b_B, and g_B), as shown. The pump shapes in the two devices will also need to be independently tunable. I denote the pump shapes at device A and device B as $[\alpha_A]g_m(t)+[e^{i\theta_A}\sqrt{1-\alpha_A}]g_n(t)$ and $[\alpha_B]g_o(t)+[e^{i\theta_B}\sqrt{1-\alpha_B}]g_p(t)$. Then, if we denote the average number of coincidence clicks between detectors g_A and b_B by $N_{gA,bB}$, then the measurable quantity

$$\frac{N_{bA,bB}}{N_{bA,bB}+N_{bA,gB}+N_{gA,bB}+N_{gA,gB}} \tag{6.34}$$

can be expressed in terms of the shape parameters as

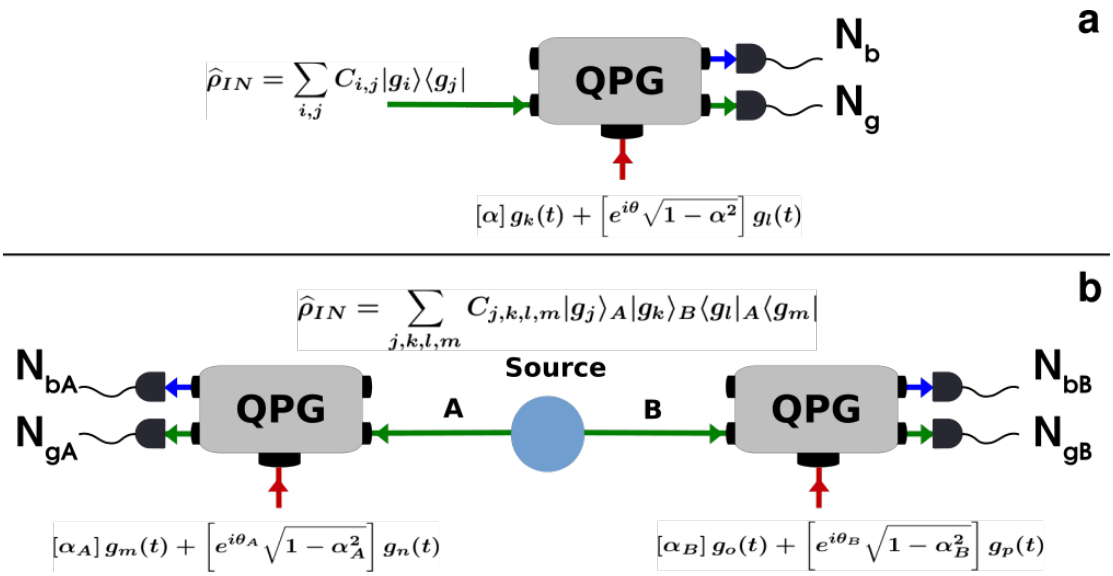

FIGURE 89. Single-photon (a) and two-photon (b) temporal-mode state tomography performed using QPG devices as projective measurements. Any subset of the density matrix can be estimated by shaping the pump pulses appropriately.

$$\begin{aligned}
&\alpha_A^2\alpha_B^2 C_{o,q,q,o} + (1-\alpha_A^2)(1-\alpha_B^2) C_{p,r,r,p} + \alpha_A^2(1-\alpha_B^2) C_{o,r,r,o} + (1-\alpha_A^2)\alpha_B^2 C_{p,q,q,p} \\
&+ 2\mathfrak{Re}\Big[e^{i\theta_A}\alpha_A\sqrt{1-\alpha_A^2}\left\{\alpha_B^2 C_{o,q,q,p} + (1-\alpha_B^2) C_{o,r,r,p}\right\} \\
&+ e^{i\theta_B}\alpha_B\sqrt{1-\alpha_B^2}\left\{\alpha_A^2 C_{o,q,r,o} + (1-\alpha_A^2) C_{p,q,r,p}\right\} \\
&+ \alpha_A\alpha_B\sqrt{1-\alpha_A^2}\sqrt{1-\alpha_B^2}\left\{e^{i(\theta_A+\theta_B)} C_{o,q,r,p} + e^{i(\theta_A-\theta_B)} C_{o,r,q,p}\right\}\Big]. \qquad (6.35)
\end{aligned}$$

Cycling through the shape parameters:

$(\alpha_{A/B}, \theta_{A/B}) \in \{(1,-),(0,-),(1/\sqrt{2},0),(1/\sqrt{2},\pi/2)\}$ as well as varying the indices (m,n,o,p) will reveal any desired set of coefficients from the two-photon density matrix.

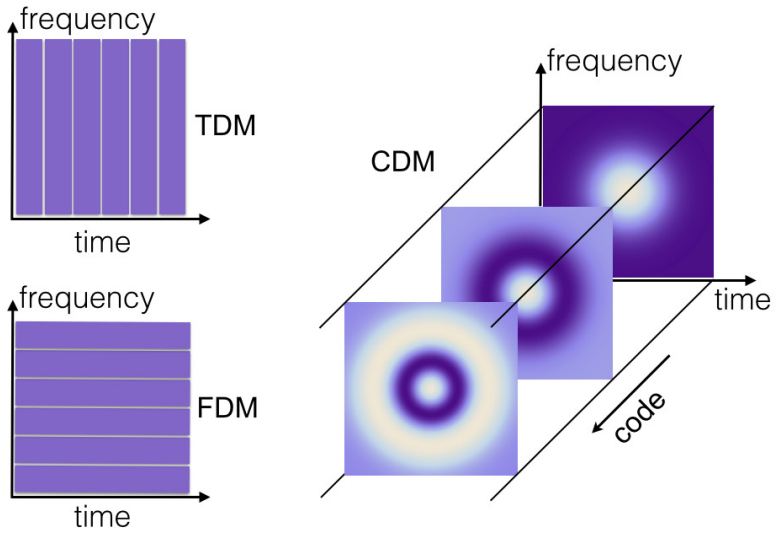

FIGURE 90. Time- and frequency-division multiplexing being contrasted with code-division multiplexing (CDM), with different codes represented by time-frequency Wigner functions for orthogonal temporal modes. The choice of the temporal-mode set is not unique. Image by Prof. M. G. Raymer.

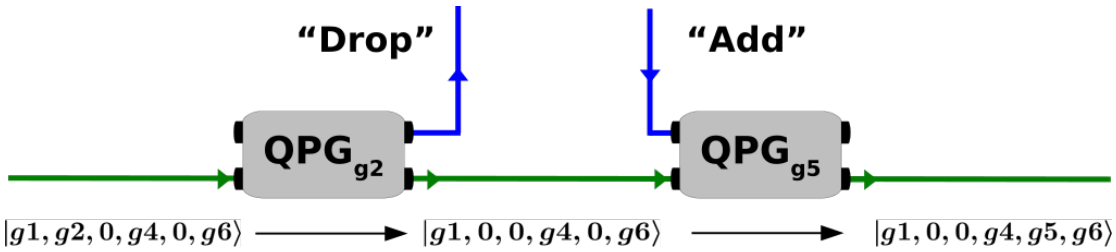

FIGURE 91. All-optical routing and the utilization of different temporal modes as different communication bands in a single guided line in an optical network using QPG devices.

All-optical multiplexing

QPG allows for the realization of true field-orthogonal optical-code-division-multiplexing in guided media even at the single-photon level (Fig. 90). Different temporal modes may be used as different classical/quantum bands for communication in an all-optical routable network, where QPG devices can selectively "add" and "drop" photons or photon components into/from specific bands, as shown in Fig. 91. Although QPG does not offer any improvements

on bounds in band capacity, it allows for more efficient use of a specific optical spectral band spanned by an arbitrary number of temporal mode functions. When extended to FWM-QPG, one can access multiple temporal modes in the b-band as well, and can thus operate two distinct networks at different frequency bands and fully cross-link them with arbitrary inter-band mappings, enabling unitary photon reshaping and interfacing hybrid quantum systems.

The Takeaway

The problem of the sorting of photons with differing shapes was introduced to this author by his advisor on the very first day he joined the group. It was at the time, a theory project meant to supplement the author's experience in helping with the experiments at the lab. The major milestones have been the brick wall at the end of the full analysis of single-stage schemes, the elation of having cracked the problem by use of multiple stages, and the satisfaction of experimentally having verified the prediction. The main philosophical lessons learnt have been to look for solutions to advanced problems (QPG) in the earlier chapters (Mach-Zehnder interferometers), and to look for asymptotic solutions when exact ones prove elusive.

REFERENCES CITED

[1] Newton, I. (1704). *Opticks: or, A Tristies of the Reflections, Refractions, Inflections and Colours of Light* (fourth ed.).

[2] Hooke, R. (1665). *Micrographia, or Some Physiological Descriptions of Minute Bodies* (first ed.). Royal Society.

[3] Huygens, C. (1690). *Traité de la Lumière*. Chez Pierre vander Aa.

[4] Euler, L. (1746). Nova theoria lucis et colorum. *Opuscula varii argumenti 1*, 169–244.

[5] Young, T. (1801). The Bakerian lecture: On the theory of light and colours. *Philosophical Transactions of the Royal Society of London 92*, 12–48.

[6] Michelson, A. A. and E. W. Morley (1887). On the relative motion of the earth and the luminiferous ether. *American Journal of Science 34*, 333–345.

[7] Faraday, M. (1933). *For this discovery see #7504, 13 Sept. 1845 to #7718, 30 Sept. 1845 of Faraday's Dairy. Volume IV, Nov. 12 1839 - June 26, 1847*. George Bell and Sons, Ltd.

[8] Maxwell, J. C. (1873). *A Treatise on Electricity and Magnetism* (first ed.). Oxford: The Clarendon Press.

[9] Hertz, H. R. (1887). On electromagnetic effects produced by electrical disturbances in insulators. *Sitzungsber. d. Berl. Akadem., Wiedmann's Ann. 34*, 273.

[10] Planck, M. (1901). Über das gesetz der energieverteilung im normalspektrum. *Ann. Phys. 4*, 553.

[11] Einstein, A. (1905). Über einen die erzeugung und verwandlung des lichtes betreffenden heuristischen gesichtspunkt. *Ann. Phys. 17*, 132.

[12] Compton, A. H. (1923, May). A quantum theory of the scattering of x-rays by light elements. *Phys. Rev. 21*, 483–502.

[13] Dirac, P. A. M. (1928). The quantum theory of the electron. *Proc. Royal Soc. A 117*, 610.

[14] Tomonaga, S. (1946). On a relativistically invariant formulation of the quantum theory of wave fields. *Progress of Theoretical Physics 1*(2), 27.

[15] Schwinger, J. (1948, Nov). Quantum electrodynamics. I. A covariant formulation. *Phys. Rev. 74*, 1439–1461.

[16] Feynman, R. P. (1949, Sep). Space-time approach to quantum electrodynamics. *Phys. Rev. 76*, 769–789.

[17] Titulaer, U. M. and R. J. Glauber (1966). Density operators for coherent fields. *Phys. Rev. 145*(4), 1041.

[18] Jagannathan, R., R. Simon, E. C. G. Sudarshan, and N. Mukunda (1989). Quantum theory of magnetic electron lenses based on the dirac equation. *Phys. Lett. A 134*(8), 457–464.

[19] Aspect, A., P. Grangier, and G. Roger (1982, Jul). Experimental realization of Einstein-Podolsky-Rosen-Bohm gedankenexperiment: A new violation of Bell's inequalities. *Phys. Rev. Lett. 49*, 91–94.

[20] Clauser, J. F., M. A. Horne, A. Shimony, and R. A. Holt (1969, Oct). Proposed experiment to test local hidden-variable theories. *Phys. Rev. Lett. 23*, 880–884.

[21] Inc., A. (2008). *FCC Rules and Regulations for the Amateur Radio Service* (third ed.). American Radio Relay League.

[22] Mouly, M. and M.-B. Pautet (1992). *The GSM System for Mobile Communications*. Telecom Publishing.

[23] Gnauck, A. H., P. J. Winzer, S. Chandrasekhar, X. Liu, B. Zhu, and D. W. Peckham (2010). 10 × 224-Gb/s WDM transmission of 28-Gbaud PDM 16-QAM on a 50-GHz grid over 1,200 Km of fiber. In *National Fiber Optic Engineers Conference*, pp. PDPB8. Optical Society of America.

[24] Essiambre, R. J., R. Ryf, N. K. Fontaine, and S. Randel (2013, April). Breakthroughs in photonics 2012: Space-division multiplexing in multimode and multicore fibers for high-capacity optical communication. *IEEE Photonics Journal 5*(2), 0701307–0701307.

[25] Ren, Y., Z. Wang, P. Liao, L. Li, G. Xie, H. Huang, Z. Zhao, Y. Yan, N. Ahmed, A. Willner, M. P. J. Lavery, N. Ashrafi, S. Ashrafi, R. Bock, M. Tur, I. B. Djordjevic, M. A. Neifeld, and A. E. Willner (2016, Feb). Experimental characterization of a 400 Gbit/s orbital angular momentum multiplexed free-space optical link over 120 m. *Opt. Lett. 41*(3), 622–625.

[26] Smith, B. J., B. Killett, M. G. Raymer, I. A. Walmsley, and K. Banaszek (2005, Dec). Measurement of the transverse spatial quantum state of light at the single-photon level. *Opt. Lett. 30*(24), 3365–3367.

[27] Smith, B. J. and M. G. Raymer (2007, November). Photon wave functions, wave-packet quantization of light, and coherence theory. *New J. Phys. 9*(11), 414.

[28] Brecht, B., D. V. Reddy, C. Silberhorn, and M. G. Raymer (2015, Oct). Photon temporal modes: A complete framework for quantum information science. *Phys. Rev. X 5*, 041017.

[29] Eckstein, A., B. Brecht, and C. Silberhorn (2011, July). A quantum pulse gate based on spectrally engineered sum frequency generation. *Opt. Express 19*(15), 13770–13778.

[30] Brecht, B., A. Eckstein, A. Christ, H. Suche, and C. Silberhorn (2011, June). From quantum pulse gate to quantum pulse shaper - Engineered frequency conversion in nonlinear optical waveguides. *New J. Phys. 13*(6), 065029.

[31] Cirac, J. I., L. M. Duan, and P. Zöller (2004). Quantum optical implementation of quantum information processing. *arXiv:quant-ph/0405030*.

[32] Lvovsky, A. I., B. C. Sanders, and W. Tittel (2009). Optical quantum memory. *Nat. Photonics 3*, 706–714.

[33] U'Ren, A. B., C. Silberhorn, K. Banaszek, I. A. Walmsley, R. Erdmann, W. P. Grice, and M. G. Raymer (2005). Generation of pure-state single-photon wavepackets by conditional preparation based on spontaneous parametric downconversion. *Laser Phys. 15*, 146–161.

[34] Kuzucu, O., M. Fiorentino, M. A. Albota, F. N. C. Wong, and F. X. Kärtner (2005, Mar). Two-photon coincident-frequency entanglement via extended phase matching. *Phys. Rev. Lett. 94*, 083601.

[35] Nunn, J., L. J. Wright, C. Söller, L. Zhang, I. A. Walmsley, and B. J. Smith (2013, Jul). Large-alphabet time-frequency entangled quantum key distribution by means of time-to-frequency conversion. *Opt. Express 21*(13), 15959–15973.

[36] Shannon, C. E. (2001, January). A mathematical theory of communication. *SIGMOBILE Mob. Comput. Commun. Rev. 5*(1), 3–55.

[37] Leverrier, A., R. Alléaume, J. Boutros, G. Zémor, and P. Grangier (2008, Apr). Multidimensional reconciliation for a continuous-variable quantum key distribution. *Phys. Rev. A 77*, 042325.

[38] Nunn, J. (2008). *Quantum Memory in Atomic Ensembles*. Ph. D. thesis, University of Oxford.

[39] Kumar, P. (1990, Dec). Quantum frequency conversion. *Opt. Lett. 15*(24), 1476–1478.

[40] Reddy, D. V., M. G. Raymer, C. J. McKinstrie, L. Mejling, and K. Rottwitt (2013, June). Temporal mode selectivity by frequency conversion in second-order nonlinear optical waveguides. *Opt. Express 21*(11), 13840–13863.

[41] Reddy, D. V., M. G. Raymer, and C. J. McKinstrie (2014, May). Efficient sorting of quantum-optical wave packets by temporal-mode interferometry. *Optics Letters 39*(10), 2924–2927.

[42] Reddy, D. V., M. G. Raymer, and C. J. McKinstrie (2015, Jan). Sorting photon wave packets using temporal-mode interferometry based on multiple-stage quantum frequency conversion. *Phys. Rev. A 91*, 012323.

[43] Christensen, J. B., D. V. Reddy, C. J. McKinstrie, K. Rottwitt, and M. G. Raymer (2015, Sep). Temporal mode sorting using dual-stage quantum frequency conversion by asymmetric Bragg scattering. *Opt. Express 23*(18), 23287–23301.

[44] Reddy, D. V. and M. G. Raymer (2017a, May). Engineering temporal-mode-selective frequency conversion in nonlinear optical waveguides: from theory to experiment. *Opt. Express 25*(11), 12952–12966.

[45] Reddy, D. V. and M. G. Raymer (2017b). Photonic temporal-mode multiplexing by quantum frequency conversion in a dichroic-finesse cavity. *arXiv:1708.01705*.

[46] Jackson, J. D. (1998). *Classical Electrodynamics* (third ed.). Wiley.

[47] Dirac, P. A. M. (1927). The quantum theory of the emission and absorption of radiation. *Proceedings of the Royal Society of London A: Mathematical, Physical and Engineering Sciences 114*(767), 243–265.

[48] Steck, D. (2007). *Quantum and Atom Optics*.

[49] Hillery, M. and L. D. Mlodinow (1984, Oct). Quantization of electrodynamics in nonlinear dielectric media. *Phys. Rev. A 30*, 1860.

[50] Quesada, N. and J. E. Sipe (2017). Why you should not use the electric field to quantize in nonlinear optics. *arXiv:1707.01686*.

[51] Caves, C. M. (1981, Apr). Quantum-mechanical noise in an interferometer. *Phys. Rev. D 23*, 1693.

[52] Paul, H. (1982, Oct). Photon antibunching. *Rev. Mod. Phys. 54*, 1061.

[53] Leonhardt, U. (1993, Oct). Quantum statistics of a lossless beam splitter: SU(2) symmetry in phase space. *Phys. Rev. A 48*, 3265.

[54] Elitzur, A. C. and L. Vaidman (1993, Jul). Quantum mechanical interaction-free measurements. *Found. Phys. 23*(7), 987–997.

[55] Humphreys, P. C., W. S. Kolthammer, J. Nunn, M. Barbieri, A. Datta, and I. A. Walmsley (2014, Sep). Continuous-variable quantum computing in optical time-frequency modes using quantum memories. *Phys. Rev. Lett. 113*, 130502.

[56] Gröblacher, S., T. Jennewein, A. Vaziri, G. Weihs, and A. Zeilinger (2006). Experimental quantum cryptography with qutrits. *New J. Phys. 8*(5), 75.

[57] Barreiro, J. T., T.-C. Wei, and P. G. Kwiat (2008). Beating the channel capacity limit for linear photonic superdense coding. *Nat. Phys. 4*(4), 282–286.

[58] Leach, J., E. Bolduc, D. J. Gauthier, and R. W. Boyd (2012, Jun). Secure information capacity of photons entangled in many dimensions. *Phys. Rev. A 85*, 060304.

[59] Loudon, R. (2000). *The Quantum Theory of Light* (third ed.). Oxford: Oxford University Press.

[60] Raymer, M. G., J. Noh, K. Banaszek, and I. A. Walmsley (2005, Aug). Pure-state single-photon wave-packet generation by parametric down-conversion in a distributed microcavity. *Phys. Rev. A 72*, 023825.

[61] Zernike, F. and J. E. Midwinter (1973). *Applied Nonlinear Optics* (first ed.). Wiley-Interscience.

[62] Huang, J. and P. Kumar (1992, Apr). Observation of quantum frequency conversion. *Phys. Rev. Lett. 68*, 2153.

[63] Vandevender, A. P. and P. G. Kwiat (2004, January). High efficiency single photon detection via frequency up-conversion. *J. Mod. Opt. 51*(9-10), 1433–1445.

[64] Albota, M. A. and F. N. C. Wong (2004, July). Efficient single-photon counting at 1.55 μm by means of frequency upconversion. *Optics Letters 29*(13), 1449–1451.

[65] Roussev, R. V., C. Langrock, J. R. Kurz, and M. M. Fejer (2004, July). Periodically poled lithium niobate waveguide sum-frequency generator for efficient single-photon detection at communication wavelengths. *Optics Letters 29*(13), 1518–1520.

[66] Ding, Y. and Z. Y. Ou (2010, August). Frequency downconversion for a quantum network. *Optics Letters 35*(15), 2591–2593.

[67] Raymer, M. G., S. J. van Enk, C. J. McKinstrie, and H. J. McGuinness (2010, March). Interference of two photons of different color. *Opt. Commun. 283*(5), 747–752.

[68] McGuinness, H. J., M. G. Raymer, C. J. McKinstrie, and S. Radic (2010, August). Quantum Frequency Translation of Single-Photon States in a Photonic Crystal Fiber. *Phys. Rev. Lett. 105*(9), 093604.

[69] Strang, G. (1998). *Introduction to Linear Algebra* (third ed.). Wellesley-Cambridge Press.

[70] Gbur, G. J. (2011). *Mathematical Methods for Optical Physics and Engineering*. Cambridge Press.

[71] Brecht, B., A. Eckstein, R. Ricken, V. Quiring, H. Suche, L. Sansoni, and C. Silberhorn (2014, Sep). Demonstration of coherent time-frequency schmidt mode selection using dispersion-engineered frequency conversion. *Phys. Rev. A 90*, 030302.

[72] Ansari, V., M. Allgaier, L. Sasoni, B. Brecht, J. Roslund, N. Treps, G. Harder, and C. Silberhorn (2016). Temporal-mode tomography of single photons. *arXiv:1607.03001v1*.

[73] Braunstein, S. (2005, May). Squeezing as an irreducible resource. *Phys. Rev. A 71*(5), 055801.

[74] Raymer, M. G. and K. Srinivasan (2012). Manipulating the color and shape of single photons. *Physics Today 65*(11), 32.

[75] Rakher, M., L. Ma, O. Slattery, X. Tang, and K. Srinivasan (2010). Quantum transduction of telecommunications-band single photons from a quantum dot by frequency upconversion. *Nat. Photon. 4*(October).

[76] Ikuta, R., Y. Kusaka, T. Kitano, H. Kato, T. Yamamoto, M. Koashi, and N. Imoto (2011, January). Wide-band quantum interface for visible-to-telecommunication wavelength conversion. *Nat. Commun. 2*, 1544.

[77] Mejling, L., C. J. McKinstrie, M. G. Raymer, and K. Rottwitt (2012). Quantum frequency translation by four-wave mixing in a fiber: low-conversion regime. *Opt. Express 20*(8), 695–697.

[78] Brańczyk, A. M., A. Fedrizzi, T. M. Stace, T. C. Ralph, and A. G. White (2011, January). Engineered optical nonlinearity for quantum light sources. *Opt. Express 19*(1), 55–65.

[79] McGuinness, H. J. (2011). *The creation and frequency translation of single-photon states of light in optical fiber*. Ph. D. thesis, University of Oregon.

[80] Manurkar, P., N. Jain, M. Silver, Y.-P. Huang, C. Langrock, M. M. Fejer, P. Kumar, and G. S. Kanter (2016, Dec). Multidimensional mode-separable frequency conversion for high-speed quantum communication. *Optica 3*(12), 1300–1307.

[81] Clemmen, S., A. Farsi, S. Ramelow, and A. L. Gaeta (2016, Nov). Ramsey interference with single photons. *Phys. Rev. Lett. 117*, 223601.

[82] Kobayashi, T., D. Yamazaki, K. Matsuki, R. Ikuta, S. Miki, T. Yamashita, H. Terai, T. Yamamoto, M. Kaoshi, and N. Imoto (2017). Mach-Zehnder interferometer using frequency-domain beamsplitter. *arXiv:1703.08114*.

[83] McKinstrie, C. J., L. Mejling, M. G. Raymer, and K. Rottwitt (2012, May). Quantum-state-preserving optical frequency conversion and pulse reshaping by four-wave mixing. *Phys. Rev. A 85*(5), 053829.

[84] Raymer, M. G. and J. Mostowski (1981). Stimulated Raman scattering: Unified treatment of spontaneous initiation and spatial propagation. *Phys. Rev. A 24*(4), 1980.

[85] Giacone, R. E., C. J. McKinstrie, and R. Betti (1995). Angular dependence of stimulated Brillouin scattering in homogeneous plasma. *Physics of Plasmas 2*(12), 4596.

[86] Churchill, R. V. (1971). *Operational Mathematics* (third ed.). McGraw-Hill.

[87] Raymer, M. G. (2004). Quantum state entanglement and readout of collective atomic-ensemble modes and optical wave packets by stimulated Raman scattering. *J. Mod. Opt. 51*(12), 1739–1759.

[88] Burnham, D. and R. Chiao (1969, December). Coherent resonance fluorescence excited by short light pulses. *Phys. Rev. 188*(2), 667–675.

[89] Pfister, O., S. Feng, G. Jennings, R. Pooser, and D. Xie (2004, Aug). Multipartite continuous-variable entanglement from concurrent nonlinearities. *Phys. Rev. A 70*, 020302.

[90] McKinstrie, C. J., S. J. van Enk, M. G. Raymer, and S. Radic (2008, Feb). Multicolor multipartite entanglement produced by vector four-wave mixingin a fiber. *Opt. Express 16*(4), 2720–2739.

[91] Clemmen, S., A. Farsi, S. Ramelow, and A. L. Gaeta (2014). Ramsey interferometry with photons. In *CLEO: 2014 Postdeadline Paper Digest, paper: FTh5A.2*. Optical Society of America.

[92] Raymer, M. G., S. J. van Enk, C. J. McKinstrie, and H. J. McGuinness (2010, March). Interference of two photons of different color. *Opt. Commun. 283*(5), 747–752.

[93] Quesada, N. and J. E. Sipe (2016, Jan). High efficiency in mode-selective frequency conversion. *Opt. Lett. 41*(2), 364–367.

[94] Mejling, L., D. S. Cargill, C. J. McKinstrie, K. Rottwitt, and R. O. Moore (2012, Nov). Effects of nonlinear phase modulation on Bragg scattering in the low-conversion regime. *Opt. Express 20*(24), 27454–27475.

[95] Mejling, L., S. M. M. Friis, D. V. Reddy, K. Rottwitt, M. G. Raymer, and C. J. McKinstrie (2014). Asymmetrically pumped bragg scattering with the effects of nonlinear phase modulation. In *Advanced Photonics, paper: JTu3A.36*. Optical Society of America.

[96] Ansari, V., G. Herder, M. Allgaier, B. Brecht, and C. Silberhorn (2017). Temporal-mode detector tomography of a quantum pulse gate. *arXiv:1702.03336v1*.

[97] Zheng, Z. and A. Weiner (2001). Coherent control of second harmonic generation using spectrally phase coded femtosecond waveforms. *Chemical Physics 267*(1), 161 – 171.

[98] Zheng, Z., A. M. Weiner, K. R. Parameswaran, M.-H. Chou, and M. M. Fejer (2002, Apr). Femtosecond second-harmonic generation in periodically poled lithium niobate waveguides with simultaneous strong pump depletion and group-velocity walk-off. *J. Opt. Soc. Am. B 19*(4), 839–848.

[99] Laiho, K., K. N. Cassemiro, and C. Silberhorn (2009, Dec). Producing high fidelity single photons with optimal brightness via waveguided parametric down-conversion. *Opt. Express 17*(25), 22823–22837.

[100] Weiner, A. M. (2000). Femtosecond pulse shaping using spatial light modulators. *Review of Scientific Instruments 71*(5), 1929–1960.

[101] Frumker, E. and Y. Silberberg (2007, Dec). Phase and amplitude pulse shaping with two-dimensional phase-only spatial light modulators. *J. Opt. Soc. Am. B 24*(12), 2940–2947.

[102] Christ, A., B. Brecht, W. Mauerer, and C. Silberhorn (2013, May). Theory of quantum frequency conversion and type-II parametric down-conversion in the high-gain regime. *New J. Phys. 15*(5), 053038.

[103] Bao, X.-H., A. Reingruber, P. Dietrich, J. Rui, A. Duck, T. Strassel, L. Li, N.-L. Liu, B. Zhao, and J.-W. Pan (2012). Efficient and long-lived quantum memory with cold atoms inside a ring cavity. *Nat. Phys. 8*, 517–521.

[104] Nunn, J., J. H. D. Munns, S. Thomas, K. T. Kaczmarek, C. Qiu, A. Feizpour, E. Poem, B. Brecht, D. J. Saunders, P. M. Ledingham, D. V. Reddy, M. G. Raymer, and I. A. Walmsley (2017, Jul). Theory of noise suppression in Λ-type quantum memories by means of a cavity. *Phys. Rev. A 96*, 012338.

[105] Raymer, M. G. and C. J. McKinstrie (2013, Oct). Quantum input-output theory for optical cavities with arbitrary coupling strength: Application to two-photon wave-packet shaping. *Phys. Rev. A 88*, 043819.

[106] Ramelow, S., A. Farsi, S. Clemmen, D. Orquiza, K. Luke, M. Lipson, and A. L. Gaeta (2015). Silicon-nitride platform for narrowband entangled photon generation. *arXiv:1508.04358*.

[107] Menicucci, N. C., S. T. Flammia, and O. Pfister (2008, Sep). One-way quantum computing in the optical frequency comb. *Phys. Rev. Lett. 101*, 130501.

[108] Rieländer, D., A. Lenhard, O. Jimenez, A. Máttar, D. Cavalcanti, M. Mazzera, A. Acín, and H. de Reidmatten (2017). Frequency-bin entanglement of ultra-narrow band non-degenerate photon pairs. *arXiv:1707.02837*.

[109] Kuo, P. S. and G. S. Solomon (2011, Aug). On- and off-resonance second-harmonic generation in gaas microdisks. *Opt. Express 19*(18), 16898–16918.

[110] Bi, Z.-F., A. W. Rodriguez, H. Hashemi, D. Duchesne, M. Loncar, K.-M. Wang, and S. G. Johnson (2012, Mar). High-efficiency second-harmonic generation in doubly-resonant $\chi(2)$ microring resonators. *Opt. Express 20*(7), 7526–7543.